



Polymerization-induced microphase separation of a polymerization mixture into nanostructured block polymer materials[☆]



Taeseok Oh^a, Suchan Cho^a, Changsu Yoo^a, Wonjune Yeo^a, Jinyeong Oh^a, Myungeun Seo^{a,b,*}

^a Department of Chemistry, Korea Advanced Institute of Science and Technology (KAIST), Daejeon 34141, Korea

^b KAIST Institute for Nanocentury, KAIST, Daejeon 34141, Korea

ARTICLE INFO

Article history:

Received 21 March 2023

Revised 14 July 2023

Accepted 13 August 2023

Available online 16 August 2023

Keywords:

Polymerization-induced microphase separation

Block polymer

RAFT polymerization

Bicontinuous morphology

Porous polymer

Polymer electrolyte

ABSTRACT

Block polymers comprising covalently joined polymeric segments represent a class of nanostructured, multicomponent polymeric materials. Polymerization-induced microphase separation (PIMS) is an intriguing subset that allows for simultaneous nanostructuring during block polymer synthesis. In contrast to polymerization-induced self-assembly (PISA), useful for the spontaneous formation of block polymer micelles, PIMS is well suited to fabricating monolithic block polymer materials by turning a whole polymerization mixture into a nanostructured solid. With the *in situ* cross-linking feature, PIMS offers a facile route to nanostructured block polymer thermosets in combination with various polymerization techniques, from emulsion polymerization to 3D printing. This review aims to provide a comprehensive overview and practical guide on PIMS by covering its historical background and mechanistic aspects and also highlighting representative material classes and applicable polymerization techniques.

© 2023 Elsevier B.V. All rights reserved.

1. Introduction

1.1. Polymerization-induced structuring

Block polymers are hybrid macromolecules consisting of chemically distinct polymer segments joined by covalent bonds. The covalent junction prevents the constituting blocks from separating apart even under immiscible conditions [1]. For example, A-*b*-B diblock polymers prefer to populate at the interface of A- and B-selective media and behave as interfacial stabilizers by reducing interfacial tension [2,3]. In an A-selective solvent, the diblock copolymers self-assemble into micelles by segregation of the B block [4]. When the constituting blocks are immiscible in neat, they undergo microphase separation to form periodic nanostructures composed of discrete A and B microdomains. Their morphologies and length scales depend on the molar mass and the composition of block polymers, which can be adjusted in the synthesis step by employing controlled polymerization techniques [5–9]. The size of most block polymer-based structures falls into the range of 1 – 1000 nm.

With synthetic freedom of block combination, block polymers offer a unique, versatile, and controlled route to polymeric nanomaterials and find a wide range of applications, including thermoplastic elastomers [10], drug delivery vehicles [11], lithographic templates [12], and membranes [13,14].

Over the past decade, interest in block polymers has focused on polymerization-induced structuring strategies that dynamically couple the synthesis and nanostructuring steps. Traditionally, block polymers have been synthesized by consecutive controlled polymerizations, purified, and then processed into the desired macroscopic shape accompanying nanostructuring, often including additional steps such as annealing [15]. *In situ* nanostructuring during the block polymer formation can reduce the number of steps to the final materials. More importantly, new exciting features, such as access to new self-assembling phases, can emerge in the process of turning a homogeneous polymerization mixture into nanostructured materials by polymerization as the nanostructure evolution follows a complex pathway in the competition between polymerization and ordering kinetics.

There have been many excellent reviews on polymerization-induced self-assembly (PISA) utilizing the spontaneous formation of block polymer micelles during chain extension in a selective solvent (see [16–21] for representative examples). However, no comprehensive review exists on polymerization-induced microphase separation (PIMS) since its first report in 2012 [22], where neat

[☆] This MS is for October 2023, Volume 145 – Rising Stars. Please include the special logo on the first page of this review article to indicate that this paper is part of the special Issue 'Rising Stars 2023'.

* Corresponding author.

E-mail address: seomyungeun@kaist.ac.kr (M. Seo).

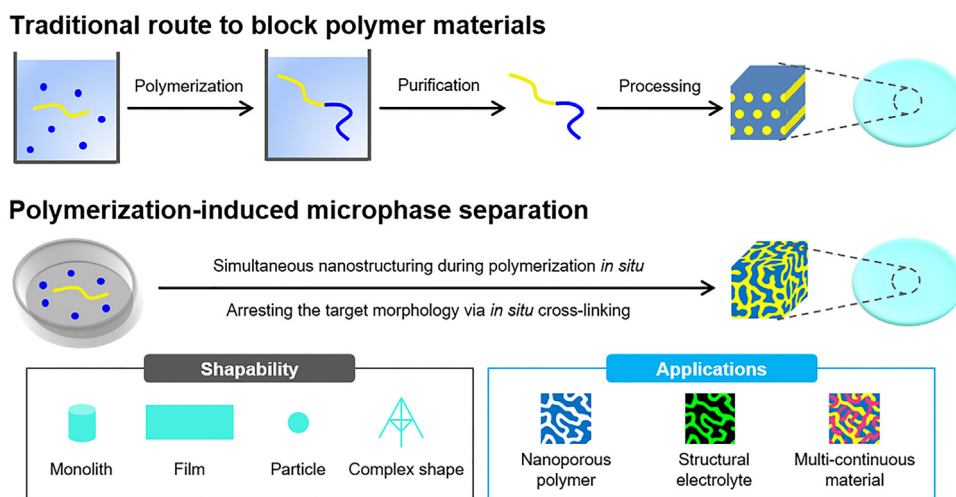


Fig. 1. Concept of PIMS. Compared to traditional block polymer systems where the synthesis and processing steps are decoupled, block polymer formation in the neat polymerization mixture produces nanostructured materials in one step via the PIMS mechanism. Some accessible product shapes and representative applications are given as examples.

polymerization in the absence of a solvent (or with a minimal amount of a solvent required to ensure the homogeneity of the mixture) converts the whole polymerization mixture into a solid monolith. With the *in situ* cross-linking feature, PIMS offers a facile route to nanostructured block polymer thermosets and has found numerous applications, from structural polymer electrolytes to robust nanoporous polymers as outlined in Fig. 1. Recent progress exploits the compatibility of the PIMS process with various polymerization and processing techniques, such as emulsion polymerization and 3D printing, showcasing the synthesis of more complex and hierarchically structured materials across several length scales.

In this contribution, we aim to provide a comprehensive overview and also a practical guide on the PIMS process to facilitate its use by the wider polymer community. The Review is organized as follows. In the first section, we present a historical account of PIMS to portray how polymerization-induced structuring strategies have evolved by adopting block polymers. Then we discuss the mechanistic aspects of the PIMS process compared to the temperature-driven microphase separation behavior of presynthesized block polymers and identify factors influencing the nanostructure evolution. The following sections will cover representative material classes based on the PIMS process and applicable polymerization techniques with a thorough literature survey. We summarize the key features of PIMS and propose future challenges in the final section.

1.2. Historical background

Blending immiscible polymers has been widely investigated to produce composite materials with enhanced properties [23]. For example, dispersing rubbery polymer domains in the glassy polymer matrix can enhance toughness and impact resistance [24]. However, controlling the phase separation dynamics to optimize the morphology with restraining domain size is often challenging, especially when the polymer pair is strongly incompatible.

Polymerization-induced phase separation (PIPS) circumvents the polymer miscibility issue by starting with a mixture of a polymer (“modifier” or “diluent”) with monomers [17]. A homogeneous solution can be obtained relatively readily as the degree of polymerization N in the monomer state equals 1. Phase separation occurs during polymerization mainly because increasing N reduces the entropic contribution to the free energy of mixing. Vitrifica-

tion or *in situ* cross-linking by including a cross-linking agent in the solution can prevent coarsening of the domains and arrest the emerging morphology [25]. Toughened epoxy and polyurethane resins and polymer-dispersed liquid crystals are well-known examples produced by PIPS [26–32]. Low molar mass compounds have also been used as the porogenic diluent to induce phase separation with the growing polymer network and create macroporous void upon removal [33–43].

Block copolymers containing the growing polymer-compatible and incompatible blocks have been developed as modifiers to produce microphase-separated morphologies in the resulting materials. For example, Hillmyer et al. utilized poly(ethylene oxide)-*b*-poly(ethyl ethylene) (PEO-*b*-PEE) for the synthesis of modified epoxy resins [44,45]. As the epoxy-miscible PEO chains surrounded the epoxy-incompatible PEE domain and stabilized it against coarsening, ordered arrays of the PEE core embedded in the epoxy matrix could be obtained. Meng et al. showed a microphase separated morphology could emerge from a disordered mixture of poly(ϵ -caprolactone)-*b*-polybutadiene-*b*-poly(ϵ -caprolactone) with epoxy monomers upon curing [46].

The absence of covalent bonds between the presynthesized polymer and the growing polymer characterizes the PIPS examples described above. High-impact polystyrene (HIPS) represents an intriguing example of creating covalent connections between the preexisting and growing polymer blocks. Radical polymerization of styrene in the presence of polybutadiene (PB) dissolved in styrene grafts PS chains on PB *in situ* by consuming its double bonds. Despite not falling into the category of block polymers, the resulting nonlinear macromolecules effectively stabilize the PS/PB interface and produce the well-known “salami” morphology of PB domains dispersed in the continuous PS phase [47].

In 1995, Ryan et al. investigated how nanostructures evolve when covalent junctions form between polymer segments during polyurethane synthesis [48,49]. *In situ* small-angle X-ray scattering (SAXS) measurements showed that a scattering peak corresponding to the periodicity in the nanometer length scale appeared above a critical conversion, signaling the onset of microphase separation. The peak intensity grew and saturated over time, indicating the resulting multiblock copolymer composed of alternatingly arranged hard and soft segments induced microphase separation during the step-growth polymerization. Vitrification of the hard domain froze the disordered interconnected morphology in the polyurethane.

Structure evolution during the block polymer formation via living and controlled polymerizations based on the chain growth mechanism has also been studied [50–55]. In 2006, Hashimoto et al. used time-resolved small-angle neutron scattering (SANS) to monitor the anionic polymerization of styrene and isoprene in a concentrated benzene solution. Rapid consumption of isoprene produced clusters of mostly polyisoprene (PI) anions [56]. Continuous polymerization produced (tapered) PI-*b*-PS block copolymers, which induced a transition into the ordered phase through concentration fluctuation and finally adopted a hexagonally packed cylindrical morphology in solution. They coined the term “polymerization-induced microphase transition” to indicate that the increasing N drives the system to order, not changes in temperature or pressure, as in the presynthesized block polymers. They further investigated a neat polymerization system by utilizing reversible addition-fragmentation chain transfer (RAFT) polymerization. PMMA-macro chain transfer agent (PMMA-CTA) was dissolved in styrene to make a homogeneous mixture, and styrene polymerization was again followed by SANS [57]. An order-disorder transition and more order-order transitions were detected with the increasing conversion, along with macrophase separation, probably because of PS homopolymer formation. They also theoretically predicted that complex non-equilibrium morphologies could emerge when the polymerization proceeds faster than ordering kinetics [58].

Around the same time, several groups pursued chain extension in a selective solvent as modified versions of dispersion and emulsion polymerizations to synthesize uniform block polymer micelles and latex particles [59–65]. The key feature was to utilize a solvophilic polymer as the first block and extend the chain with a solvophobic block. In the case of dispersion polymerization, the solvophobic block was chosen to be miscible in the monomer state but to segregate over a critical molar mass. Spontaneous aggregation resulted in the formation of block polymer micelles. The term “polymerization-induced self-assembly” seems to be first used around 2012 to describe the process [66]. Depending on the factors such as the chain mobility of the micellar core, the micelle could undergo morphological transitions as the polymerization proceeded with the increasing fraction of the solvophobic block. Some works included a cross-linker such as divinylbenzene (DVB) as a co-monomer to synthesize core cross-linked and microgel star polymers [67–70], which also trapped the emergent morphology by *in situ* cross-linking.

In 2012, Seo and Hillmyer reported neat RAFT copolymerization of styrene and DVB in the presence of polylactide (PLA)-CTA and used the term “PIMS” for the process [22]. Fig. 2 schematically illustrates the PIMS process compared to PIPS and PISA. A trithiocarbonate group was installed at the PLA chain end as the CTA motif and successfully mediated the radical copolymerization. The P(S-*co*-DVB) block adopting the branched network topology grew from the PLA chain end to produce PLA-*b*-P(S-*co*-DVB). The increasing N and the block polymer concentration at the cost of the monomer consumption by polymerization induced microphase separation. While the transient disordered bicontinuous morphology was arrested at the onset of gelation, the polymerization proceeded further to nearly complete conversion and resulted in a solid transparent monolith. A robust nanoporous polymer with percolating pores supported by the densely cross-linked P(S-*co*-DVB) framework could be obtained by PLA etching. Since then, several groups have exploited the potential of the PIMS process, particularly focusing on feasible access to the bicontinuous nanostructure. Table 1 summarizes polymer combinations for PIMS available in the literature, along with polymerization methods and applications.

PISA offers a feasible route to preparing block polymer micelles at high concentrations. Both PIPS and PIMS are suited for

producing neat polymeric materials. Dispersed and cocontinuous morphologies at the micrometer length scale can be readily accessed for immiscible polymer blends via PIPS. PIMS could be more advantageous if nanoscopic morphologies are desired with length scale control.

The boundaries between PIMS, PIPS, and PISA are becoming less clear. For example, adding a homopolymer in the PIMS formulation can induce a transition from PIMS to PIPS with a gradual increase in the domain size [71]. A high-molar mass homopolymer additive can drive PIMS and PIPS simultaneously. Similarly, a small amount of the selective solvent can be added to the PIMS polymerization mixture to swell the domain of the first block while retaining the product's monolithic feature [72]. The polymerization follows the PISA mechanism when the polymer domain cannot accommodate the whole solvent. PISA can exhibit lyotropic phase transitions in the concentrated solution, for example, from closed-packed spherical to hexagonally-packed cylindrical phases [73].

Examples of polymerization-induced phase transitions in microphase-separated media have also been reported by Hickey and co-workers [74–76]. Analogous to HIPS, *in situ* grafting of PS on PS-*b*-PB led to complex phase transitions with increasing styrene conversion. Besides polymerization, postpolymerization modification can induce phase transitions by chemically transforming one block into another and thus tuning the interaction parameter. For example, Magenau and co-workers reported that Pd-catalyzed cross-coupling [77] and thiol-epoxide click reactions [78] can be used to form block polymer micelles *in situ* by modifying the core block. Chen and co-workers reported phase transitions of glycopolymer amphiphiles via deacetylation [79,80] and debenzoylation [81]. These “reaction-induced phase transition” approaches are anticipated to enrich the toolbox of *in situ* nanostructuring further.

Finally, we should note that other polymerization methodologies can also induce microphase separation at the nanometer length scale. For example, free radical copolymerization of *N,N*-dimethylacrylamide (DMA) with acrylate-appended telechelic polydimethylsiloxane (PDMS) formed covalent junctions between PDMS and PDMA *in situ* that led to a cross-linked network consisting of disordered bicontinuous PDMS and PDMA domains [82]. Hayward et al. also developed an approach to creating bicontinuous polymer networks. In this “randomly end-linked copolymer network,” the end groups of two different telechelic polymers are arbitrarily tied to produce disordered bicontinuous morphologies over a wide composition range of the constituent network strands [83–87]. Distinct from PIMS, these approaches offer a route to cocontinuous nanostructures without using controlled polymerization techniques.

2. Fundamental aspects of PIMS

2.1. Driving force to order: temperature vs. polymerization

The phase behavior of neat block polymers is governed by the Flory-Huggins interaction parameter (χ), volume composition (f), and N . Fig. 3a shows a theoretical phase diagram of an A-*b*-B diblock copolymer constructed based on the self-consistent mean-field theory [88]. The composition f is designated the X-axis and determines the interfacial curvature of the microphase-separated morphology. The Y-axis constitutes a product of $\chi_{AB}N$ as the segregation strength. χ_{AB} represents the incompatibility between two blocks and is given in eqn (1).

$$\chi_{AB} = \left(\frac{z}{k_B T} \right) \left[\varepsilon_{AB} - \frac{1}{2}(\varepsilon_{AA} + \varepsilon_{BB}) \right] \quad (1)$$

where z is the number of neighbors of one repeating unit of polymers, k_B is Boltzmann constant, and ε_{AA} , ε_{BB} , and ε_{AB} are interaction energy between A-A, B-B, and A-B per unit molecules, respec-

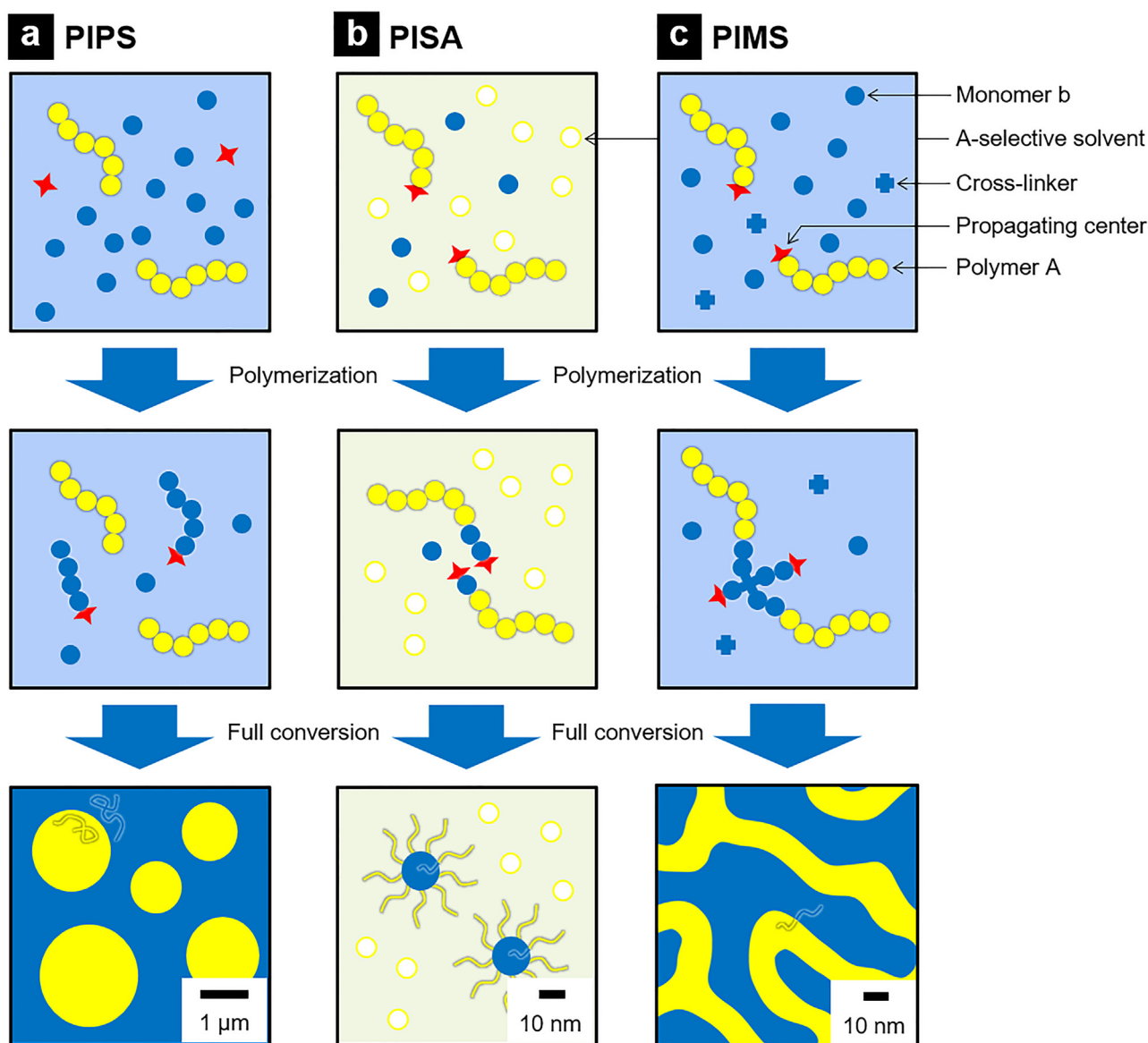


Fig. 2. Schematic illustration of PIPS (a), PISA (b), and PIMS (c) processes. (a) PIPS starts with a homogeneous solution of polymer A dissolved in monomer b. Polymerization converts monomer b into polymer B, resulting in macrophase separation between A and B. A droplet morphology is drawn as an example. (b) In PISA, polymer A carrying a propagating center at the chain end is dissolved in an A-selective solvent with monomer b. Growing the B chain from the A chain end, incompatible with the solvent, spontaneously produces block polymer micelles. A spherical morphology is given as an example. (c) PIMS does not require solvent in contrast to PISA. Polymerization proceeds in a neat polymerization mixture typically containing a cross-linker as a comonomer. The whole mixture is converted into a monolithic solid with a disordered bicontinuous morphology composed of A and B microdomains at the nanometer length scale. The chain conformation in the final materials is sketched as lines.

tively [1]. As χ is inversely proportional to temperature, cooling a disordered block polymer melt below the order-disorder transition temperature (T_{ODT}) can induce microphase separation for block polymers with fixed N .

While temperature is typically kept constant in the PIMS process, polymerization drives the system to order. The initial polymerization mixture can be considered a solution of polymer A in monomer b. Polymerization produces A-*b*-B diblock copolymer by consuming monomer b, which continuously increases N , f_B , and the block polymer concentration (φ) in the solution as a function of conversion. Assuming χ_{AB} , χ_{Ab} , and χ_{Bb} do not vary upon b polymerization, the polymerizing solution can be described by a three-dimensional phase diagram composed of f , N , and φ axes. Such a phase diagram is illustrated in Fig. 3b [89]. Note that the diagram during the polymerization is not symmetric for f because monomer b should be much more selective to its own polymer B

than A (i.e., $\chi_{Ab} > \chi_{Bb}$). Roughly, both increases in N and φ facilitate microphase separation, while changes in f and φ allow the solution to move across various phases during polymerization, as exemplified in Fig. 3c [90].

The polymerizing solution may not reach thermodynamic equilibrium during polymerization. This kinetic feature could be more significant in PIMS than PISA because the much higher viscosity of the neat polymerization mixture could slow down the chain dynamics. Iida et al. investigated the phase transition behavior by calculating the free energy of the system by developing a coarse-grained model based on the Ginzburg-Landau expansion coupled with random phase approximation (Fig. 3d) [58]. While fast polymerization essentially yielded a quenched block polymer melt, the phase transition and the domain growth kinetics could compete with the slower polymerization. Non-equilibrium morphologies such as inverted cylinders were found when the do-

Table 1

PIMS formulations reported in the literature and their applications.

Macro-CTA	Monomer	Cross-linker	Additive	Polymerization technique	Material	Reference
PLA	S	DVB		Bulk	Nanoporous polymer	[22,107]
PLA	S	DVB		Bulk	Nanoporous film	[169]
PLA	S	DVB		Bulk (with impregnated support)	Nanoporous membrane	[170]
PLA	S	DVB		Emulsion	Semipermeable microcapsule	[198]
PLA	S	DVB		Emulsion	Micro-/meso-/macroporous polymer	[207]
PLA	S	DVB	PLA	Bulk	Meso-/macroporous polymer	[71]
PLA	S	DVB	PEO	Bulk	Meso-/macroporous polymer	[115]
PLA	S	DVB	Acetonitrile	Bulk	Nanoporous polymer	[72]
PLA	S	MVCLs		Bulk	Micro-/mesoporous polymer	[138,139]
PLA	4-alkyl styrenes	DVB		Bulk	Micro-/mesoporous polymer	[137]
PLA	VBzCl	DVB		Bulk	Micro-/mesoporous polymer	[143]
PLA	TMSS, VBzCl	DVB		Bulk	Micro-/mesoporous polymer	[109,144]
PLA	IBA	EGDA		Photo	Nanoporous film	[191]
PLA	S	DVB		Bulk (simultaneous block polymerization)	Nanoporous polymer	[116]
PLA, PI	S	DVB		Bulk	Nanoporous polymer	[147]
PEO	S	DVB	BMITFSI, LiTFSI	Bulk	Polymer electrolyte	[158]
PEO	S	DVB	BMITFSI	Bulk	Polymer electrolyte	[111]
PEO	S	DVB	HEImTFSI	Bulk	Polymer electrolyte	[160]
PEO	S	DVB	LiTFSI + SN	Bulk	Polymer electrolyte	[159]
PEO	S	DVB	Acetonitrile + polyoxometalates	Bulk	Polymer electrolyte	[161]
PEO	mVSZ	DVB		Bulk	Mesoporous SiCN	[179]
PEO	IBA	TMPTA	BMITFSI	Photo	3D-printed polymer electrolyte	[217]
POEGMEA	IBA	TMPTA	BMITFSI	Photo	3D-printed polymer electrolyte	[218]
PCL- <i>b</i> -PVBzCl	S	DVB		Suspension	Functionalized nanoporous polymer	[177]
PCL- <i>b</i> -PtBA	S	DVB		Suspension	Functionalized nanoporous polymer	[177]
P4MCL	MMA	EGDMA		Bulk	Photochromic lens	[183]
PMMA	S	DVB	C ₈ mimNtf ₂ , C ₁₂ mimNtf ₂ (saturated with AgCl)	Bulk	Reference electrode	[162]
PVBzCl	S	DVB		Bulk	Anion-exchange resin	[174]
PoSSE	S	DVB		Bulk	Cation-exchange resin	[174]
PnBA	AA	EGDA		Photo	3D-printed composite resin	[214–216]

main growth outspeed order-order transitions. The calculation also predicted an acceleration in the polymerization rate upon microphase separation, which was inconsistent with the experimental results.

Motokawa et al. examined the structure evolution kinetics for the PMMA-*b*-PS system mediated by the RAFT polymerization of styrene-*d*₈ [57,91]. First-order polymerization kinetics up to intermediate conversion supported controlled chain growth, at least in the early stage, while the dispersity of the final polymer was relatively high. In the time-resolved SANS data shown as a function of the scattering vector q , the initial increase in the scattering intensity with the q^{-4} -dependent profile in the low q regime was interpreted as macrophase separation due to PS homopolymer formation. The growth of a broad scattering peak was consistent with the “correlation hole” originating from a diblock polymer in the disordered state [92]. The appearance of a sharp scattering peak marked the onset of microphase separation. The order-disorder transition behavior in the PIMS process is similar to that observed in the temperature-induced microphase separation, where increasing the segregation strength induces chain stretching and generates fluctuation in composition near the critical point (Fig. 4a and b). A body-centered cubic morphology was identified at the end of polymerization by conventional and ultra SANS analyses (Fig. 4c and d). In a separate setting targeting high molar mass synthesis, they observed more order-order transitions into PS-rich phases with increasing conversion (Fig. 4c). Along with the increase in the domain spacing (d), the q dependence in the low q regime shifted from q^{-4} to q^{-2} over time, suggesting the microphase-

separated structure dominates the scattering behavior in the later stage (Fig. 4d). In a later study using PMMA-CTA with ultrahigh molar mass ($M_w = 169 \text{ kg mol}^{-1}$), the authors found microphase-separated structures with large periodicities in the visible light range could be produced in the polymerization mixture that reflected different wavelengths as a function of conversion [93]. The PIMS process may be a practical route to block polymer-based photonic materials by avoiding difficulties associated with the processing of ultrahigh molar mass block polymers [94].

Seo and Hillmyer investigated the PIMS kinetics by copolymerizing a cross-linker to trap an intermediate morphology (Fig. 5) [22]. When styrene and DVB were copolymerized in the presence of PLA-CTA, the P(S-*co*-DVB) block started to grow from the PLA chain end, as evidenced by a gradual shift to higher molar mass over time in the size exclusion chromatography (SEC) traces. The appearance of very high molar mass species followed by gelation indicated cross-linked network formation because of DVB. The remaining monomer was continuously consumed after gelation to yield a solid monolith with >90% yield (Fig. 5b). *In situ* SAXS of the polymerization mixture showed the emergence of a broad scattering peak that retained its position and intensity after saturation (Fig. 5c). The exponential increase in the scattering intensity resembles early-stage spinodal decomposition, characterized as three-dimensional composition fluctuation into bicontinuous domains, that can be described by the Cahn-Hilliard theory (Fig. 5d) [96]. The presence of a maximum in the intensity growth rate profile as a function of q^2 suggested a discrete length scale dominates the structure growth, which coincides to the dimension of

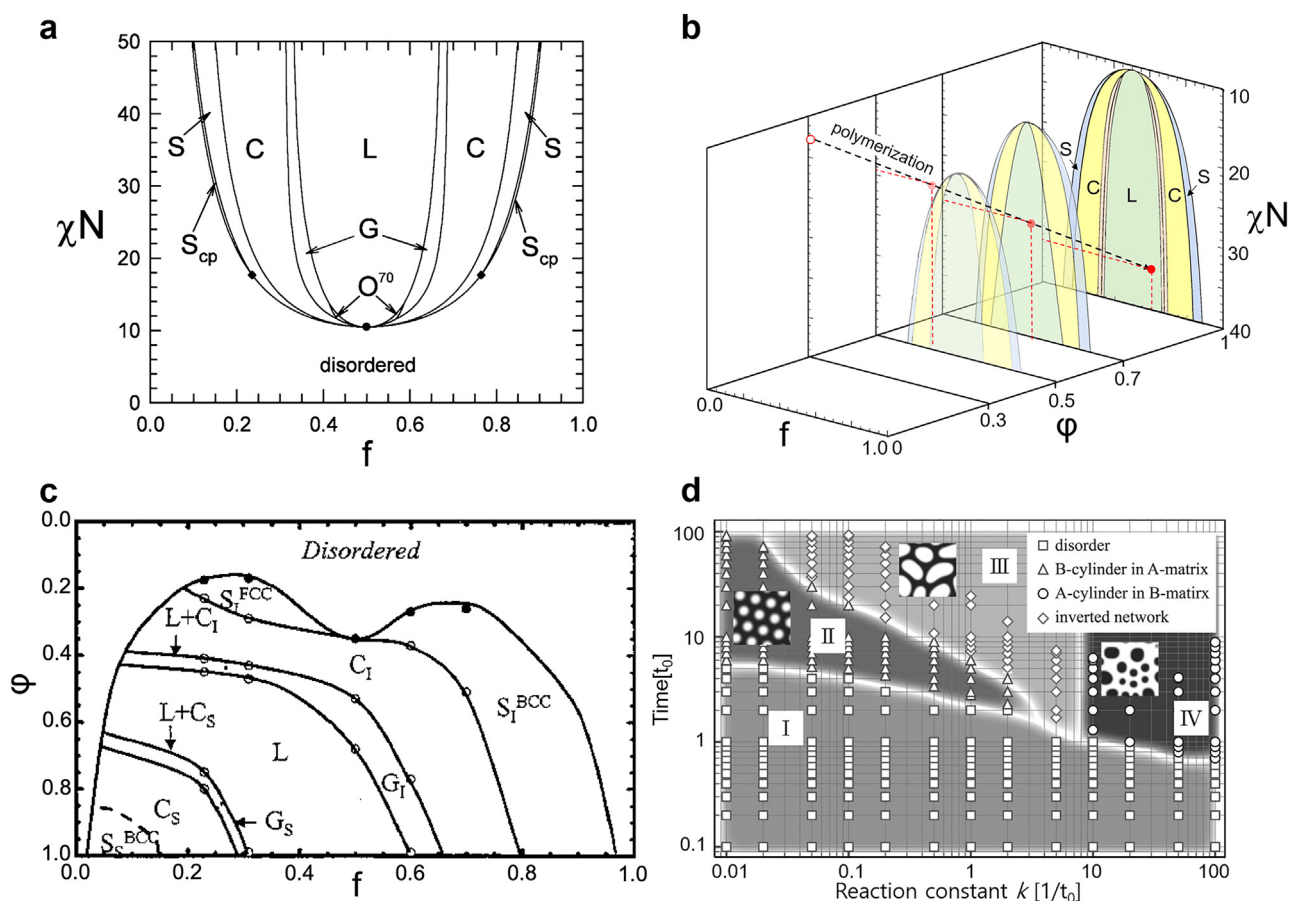


Fig. 3. (a) Phase diagram of an A-B diblock copolymer melt constructed based on the self-consistent mean-field theory. S: sphere; S_{cp} : close-packed sphere; C: cylinder; G: gyroid; O_{70} : $Fddd$; L: lamella [88], Copyright 2012. Reproduced with permission from the American Chemical Society. (b) Imaginary 3D phase diagram illustrating the PIMS process starting with a polymerization mixture of polymer A in monomer b. Because the monomer b also acts as a solvent, the volume concentration (ϕ) was added to the diagram as the x-axis to describe the phase behavior of a block polymer solution according to [89]. The volume fraction of polymer A in the polymerization mixture ($N = 1$) is set to 0.3. An arbitrary reaction trajectory is also shown as a dashed line connecting red dots, assuming that the ordering kinetics is fast enough to reach equilibrium per each monomer addition [89], Copyright 1998. Adapted with permission from the American Chemical Society. (c) Experimentally determined phase diagram of a block polymer solution as functions of f and ϕ . The data of polystyrene-*b*-polyisoprene (PS-*b*-PI) in diethyl phthalate at 100 °C is given as an example. The subscript denotes the polymer block forming the minor phase [90], Copyright 2002. Adapted with permission from the American Chemical Society. (d) Phase transition of the A-*b*-B diblock copolymer by chain extension with monomer b as a function of the polymerization reaction constant. A coarse-grained model in 2D space based on the Ginzburg-Landau expansion coupled with random phase approximation was used for calculation. At the complete conversion, the volume fraction of A is 0.3 [58], Copyright 2008. Reproduced with permission from the American Chemical Society.

the forming block polymer (Fig. 5e) [97,98]. Overall, the results support that the block polymer formation *in situ* drives microphase separation, but simultaneous cross-linking captures the emergent morphology into the disordered bicontinuous structure. Further monomer consumption develops a narrower interface while retaining the morphology and the length scale.

2.2. Factors affecting PIMS

Cross-linker. In the PIMS process, the cross-linker copolymerization provides a means to fix the target morphology spontaneously. The disordered bicontinuous structure PIMS can readily capture with *in situ* cross-linking has attracted prominent attention (Fig. 6a). An active domain with three-dimensional connectivity, responsible for functions such as transport, spares the need for domain alignment and can be combined with a continuous structural framework providing integrity. While the bicontinuous morphology produced by PIMS is topologically similar to those found in spinodally decomposed materials [96,99] and bicontinuous microemulsions [100], the sub-10 nm features of PIMS that emerge spontaneously during polymerization are highly desirable for polymer nanostructuring. High cross-linking density can add additional

stability to the PIMS materials. In comparison, the gyroid structure, representing an ordered version of the bicontinuous morphology, suffers from its narrow phase window for broader applications [101–105]. In addition to the polymerization methodologies to the cocontinuous morphologies discussed earlier [82–87], we note that cross-linking of block polymer materials in the disordered state also produces similarly disordered bicontinuous structures [106].

Schulze et al. investigated the effect of cross-linker loading on the PLA-CTA/styrene/DVB system and showed that the cross-linker content could determine the moment of structure arrest, spanning from disorder to order [107]. An ordered lamellar morphology appeared in the ≤ 2 mol% DVB condition, suggesting gelation occurred after the order-disorder transition. Collapsed layers visualized by scanning electron microscopy (SEM) after PLA removal supports the assignment (Fig. 6b). Given that the PLA weight fraction predicts the cylindrical phase in equilibrium, the lamellar morphology seems trapped by cross-linking. In the intermediate cross-linker content (5 to 40 mol% DVB), a broad principal scattering peak followed by a second-order shoulder characterized the scattering pattern consistent with the disordered bicontinuous morphology with some local order (Fig. 6c). SEM images after PLA etching revealed

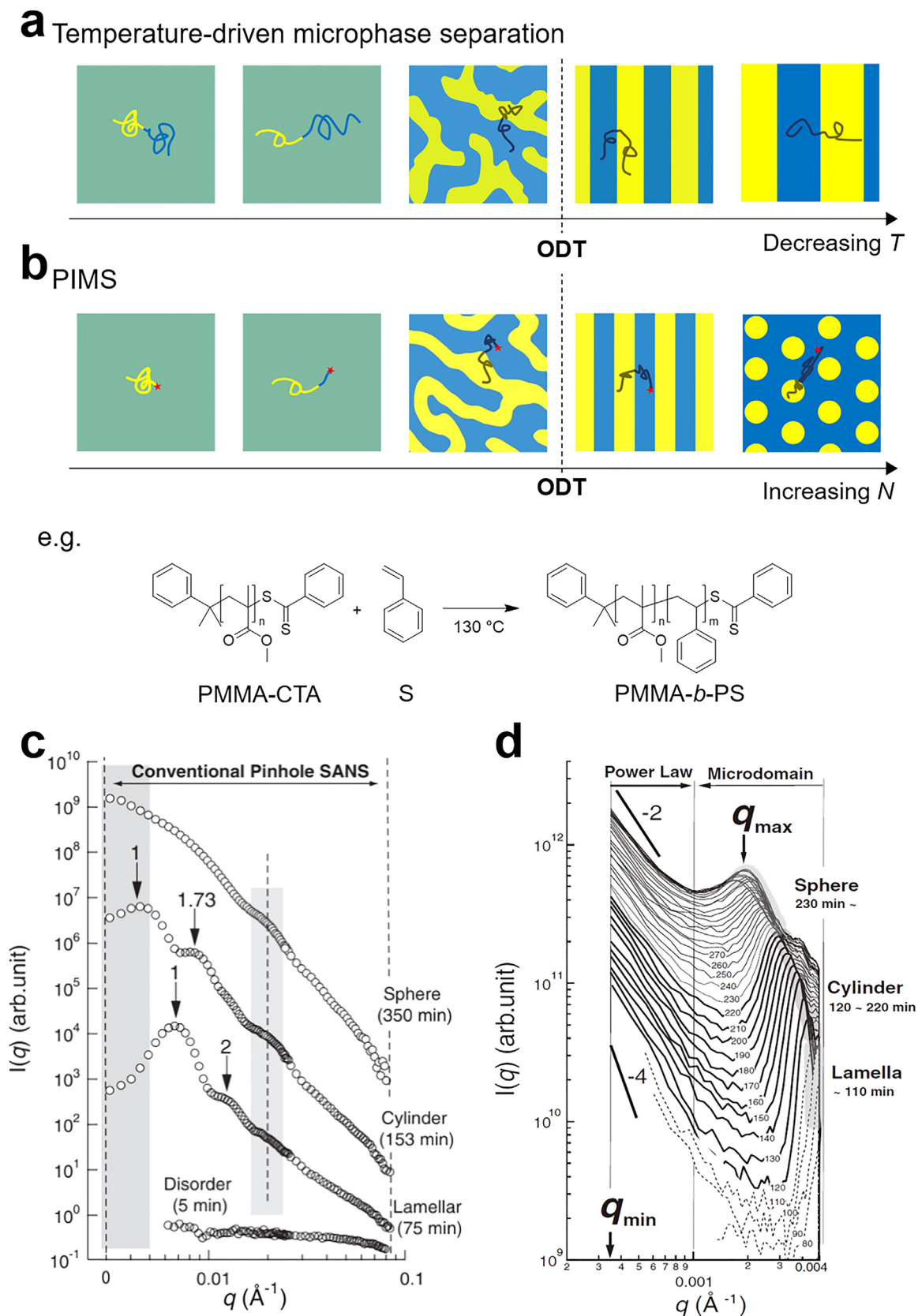
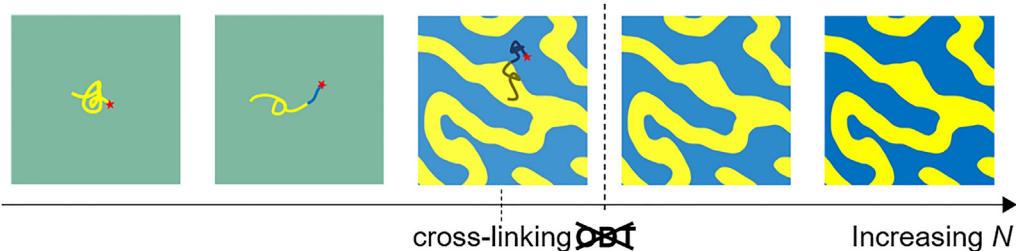


Fig. 4. (a) Illustration of morphological changes during the temperature-driven microphase separation for a symmetric diblock copolymer. (b) Illustration of morphological changes during PIMS at a constant temperature. Note that the yellow polymer becomes a minor block at the full conversion. The drawings were taken from [95], Copyright 1995. Adapted with permission from the American Chemical Society. (c-d) *In situ* SANS (c) and ultra SANS (d) profiles taken during the RAFT polymerization of styrene in the presence of PMMA-CTA (the reaction scheme is shown above) [57], Copyright 2007. Adapted with permission from Springer Nature.

a PIMS with *in situ* cross-linking

e.g.

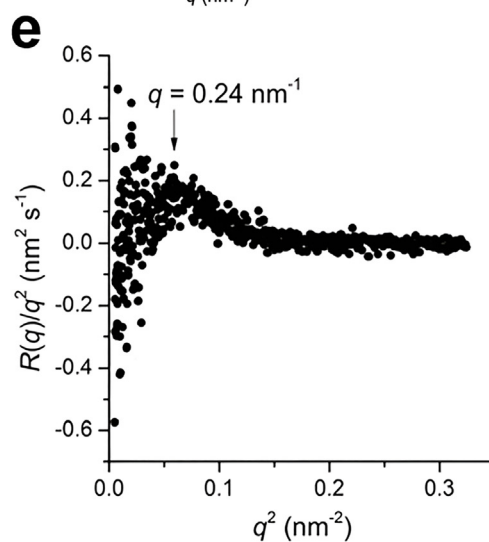
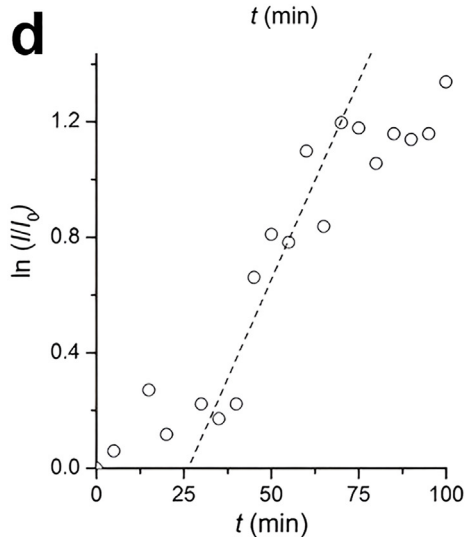
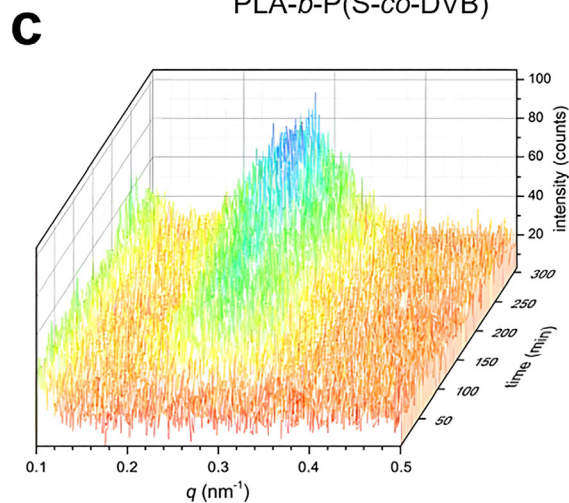
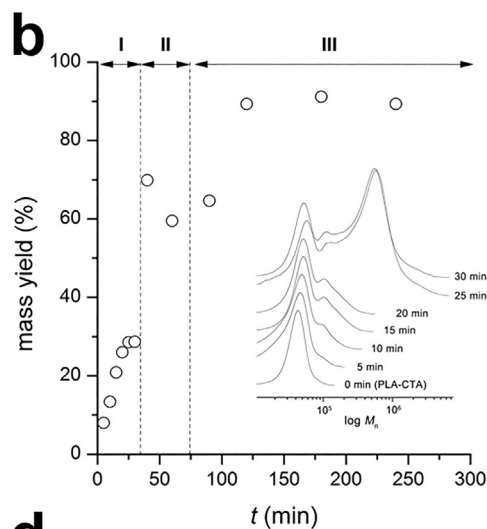
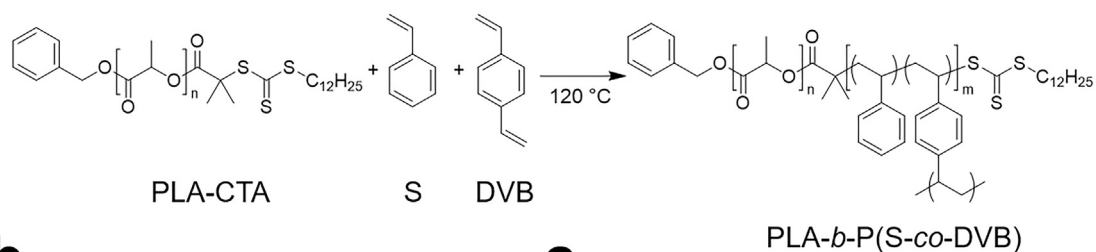


Fig. 5. (a) Effect of *in situ* cross-linking during the PIMS process that arrests the bicontinuous morphology prior to the order-disorder transition. Note that the polymerization proceeds further after gelation developing the narrower interface. The drawings were taken from [95]. Copyright 1995. Adapted with permission from the American Chemical Society. (b-e) PIMS kinetics of the PLA-CTA/styrene/DVB system (the reaction scheme is shown above) [22]. Copyright 2012. Reproduced with permission from the American Association for the Advancement of Science. (b) Mass yield vs. polymerization time plot. I, II, and III correspond to the solution, fragile gel, and monolithic solid phases. An inset shows the SEC traces of the produced polymer for the first 30 min of polymerization. (c) Waterfall overlay of *in situ* 1D SAXS profiles taken during polymerization. (d) Evolution of the normalized SAXS peak intensity at $q = 0.3 \text{ nm}^{-1}$ in the early stage. The dashed line indicates the exponential intensity increase at the onset of phase separation. (e) Plot of $R(q)/q^2$ vs. q^2 . $R(q)$ is the growth rate in the linearized Cahn-Hilliard theory that can be extracted from a slope of the line in (d).

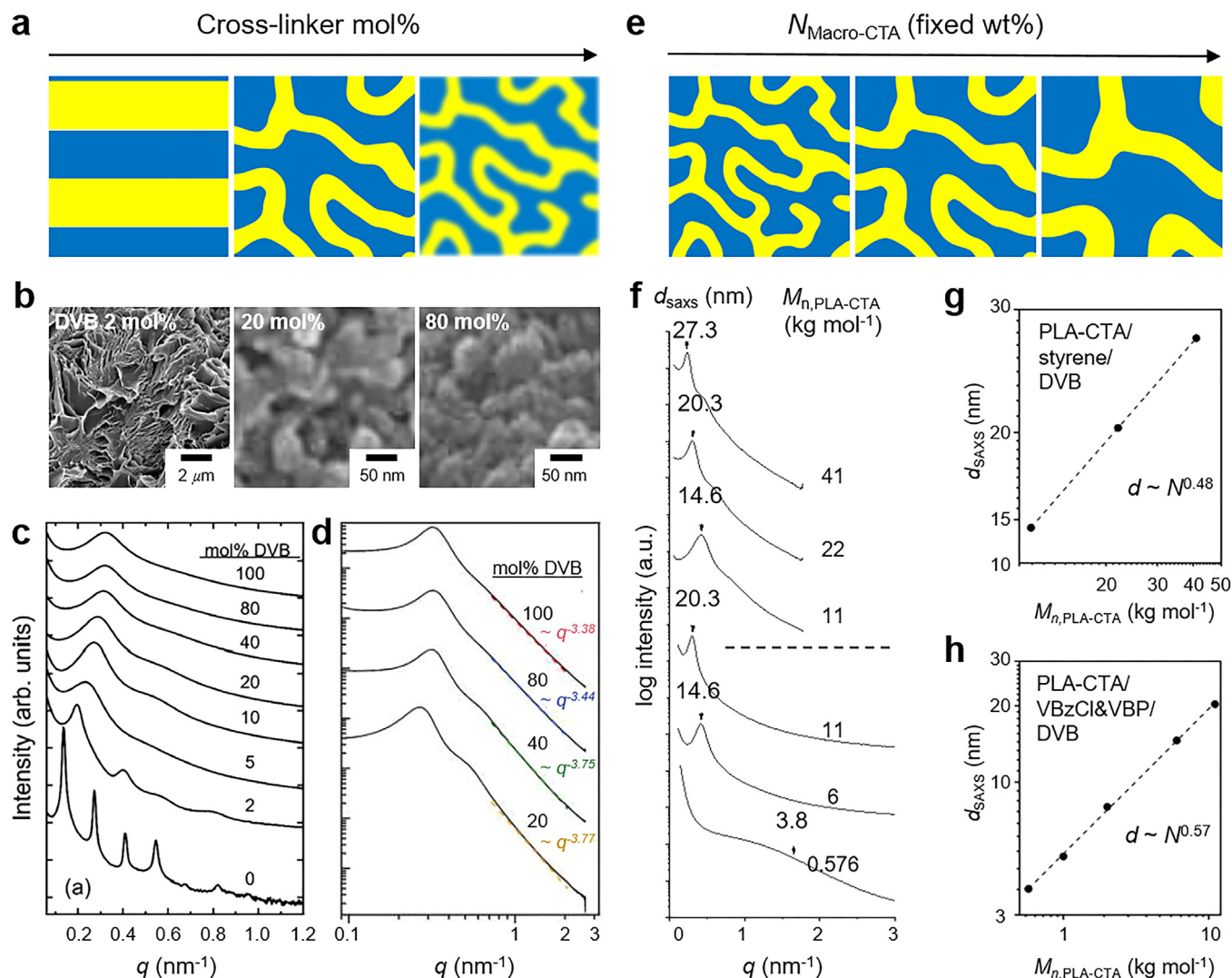


Fig. 6. (a-d) Effect of the cross-linker on PIMS. The data obtained from the PLA-CTA/styrene/DVB system is shown [107], Copyright 2017. Adapted with permission from the American Chemical Society. (a) Schematic illustration of the morphological change as a function of the cross-linker loading. (b) SEM images of the PIMS products. Imaging was performed after PLA removal to generate topographic contrast and Pt coating. (c) SAXS profiles of the PIMS products. The data is vertically shifted for clarity. (d) SAXS plots with the Porod exponents obtained after PLA etching. (e-h) Effect of N on PIMS. [22], Copyright 2012. Adapted with permission from the American Association for the Advancement of Science. [109], Copyright 2021, Adapted with permission from the American Chemical Society. Note that $N_{\text{Macro-CTA}}$ controls the whole N at the fixed weight fraction of the macro-CTA in the polymerization mixture. (e) Schematic illustration of the domain size change as a function of $N_{\text{Macro-CTA}}$. The cross-linker content is assumed to be high enough to arrest the bicontinuous morphology regardless of N . (f) SAXS profiles of the PIMS products obtained from PLA-CTA/styrene/DVB (top) and PLA-CTA/VBzCl&VBP/DVB (bottom). Data reported in [22] and [109] were plotted together. The data is vertically shifted for clarity. d_{SAXS} (nm) are calculated by $d_{\text{SAXS}} = 2\pi/q^*$. (g-h) Double logarithmic plots of d_{SAXS} vs. $M_{n,\text{PLA-CTA}}$ from PLA-CTA/styrene/DVB (g) and PLA-CTA/VBzCl&TMSS/DVB (h). The scaling exponents deduced by linear regression are shown within the plots.

that percolating pores were templated by the PLA domain and supported by the three-dimensional continuous framework. Broadening of the principal peak with the vanishing second-order shoulder above 40 mol% DVB indicates early arrest results in the less-ordered morphologies. The decrease in the Porod exponent at high q with the increasing DVB fraction supports the increase in interface roughness (Fig. 6d). Semispherical nodules constituting the framework at high DVB loading were observed by SEM and attributed to microgel formation due to extensive intramolecular cyclization.

Degree of polymerization N . Like conventional block polymer systems, the domain size of PIMS materials can be controlled by N . Assuming RAFT polymerization in action, varying the molar mass of the macro-CTA while keeping its weight fraction in the polymerization mixture furnishes PIMS materials with tunable d (\sim domain size) at identical composition (Fig. 6e).

The d dependence on N has been investigated in the PLA-CTA/styrene/DVB system at 20 mol% DVB loading (Fig. 6f) [22]. A linear relationship appears in the double logarithmic plot with a scaling exponent of 0.48 (Fig. 6g). This value is close to 0.5, which is observed in the weak segregation limit near the order-disorder transition [108]. A similar system composed of PLA-CTA/4-vinylbenzyl chloride (VBzCl)&4-vinylbiphenyl (VBP)/DVB also yielded 0.57 as the scaling exponent at the same DVB content supporting that the arrest occurs in the disordered state with less extended chain conformation (Fig. 6h) [109]. The d value of PIMS materials is also much smaller than conventional block polymers with comparable molar masses. For example, PLA-*b*-PS containing 30 wt% PLA and synthesized with PLA-CTA of number-average molar mass (M_n) = 22 kg mol⁻¹ forms a hexagonally packed cylindrical morphology with $q^* = 0.15$ nm⁻¹ [110]. When the same PLA-CTA is loaded in the PIMS solution

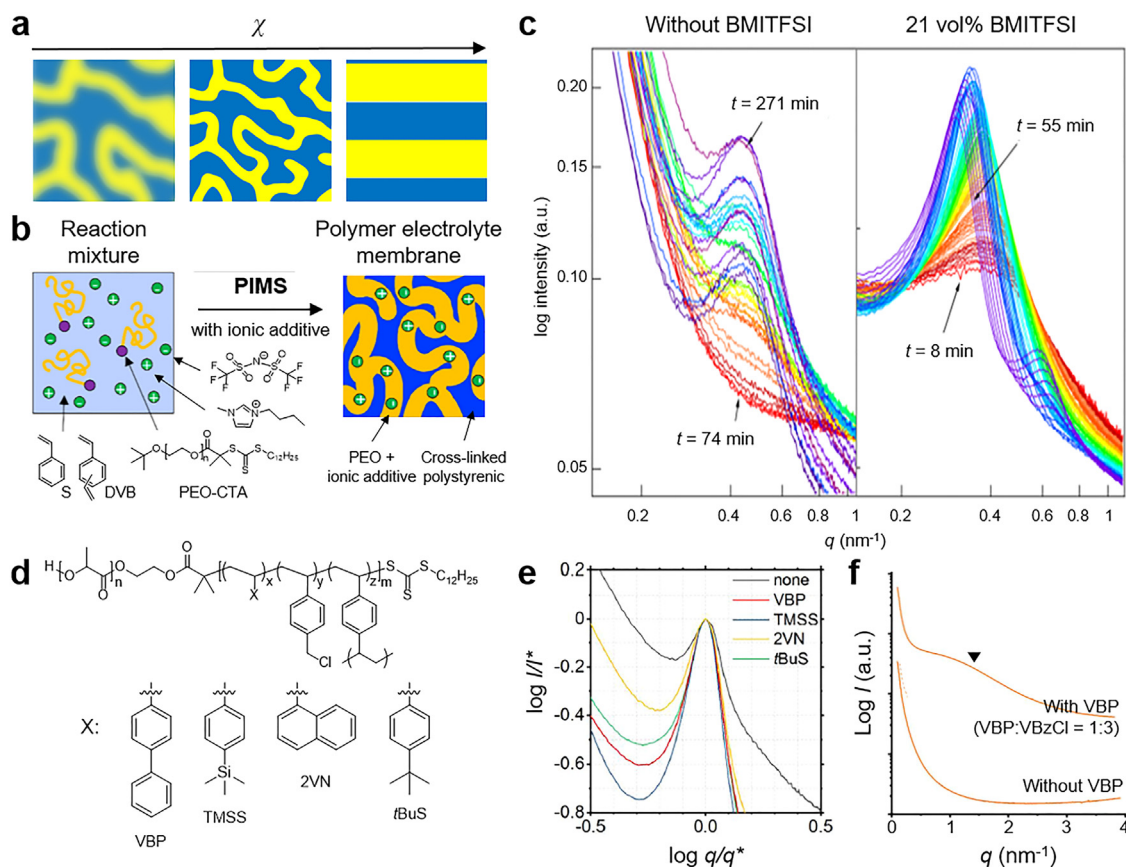


Fig. 7. χ effect on PIMS. (a) Possible morphological change with the increasing χ . (b-c) Adding BMITFSI to the PEO-CTA/styrene/DVB system increases χ by the preferential partition of the ionic liquid in the PEO domain upon polymerization [111], Copyright 2015. Adapted with permission from the American Chemical Society. (b) Schematic illustration for the PIMS process. (c) SAXS profiles taken during polymerization *in situ* without (left) and with 21 vol% of BMITFSI (right). (d-f) Increasing χ by copolymerizing with a high- χ comonomer in the PLA-CTA/VBzCl/DVB formulation [109], Copyright 2021. Adapted with permission from the American Chemical Society. (d) Chemical structure of the PIMS products with tested comonomers. (e) Overlay of scaled log-log SAXS profiles of the PIMS products obtained with different comonomers. PLA-CTA weight fraction and DVB loading were fixed as 30 wt% and 20 mol%, respectively. $M_{n, \text{PLA-CTA}} = 2 \text{ kg mol}^{-1}$. (f) SAXS data of the PIMS products obtained without VBP (bottom) and with VBP (top, [VBP]:[VBzCl] = 1:3). $M_{n, \text{PLA-CTA}} = 576 \text{ g mol}^{-1}$.

with styrene and DVB, q^* of 0.30 nm^{-1} is obtained in the resulting monolith at 20 mol% DVB loading, corresponding to the PLA domain size of $< 7 \text{ nm}$. The lower d value suggests that PLA chains adopt less stretched conformation at the onset of gelation because the segregation strength is lower than fully polymerized PLA-*b*-PS, and the polystyrenic globules formed by cross-linking creates a larger interfacial area to cover. The domain size can further decrease by increasing the DVB loading. The facile access to sub-10 nm domains is another advantage of the PIMS process. Practically, increasing the length scale by using higher-molar mass macro-CTAs is more challenging because of viscosity.

Interaction parameter. High χ between the macro-CTA and the growing block allows the system to enter the ordered phase early and develop a narrow interface (Fig. 7a). However, preparing a homogeneous polymerization mixture would not be possible if χ is too high because the monomer would be highly incompatible with the macro-CTA. Adding a selective additive and a comonomer has been reported in the literature to increase χ of the PIMS system.

McIntosh et al. investigated the effect of bis(trifluoromethylsulfonyl)imide (BMITFSI) as an additive to the PEO-CTA/styrene/DVB system (Fig. 7b-d) [111]. BMITFSI is an ionic liquid that is PEO-philic and miscible with the polymerization mixture but immiscible with PS [112–114]. In the *in situ* SAXS profile, the scattering intensity developed rapidly in the presence of BMITFSI into a narrower peak at lower q (Fig. 7d). The incompatibility of BMITFSI to the growing polystyrenic block

seems to promote microphase separation by selective partitioning of BMITFSI in the PEO domain, which increases χ between PEO (swollen with BMITFSI) and P(S-co-DVB) blocks. The authors estimated the effective χ increases by a factor of 1.5 ($\chi_{\text{PS/PEO}}$ is ~ 0.065 at 25°C and ~ 0.048 at 120°C , which is the polymerization temperature). They further predicted that microphase separation occurs before gelation in the presence of BMITFSI, while gelation precedes in the pristine PEO-CTA/styrene/DVB system. Yet the bicontinuous morphology composed of ion-conductive and cross-linked domains lacking long-range order could be arrested, presumably by preventing relaxation to morphological equilibrium.

Lee and Seo examined VBP, trimethylsilylstyrene (TMSS), 2-vinylnaphthalene (2VN), and *tert*-butylstyrene (tBuS) as high- χ comonomers in the PLA-CTA/VBzCl/DVB system (Fig. 7e and f) [109]. All the PIMS products synthesized with the comonomers showed narrower peak widths in the scaled log-log SAXS profile compared to the virgin, consistent with the increased χ (Fig. 7e). VBP was studied further to evaluate the lower limit of N in PIMS. While almost a featureless SAXS pattern was obtained without the comonomer when PLA-CTA with M_n of 576 g mol^{-1} (obtained by iterative synthesis) was used, a pronounced peak intensity from the VBP-containing product supported the presence of the microphase-separated morphology driven by higher χ (Fig. 7f).

Additive. A polymer without the CTA motif at the chain end can be a selective additive in the PIMS process. Like homopolymer/diblock copolymer blends, the phase behavior is primarily in-

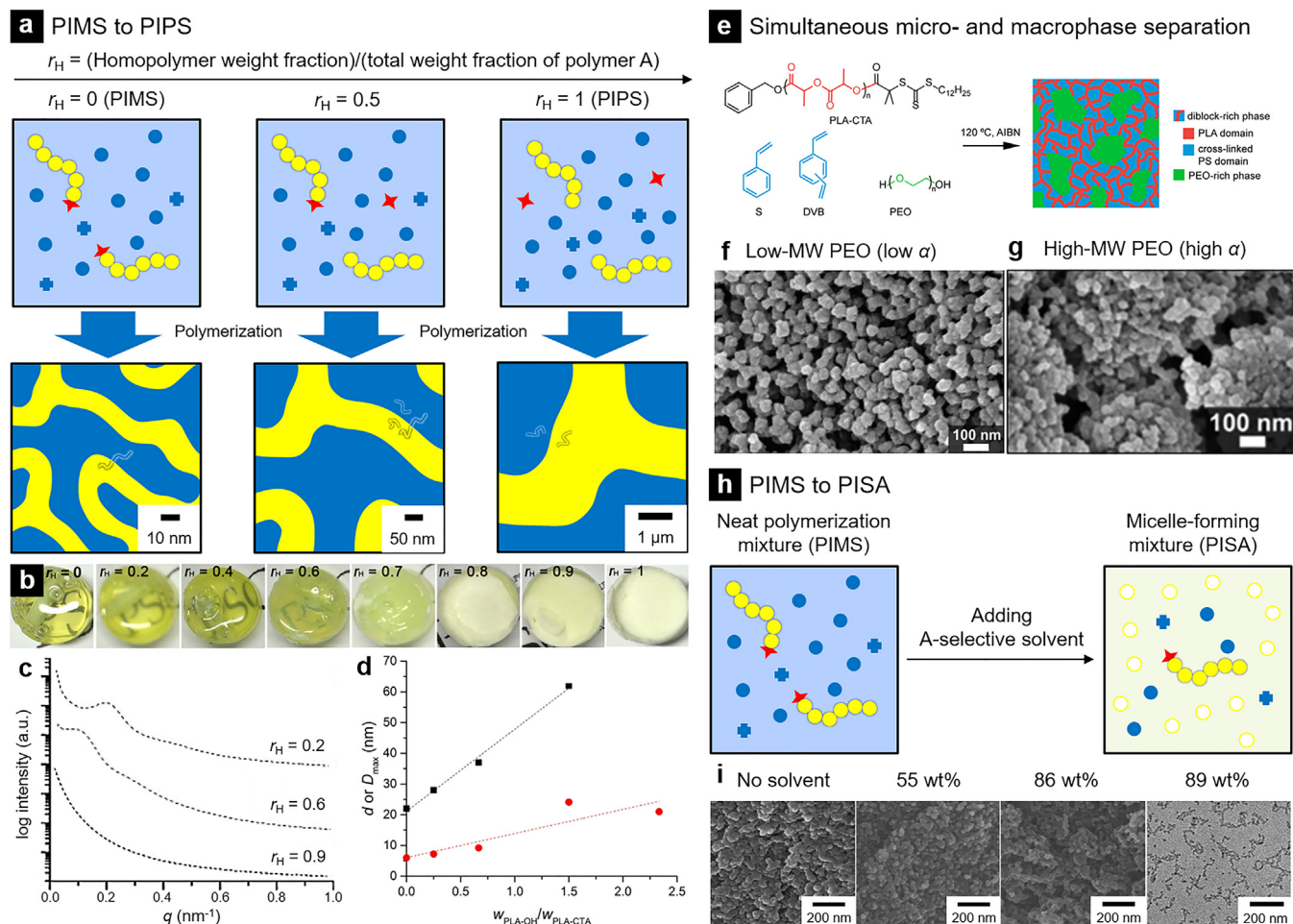


Fig. 8. (a–d) Transition from PIMS to PIPS by adding homopolymer to the polymerization mixture [72], Copyright 2017. Adapted with permission from Elsevier Science Ltd. (a) Schematic illustration of the characteristic length scale change with the increasing homopolymer fraction expressed as r_H . This scenario assumes the small molecular propagating center is added to keep the propagating center concentration constant (Series 2 in [72]). Without this, depletion of the propagating center at high r_H results in poor control over polymerization (Series 1 in [72]). (b) Photos of the PIMS products from PLA-CTA/styrene/DVB with the increasing fraction of PLA homopolymer (PLA-OH). (c) Representative 1D SAXS profiles. The data is vertically shifted for clarity. (d) d and mean pore size (D_{max} , estimated by the nitrogen sorption analysis after PLA etching) as a function of the weight fraction ratio of PLA-OH to PLA-CTA. (e–g) Simultaneous micro- and macrophase separation above the solubility limit with a high-molar mass additive. PEO was used as a PLA-selective additive in the PLA-CTA/styrene/DVB formulation ($M_{n,\text{PLA-CTA}} = 31 \text{ kg mol}^{-1}$) [115], Copyright 2015. Reproduced with permission from the American Chemical Society. (f) SEM image taken after PLA&PEO removal showing the swollen PLA domain with low- α 5 kg mol⁻¹ PEO (30 vol%). (g) SEM image indicative of micro- and macrophase separation when high- α 35 kg mol⁻¹ PEO (50 vol%) was used. (h–i) Transition from PIMS to PISA by adding the A-selective solvent [73], Copyright 2020. Adapted with permission from the Royal Society of Chemistry. (h) Schematic illustration. (i) SEM (after PLA/acetonitrile removal) and TEM images of the PIMS/PISA products obtained with the PLA-CTA/styrene/DVB system with the increasing acetonitrile weight fraction in the system as the PLA-selective solvent.

fluenced by the composition and relative molar mass of the homopolymer to the relevant block (typically denoted α in the literature). The block copolymer microdomain can accommodate the same polymer additive, but macrophase separation occurs above the solubility limit into homopolymer-rich and block copolymer-rich phases. The homopolymer with higher molar mass pushes macrophase separation (especially when $\alpha > 1$) because of the increasing entropic penalty to keep the longer homopolymer chain inside the microdomain with limited conformational freedom.

Park et al. systematically studied the effect of homopolymer in the PLA-CTA/styrene/DVB system at a constant PLA weight loading (Fig. 8a–d) [72]. When PLA homopolymer with the same molar mass as PLA-CTA was used, a gradually changing visual of the PIMS products from transparent to opaque evidenced a transition from PIMS to PIPS with the increasing PLA homopolymer fraction (Fig. 8b). While control of the morphology and the domain length scale was relatively poor at high PLA homopolymer contents, presumably because of low CTA concentration in the system, adding a molecular CTA improved the control in the full range and retained the bicontinuous morphology up to the micrometer length scale

(Fig. 8c and d). A lower molar mass PLA homopolymer ($\alpha < 1$) could increase the PLA weight fraction without macrophase separation. Macrophase separation occurred at $\alpha > 1$ along with PIMS, which resulted in the PLA homopolymer phase coexisting with the microphase-separated domains. Hierarchically porous polymers containing pores at nanometer and micrometer length scales were produced after PLA removal. In an earlier study, Saba et al. also observed similar behavior with PEO homopolymer as an additive to the PLA-CTA/styrene/DVB system (Fig. 8e–g) [115]. PEO forms a miscible blend with PLA in the entire composition range, and the basic treatment can simultaneously remove both PLA and PEO homopolymer. Swelling of the PLA domain and simultaneous micro- and macrophase separation as a function of PEO molar mass corroborates the profound impact of α in homopolymer-containing PIMS systems.

In addition to ionic liquids, acetonitrile has been reported as a small molar mass additive in the PLA-CTA/styrene/DVB system that preferentially swells the PLA domain (Fig. 8h and i) [73]. Acetonitrile with more than 25-fold volume of PLA could be added to the polymerization mixture and yet yield a monolithic PIMS product

with the increased PLA domain size. PISA occurred in the further diluted polymerization mixture with acetonitrile and produced block polymer micelles composed of cross-linked polystyrenic core and PLA corona. Accelerated polymerization rate and formation of elongated and branched micellar morphologies in the presence of DVB suggested that cross-linking helps segregation of the micellar core in the early stage of the reaction and contributes to bridging the cores via inter-core cross-propagation.

Simultaneous block polymerization/gradient copolymerization. While most PIMS examples have utilized a macro-CTA containing a presynthesized polymer block, an intriguing approach has been reported by Seo et al. showing that PIMS can occur when both blocks are simultaneously polymerized [116]. The one-shot block polymerization was achieved using a hydroxyl-functionalized trithiocarbonate as a RAFT CTA carrying an initiating site for ring-opening esterification polymerization (ROTEP) of D,L-LACTIDEALDIDE. The authors confirmed that PS-*b*-PLA can be obtained by sequential RAFT-ROTEP, ROTEP-RAFT, and simultaneous RAFT-ROTEP by using Sn(II) 2-ethylhexanoate as the ROTEP catalyst. The one-shot polymerization of styrene, DVB, and D,L-LACTIDE did afford a cross-linked block polymer monolith that could be transformed into a nanoporous polymer upon PLA removal. However, a clear principal scattering peak corresponding to the block polymer length scale was not discerned in the SAXS analysis, suggesting that the limited control over the RAFT polymerization might have generated heterogeneity at the larger length scale.

A computational approach based on the dissipative particle dynamics simulations also suggested that controlled copolymerization of styrene and 4-vinylpyridine (4VP) can induce microphase separation because of the composition drift [117]. The much higher reactivity ratio of styrene ($r_S = 17.39$, $r_{4VP} = 0.058$) leads to the formation of gradient copolymers composed of the PS-rich and nearly pure P4VP blocks. The authors found that the order-disorder transition occurred above critical conversion, which was influenced by the composition and target N of the polymerization mixture. At the order-disorder transition, χN was linearly proportional to the target N . Various microphase-separated and lyotropic morphologies could be predicted. While experimentally not verified yet, the sequence control based on the monomer reactivity could be a valuable platform for the synthesis of block polymer materials via one-step PIMS.

3. PIMS-based materials

As pointed out earlier, the PIMS approach was originally developed for the synthesis of robust mesoporous polymer monoliths with percolating, sub-10 nm mesopores. More applications have emerged by harnessing the bicontinuous morphology captured by *in situ* cross-linking and synergistically combining the component functions. Postpolymerization modification and interfacial tuning further diversified material composition attainable via PIMS. This chapter reviews the materials produced based on the PIMS methodology.

3.1. Nanoporous polymers

Nanoporous polymers are useful for separation, storage, and heterogeneous catalysis applications [118,119]. PIPS in the presence of a porogenic diluent is commercially used to prepare macroporous beads and monolithic columns with interconnected macropores for chromatography [35,42,120–123]. However, with the macrophase separation-based methodology, downscaling pore size below 100 nm with reliable control is challenging. Block polymer-based approaches are a unique route to well-defined nanoporous polymers with control over pore size, comparable to inorganic counterparts such as mesoporous silica, yet taking advantage of

compositional diversity and high processability of polymeric materials [124,125]. Selective removal of the sacrificial block in the microphase-separated block polymer precursor is particularly appealing as the block polymer morphology persists during etching and thus precisely dictates the pore structure and pore size [126–128].

With the PLA-CTA/styrene/DVB combination, Seo and Hillmyer showed that the disordered bicontinuous morphology derived by the PIMS process could be converted into a 3D continuous pore structure (Fig. 9a) [22]. In a typical run, PLA-CTA was dissolved in a mixture of styrene and DVB (4:1 in molar ratio) to make a 30 wt% solution. Heating up to 120 °C initiated the RAFT polymerization by spontaneous radical generation via the Diels-Alder reaction of styrene ("autoinitiation"). Solidification of the whole polymerization mixture yielded a monolithic precursor molded by the shape of the polymerization vessel. High transparency to visible light supported the absence of macroscopic heterogeneity typical in PIPS, indicating that the block polymerization successfully confined the length scale to the nanometer level. The yellow color of the precursor originated from the trithiocarbonate group in the CTA motif. PLA was chosen because it could be readily etched out in the basic condition (e.g., 0.5 M NaOH solution in a water/methanol mixture). Complete removal of PLA was confirmed by FTIR (Fig. 9b), differential scanning calorimetry (DSC, Fig. 9c), and gravimetric weight loss measurements. A quarter coin-sized monolith could be rendered porous while retaining the original shape, supporting the bicontinuity of PLA and P(S-*co*-DVB) microdomains (Fig. 9d). Otherwise, the complete PLA etching would be impossible, or the pore structure would collapse. SEM imaging showed that the 3D continuous nanopore structure without long-range order uniformly appears in the entire sample. Mesopores develop exclusively in the nanoporous polymer in contrast to the PIPS-based macroporous materials (Fig. 9f and g).

PIMS was a breakthrough in nanoporous polymer synthesis that opened up easy access to 3D continuous mesopore structure, which has been mostly limited to the gyroidal template suffering from a narrow phase window. The pore continuity was tested by gas and water permeation experiments. The gas permeation profiles were consistent with the Knudsen diffusion (Fig. 9h) [129]. The tortuosity factor accounting for the increased path length compared to a straight channel was estimated as 1.7, which is within the predicted range for small molecule transport through disordered, cocontinuous composites. The water permeation test based on the Poiseuille model also gave a tortuosity of 1.4 (Fig. 9i) [130].

Another benefit of PIMS is *in situ* cross-linking can stabilize pores smaller than 10 nm, challenging for block polymer-based nanoporous polymers. As Laplace pressure increases with the decreasing pore size, smaller pores are more likely to collapse and release the excess surface free energy as heat [131,132]. The densely cross-linked P(S-*co*-DVB) domain provides a rigid framework that prevents pore collapse and renders robust mechanical properties. The virtually identical SAXS pattern with a huge increase in the scattering intensity after PLA etching indicated the increased electronic density contrast to P(S-*co*-DVB), consistent with transforming the PLA domain into a void with retention of the parent morphology (Fig. 10a). The lack of an endothermic transition in the first heating cycle of the nanoporous polymer supports that the pore collapse is prevented (Fig. 9c). The correlation of the SAXS domain spacing to the PLA molar mass also persists in the nanoporous polymer state, indicating robust control over the pore size can be possible.

Seo and Hillmyer evaluated the pore characteristics of nanoporous monoliths obtained with 20 mol% DVB loading by nitrogen sorption isotherm analysis at 77 K (Fig. 10b). A large N₂ uptake at high relative pressure supported the presence of mesopores (in 2 – 50 nm) via capillary condensation. An H2-type hystere-

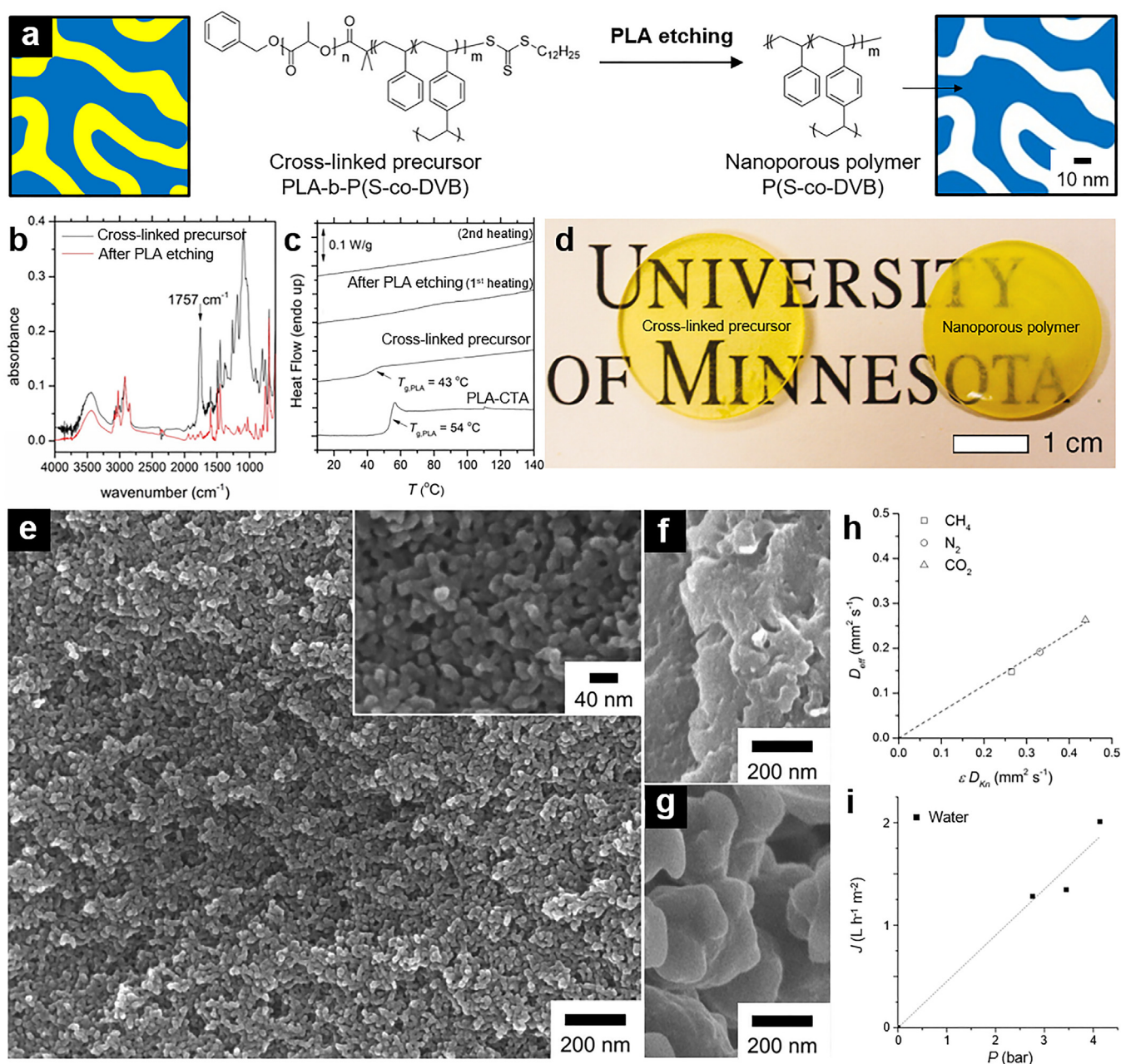


Fig. 9. PIMS-based nanoporous polymer synthesis [22], Copyright 2012. Adapted with permission from the American Association for the Advancement of Science. (a) Conversion of the cross-linked precursor produced by PIMS of PLA-CTA/styrene/DVB into a nanoporous polymer by PLA removal in the basic condition. (b) FTIR spectra before and after PLA etching. An arrow marks the C = O vibrational band originating from PLA. (c) DSC thermograms of PLA-CTA, the cross-linked precursor, and the nanoporous polymer. The data were obtained during the second heating cycle. For the nanoporous polymer, the data during the first heating cycle is also shown. (d) Photo of the cross-linked precursor and the nanoporous polymer. The precursor was molded and milled into the size of a quarter coin. (e) SEM image of the nanoporous polymer obtained with 22 kg mol⁻¹ PLA-CTA. Imaging was performed after Pt coating. An inset shows a high-magnification image. (f-g) SEM images of PIPS products obtained from PLA/styrene/DVB (f) and PLA/styrene/DVB with a molecular CTA (g; this is essentially identical to the $r_H = 1$ case shown in Fig. 8b). Images were taken after PLA etching and Pt coating. (h) Gas permeation data to deduce tortuosity (τ) of the nanoporous polymer based on Knudsen diffusion model. (i) Pressure drop vs. flux plot for water permeation. The nanoporous polymer synthesized with 41 kg mol⁻¹ PLA-CTA was used for the permeability measurements.

sis was consistent with the porous network structure [133]. The “open” gap between the adsorption and desorption branches was attributed to the trapped N₂ in the P(S-co-DVB) matrix [134]. By varying the PLA molar mass from 11 to 41 kg mol⁻¹, the average pore size estimated by the Barrett-Joyner-Halenda (BJH) model increased from 4 to 8 nm (Fig. 10c) [135]. The trend was in good agreement with the domain spacing change of 15 to 27 nm determined by SAXS. We note that the BJH model assumes 1D infinite porous cylinders and tends to reflect “pore neck” size when applied to the interconnected pores. The Brunauer-Emmett-Teller

(BET) specific surface area was on the order of 100 m² g⁻¹ for all the polymers, also consistent with the mesoporous nature [136].

Schulze et al. examined the effect of DVB loading on pore characteristics (Fig. 10d-f) [117]. The higher cross-linking density was critical for preserving smaller pores derived from lower molar mass PLA-CTAs. When 8 kg mol⁻¹ PLA-CTA was used with 20 mol% DVB, the pronounced SAXS intensity at lower q was consistent with the increased heterogeneity at large length scales caused by pore collapse (Fig. 10d). Only negligible N₂ uptake corroborated pore collapse during PLA etching (Fig. 10e). A significant frac-

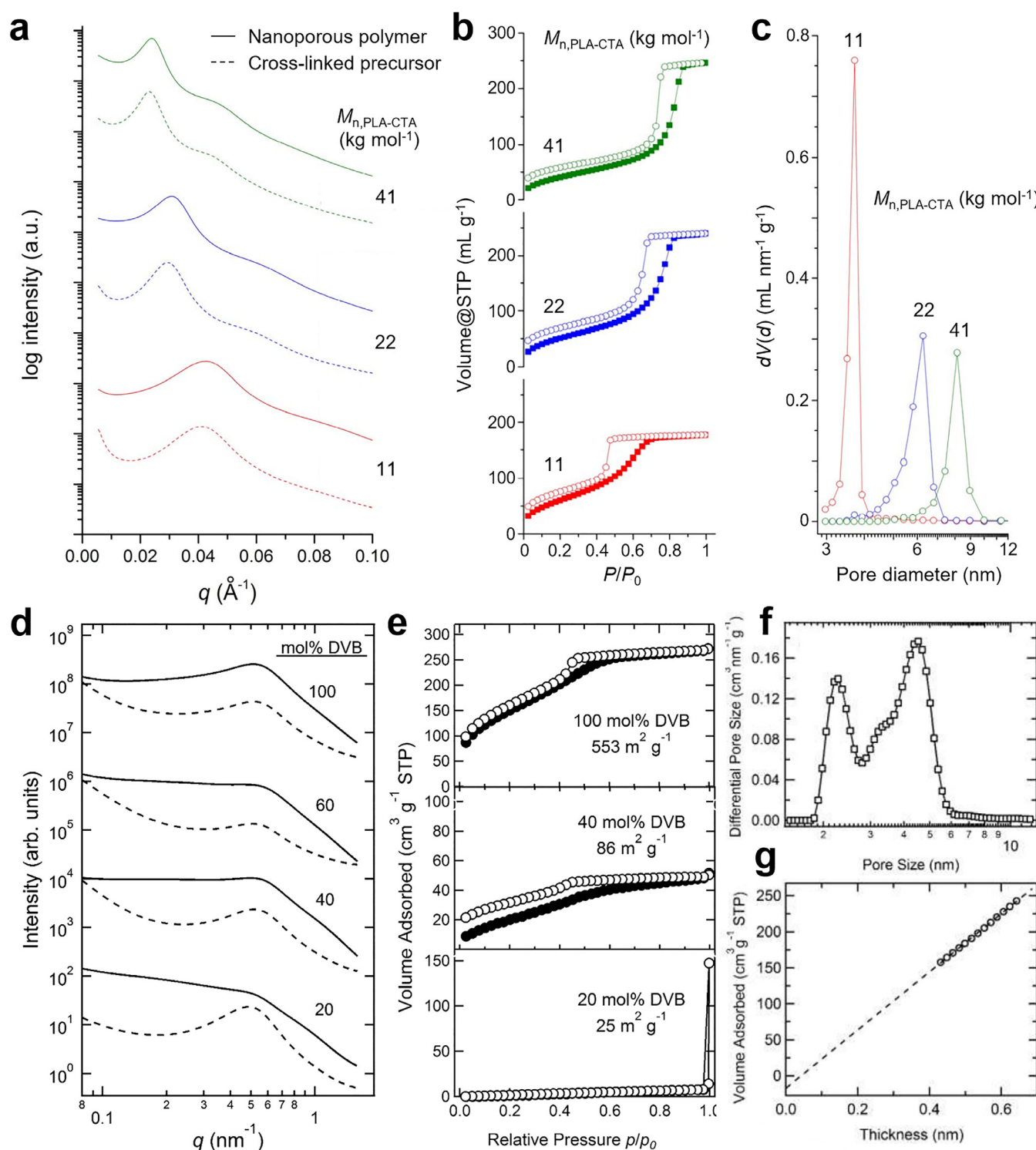


Fig. 10. Control of pore size and stability. (a–c) Pore size control as a function of PLA-CTA molar mass. DVB loading was 20 mol% [22], Copyright 2012. Adapted with permission from the American Association for the Advancement of Science. (a) SAXS data before (dashed line) and after PLA etching (solid line). (b) Nitrogen sorption isotherms. Filled symbol: adsorption branch; Open symbol: desorption branch. (c) BJH pore size distribution from the desorption branch. (d–g) Pore stability as a function of DVB mol%. PLA-CTA of 8 kg mol⁻¹ was used [117], Copyright 2017, Adapted with permission from the American Chemical Society. (d) SAXS data before (dashed line) and after PLA etching (solid line). (e) Nitrogen sorption isotherms. Filled symbol: adsorption branch; Open symbol: desorption branch. (f) QSDFT pore size distribution for 8 kg mol⁻¹ of PLA-CTA at 100 mol% DVB. (g) t-plot analysis.

tion of pores survived above 60 mol% DVB loading. In general, increasing the DVB content declined the slope of the adsorption branch in the hysteresis regime (more H2-like), indicative of the more winding pore structure with less order. An increase in the N₂ uptake at low relative pressures ($P/P_0 < 0.1$) was attributed

to the formation of pores within the P(S-co-DVB) framework. The pore size estimated by nonlocal or quenched solid density functional theory (NL- or QSDFT) analysis of the nitrogen adsorption isotherms supported the broadened pore size distribution and population of 2–3 nm pores (Fig. 10f) while the t-plot analysis did

not reveal microporosity (Fig. 10 g). All the pores were lost at 2 kg mol⁻¹ PLA-CTA even with 100 mol% DVB, limiting down-scaling pore size further and accessing the microporous regime (< 2 nm).

Creating micropores smaller than 2 nm within the framework can produce hierarchically porous polymers containing micro- and mesopores. The 3D continuous mesopore structure built by PIMS allows molecules to diffuse rapidly and access the large surface area provided by the micropores, improving adsorption and reaction kinetics. Larsen et al. used styrenic monomers containing sterically demanding groups at the *para* position to replace styrene in the PLA-CTA/styrene/DVB system to create intrinsic microporosity as permanent free volume within the cross-linked polystyrenic domain (Fig. 11a) [137]. They found that monomers providing higher glass transition temperature (T_g), such as tBuS and TMSS, increased the BET surface area after PLA etching by creating additional pores in the 2–5 nm range in the QSDFT distribution (Fig. 11b–d). Negligible N₂ uptake before PLA removal indicated that the pores are only accessible through the mesoporous space.

Satheeshkumar and Seo designed rigid multifunctional cross-linkers containing biphenyl units and used them instead of DVB (Fig. 11e–h) [138]. *N,N*-dimethylformamide (DMF) was added as a solvent to make a homogeneous polymerization mixture because the cross-linkers were solids insoluble in styrene. Nonetheless, bicontinuously nanostructured materials were obtained consistent with the PIMS mechanism and turned porous by PLA etching. 1,3,5-Tris(4-vinylphenyl) benzene (3VBP) and tetrakis(4-vinylbiphenyl)methane (4VBM) containing three and four styrenic double bonds generated noticeable micropores, as evidenced by the N₂ uptake at very low relative pressure, presumably by constructing a rigid cross-linked network with the expanded interchain distance (Fig. 11f and g). Consistent with Larsen et al., the micropores were not detectable without PLA etching. The cross-linkers were also more effective in reinforcing the framework against Laplace pressure and retaining smaller mesopores. Satheeshkumar et al. synthesized 2,3,6,7,10,11-hexakis(4-vinylphenyl)triphenylene, a triphenylene-based hexavinyl cross-linker, to utilize further the fluorescent feature of the extended π -conjugated system (Fig. 11f and h) [139]. A hierarchically porous monolith containing micropores within the mesoporous wall was obtained, showing strong bluish fluorescence originating from triphenylene under UV. Exposing the monolith to organic solutions containing nitroaromatics turned off the fluorescence. Faster and more efficient fluorescence quenching compared to nonporous solid analog suggests the potential as a robust and reusable sensing platform.

Hyper-cross-linking was combined with PIMS to produce hierarchically porous polymers containing micro- and mesopores (Fig. 12). Typically, hyper-cross-linking involves Friedel-Crafts alkylation of aromatic molecules in the presence of Lewis acid such as FeCl₃ (Fig. 12a) [140]. PVBzCl having benzyl chloride pendants along the polystyrenic main chain is a well-known precursor for hyper-cross-linking, where the benzyl carbocation attacks other aromatic rings to form a rigid cross-linked network bridged by the methylene unit. In the swollen state by a solvent, the reaction permanently arrests the interchain free volume into micropores. External agents capable of methylene insertion, such as formaldehyde dimethyl acetal, can also be used to hyper-cross-link polystyrene [141].

Seo et al. investigated PIMS of the PLA-CTA/VBzCl/DVB system (Fig. 12b) [143]. After obtaining the monolithic precursor composed of PLA and P(VBzCl-co-DVB) bicontinuous microdomains, swelling the precursor in 1,2-dichloroethane and reacting with FeCl₃ produced hierarchically porous polymers in a powdery form. SEM visualized the 3D continuous mesopore structure characteristic of PIMS, indicating degradation of PLA by FeCl₃ through C–O

bond cleavage (Fig. 12c). While micropores were not visible in SEM after Pt coating, TEM imaging in a later study corroborated the coexistence of white micropores within the black mesoporous framework and gray mesopores (Fig. 12d) [109]. SAXS analysis also supported that the PIMS morphology was retained during hyper-cross-linking as in the case of basic etching (Fig. 12e). A massive uptake at very low relative pressure in the nitrogen sorption isotherm confirmed abundant micropores occupying ~0.3 mL g⁻¹ in volume and 600 m² g⁻¹ in surface area estimated by the t-plot analysis (Fig. 12f). Combined with the mesoporosity templated by PLA, highly porous materials exceeding 1000 m² g⁻¹ of BET surface area and 1 mL g⁻¹ of pore volume could be obtained. PLA removal in the basic condition produced polymers with mesopores only, supporting that hyper-cross-linking is responsible for micropore formation. While the PLA molar mass predominantly controlled mesopore size in the hierarchically porous polymer, the pore size was noticeably larger than the PLA domain size, probably because of swelling in the hyper-cross-linking step. In a follow-up study, Kim and Seo showed that hyper-cross-linking improved mesopore stability by additionally reinforcing the polystyrenic framework cross-linked by DVB [144]. The 3D continuous mesopores could be preserved even at low DVB loading after hyper-cross-linking without pore collapse (Fig. 12 g). The pore characteristics, including micro- and mesoporosities and mesopore size, could be adjusted by the VBzCl and DVB fractions in the polymerization mixture (Fig. 12h). The hierarchically porous polymer exhibited faster nitrogen adsorption kinetics compared to the microporous analog in the early stage (Fig. 12i). The adsorption rate of methyl orange from an aqueous solution was also enhanced than the microporous polymer with a similar BET surface area, particularly when the concentration was high (Fig. 12j).

The hyper-cross-linked hierarchically porous polymer also shows higher thermal stability than the mesoporous polymer with the P(S-co-DVB) framework. Kim et al. took this advantage to prepare a heterogeneous catalyst for the Suzuki-Miyaura cross-coupling reaction in the liquid phase (Fig. 13a) [145]. The pore structure persisted while loading the polyvinylpyrrolidone (PVP)-capped Pt nanoparticles and removing the ligand by plasma treatment (Fig. 13b). The hierarchically porous polymer-supported Pt catalyst outperformed micro-, mesoporous polymer analogs, and mesoporous oxide supports in reaction yield and recyclability (Fig. 13c). High catalytic activity toward challenging aryl chloride substrates was also noticed.

Lee and Seo reported that using trimethylsilylstyrene (TMSS) as a comonomer with VBzCl and DVB could boost microporosity further (Fig. 13d and e) [146]. The bulky trimethylsilyl group creates more void in the hyper-cross-linked domain by increasing the interchain distance and preferentially reacting with the carbocation in the Friedel-Crafts alkylation to leave the polymer network. They further explored the lower limit of attainable pore size in the PIMS systems (Fig. 13f) [109]. They found that the insufficient segregation strength of the system at low *N*, not framework stability when reinforced by hyper-cross-linking, limits pore downsizing as it hinders the formation of the microphase-separated morphology with high domain purity. In the search for high- χ comonomers to increase the segregation strength (also see Section 2.2), the authors chose VBP as the high- χ and hyper-cross-linking-active comonomer. At a constant DVB fraction (20 mol%), the molar composition of VBzCl vs. VBP was optimized to balance segregation strength and hyper-cross-linking density (Fig. 13 g). With the optimal 1:3 ratio, SAXS analysis with the Teubner-Strey fitting indicated that a weakly segregated precursor could be achieved even with 576 g mol⁻¹ PLA-CTA (Fig. 7h). At this *N*, the length scale of the PLA domain and the interchain free volume unified to produce a porous polymer containing nearly exclusively micropores centered at 1.1 nm instead of the bimodal pore size distribution in

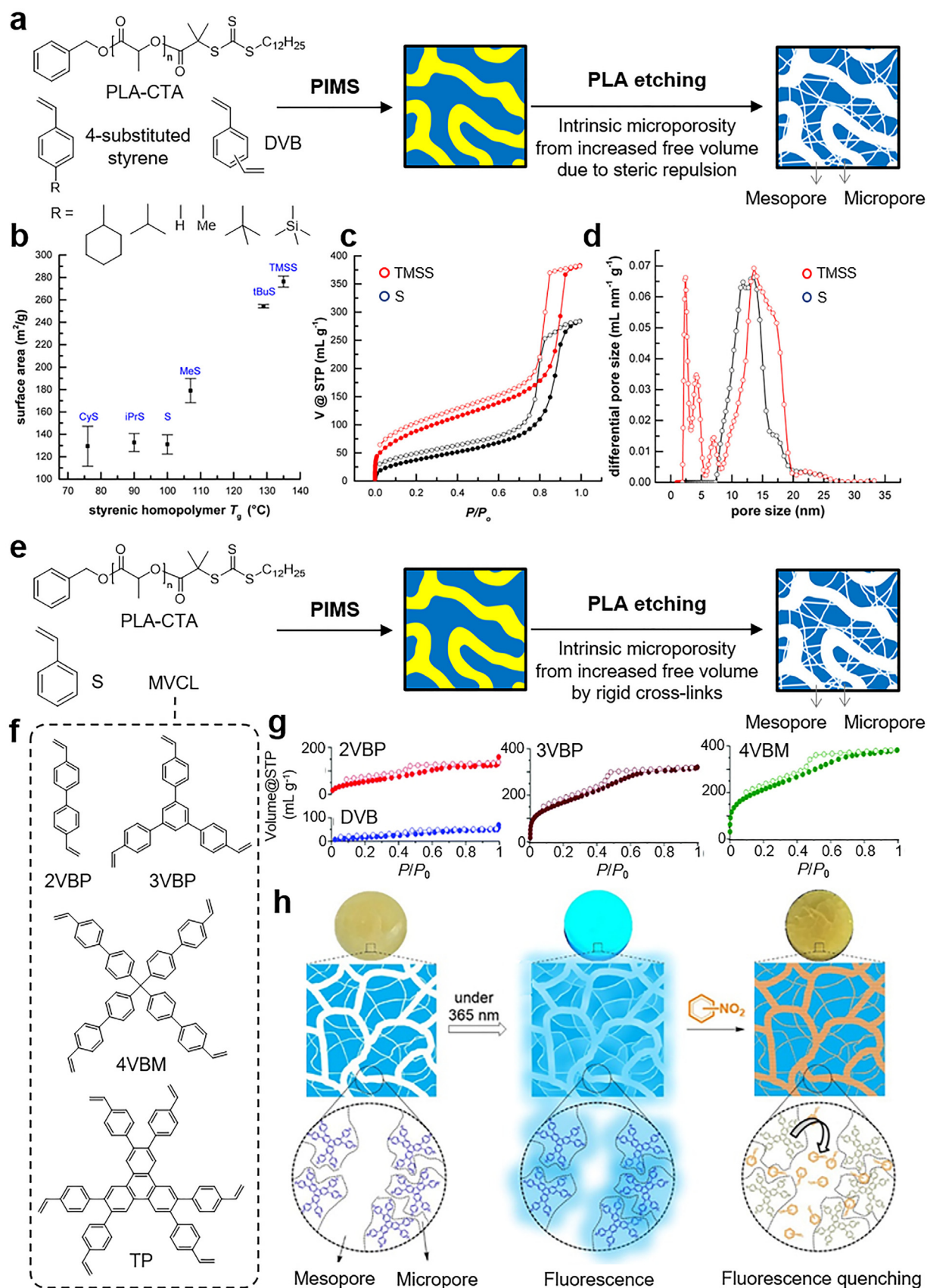


Fig. 11. (a-d) Generating intrinsic microporosity in the polystyrenic framework by introducing a sterically demanding pendant [137]. Copyright 2017. Adapted with permission from the American Chemical Society. (a) Synthetic route. (b) Correlation of S_{BET} of the porous polymers with T_g of the corresponding homopolymers. (c) Nitrogen sorption isotherms of the porous polymers synthesized with styrene (black) and TMSS (red). Filled symbol: adsorption branch; Open symbol: desorption branch. (d) QSDFT pore size distributions from the adsorption branches. (e-f) Generating intrinsic microporosity by using a conjugated multivinyl cross-linker (MVCL). (e) Synthetic route. (f) Chemical

the nitrogen sorption analysis. SAXS and TEM analyses supported the presence of micropores at this length scale, which was consistent with scaling of domain spacing and pore size as a function of PLA molar mass (Fig. 13i).

Finally, we note an interesting twist in the nanoporous polymer synthesis reported by Saba et al. The authors introduced PI-CTA as another macro-CTA incompatible with both PLA and polystyrenic chains [147]. The RAFT polymerization of DVB in the presence of PLA- and PI-CTAs yielded a tricontinuous morphology composed of PLA, PI, and PDVB domains that do not intersect. Basic PLA etching and cross-metathesis of PI with *trans*-4-octene removed the corresponding domains to produce bicontinuous nanoporous channels. This strategy could be useful for increasing mesoporosity and tailoring the surface of different porous channels with orthogonal surface chemistries.

3.2. Polymer electrolytes

Polymer electrolyte membranes are appealing alternatives to liquid electrolytes in lithium batteries and high-temperature fuel cells [148–156]. The solid-like electrolytes with higher mechanical properties are anticipated to avoid electrolyte leaking and, in the case of lithium batteries, suppress dendrite formation on the electrode surface which causes safety problems [150,151,157]. Leveraging high elastic modulus without sacrificing the ion conductivity necessary for cell operation should be key in designing polymer electrolyte membranes. PIMS offers a promising route to highly conductive and mechanically robust polymer electrolyte membranes composed of ion-conducting and densely cross-linked domains with long-range, isotropic bicontinuity. Compared to previous block polymer-based approaches, such as gelling ionic liquid with triblock copolymers and aligning lamellar-forming diblock copolymer materials swollen with ionic liquid, the PIMS approach provides much improved mechanical attributes while retaining high conductivity in a simple synthetic step.

Schulze et al. reported PIMS-derived polymer electrolyte membranes using the PEO-CTA/styrene/DVB system with BMITFSI and LiTFSI as ionic additives (Fig. 14) [158]. TEM and SEM (after PEO removal) imaging supported the PEO/BMITFSI and cross-linked polystyrenic bicontinuous domains were formed as a result of PIMS (Fig. 14b and c). The high conductivity of the materials was attributed to continuous conductive channels over macroscopic distances. Compared to a homogeneous electrolyte of the same PEO/ionic liquid composition, the estimated tortuosity factors were within the predicted bound of 1.5 – 3. Because mechanical and transport properties are decoupled in the microphase-separated morphology, the cross-linked polystyrenic domain responsible for modulus provided structural integrity even above the T_g of linear PS. Electrolyte materials with conductivity close to 10 mS/cm and elastic modulus of 0.1 GPa could be obtained (Fig. 14d and e). Increasing the ionic liquid content increased the charge carrier but lowered elastic properties, resulting in a trade-off between the ionic conductivity and the modulus according to the material composition. Replacing the ionic liquid with succinonitrile rendered the PEO/Li domain completely amorphous, resulting in even higher conductivity (~ 0.35 mS/cm) at 30 °C [159]. Other ionic liquids, such as protic 1-ethylimidazolium bis(trifluoromethylsulfonyl)imide (HEImTFSI), could also be incorporated into the PEO-CTA/styrene/DVB system and produce anhydrous proton-conducting polymer electrolyte membranes with high conductivity and high modulus [160]. Recently, Liu et al.

reported adding polyoxometalates ($H_3PW_{12}O_{40}$, $Li_7[V_{15}O_{36}(CO_3)]$) into the PEO-CTA/styrene/DVB system to fabricate anhydrous solid-state electrolytes [161]. The inorganic additives preferentially partitioned into the PEO domain and constructed effective ion-conducting nanochannels for proton and lithium.

Chopade et al. applied the PIMS-based polymer electrolyte membranes as ionic liquid-based reference electrodes [162]. Ionic liquid-based electrodes develop stable potential at the interfaces of ionic liquid and aqueous solutions of varying ionic strength and electrolyte composition, providing practical benefits over commercial KCl/porous-frit-based electrodes [163]. The authors incorporated hydrophobic 1-octyl-3-methylimidazolium bis(trifluoromethyl sulfonyl)imide ($C_8mimNtf_2$) and 1-dodecyl-3-methylimidazolium bis(trifluoromethyl sulfonyl)imide ($C_{12}mimNtf_2$) into the PMMA-CTA/styrene/DVB system. The electrode could be prepared by inserting the AgCl-coated wire into the polymerization mixture, which was firmly encapsulated within the product during polymerization. PIMS reliably produced the nanoscopic bicontinuous morphology comprising the ionic liquid-doped PMMA and cross-linked polystyrenic domains. Comparing the poly(vinylidene fluoride-co-hexafluoropropylene)-ionic liquid electrode previously reported in the literature [164], the PIMS-based reference electrode showed higher reference potential stability and reproducibility as well as sufficiently high ionic conductivity.

Bae et al. utilized the PEO-CTA/styrene/DVB system with BMITFSI as an ionic liquid additive to fabricate structural supercapacitors (Fig. 14f–j) [165]. A structural supercapacitor is a promising composite material for lightweight electric vehicles that provides high electricity storage capacity and simultaneously supports mechanical loads. One of the key challenges is to develop structural electrolytes that combine high ionic conductivity and mechanical rigidity and integrate them with active electrodes in conformal contact to minimize interfacial resistance and maximize mechanical reinforcement. The authors used carbon-coated Ni-Co core-shell nanowires on carbon fabric as active electrodes with high specific surface area to utilize electrical double-layer capacitance and fast faradaic electron charge transfer with redox reactions (pseudocapacitance). The supercapacitor was prepared by sandwiching the PIMS solution between the two electrodes and conducting polymerization. The nanowires immersed in the polymerization mixture were fully embedded in the final material, enabling load transfer through the interface to the carbon fiber. Stable charge-discharge cycling with capacitance retention supported that ion-conductive continuous pathways span the whole electrolyte thickness. Above 30 wt% loading of the ionic liquid, the composite underwent the brittle-ductile transition (Fig. 14g and h). The capacitor containing 30 wt% of the ionic liquid showed a tensile strength of ~ 100 MPa and power densities of 0.5 to 1 kW kg⁻¹. In the *in situ* mechano-electrochemical tests, the capacitor retained its capacitance during tensile and bending deformation, supporting that the structural electrolyte produced by PIMS can provide sufficient structural durability and integrity to the composite while maintaining the ability to store electricity under external loads (Fig. 14i and j).

3.3. Postpolymerization-modified materials

Postpolymerization modification refers to a reaction involving a presynthesized polymer as the substrate [166–168]. The PLA etching and hyper-cross-linking steps in the nanoporous polymer

structure of MVCLs reported in the literature. (g) Nitrogen sorption isotherms of the porous polymers synthesized with MVCLs. The DVB data is included as a reference. Filled symbol: adsorption branch; Open symbol: desorption branch [138]. Copyright 2018. Adapted with permission from the Royal Society of Chemistry. (h) Fluorescent porous monolith synthesized with TP and its fluorescence quenching upon exposure to nitroaromatics in organic solutions [139]. Copyright 2023. Adapted with permission from Elsevier Science Ltd. (For interpretation of the references to colour in this figure legend, the reader is referred to the web version of this article.)

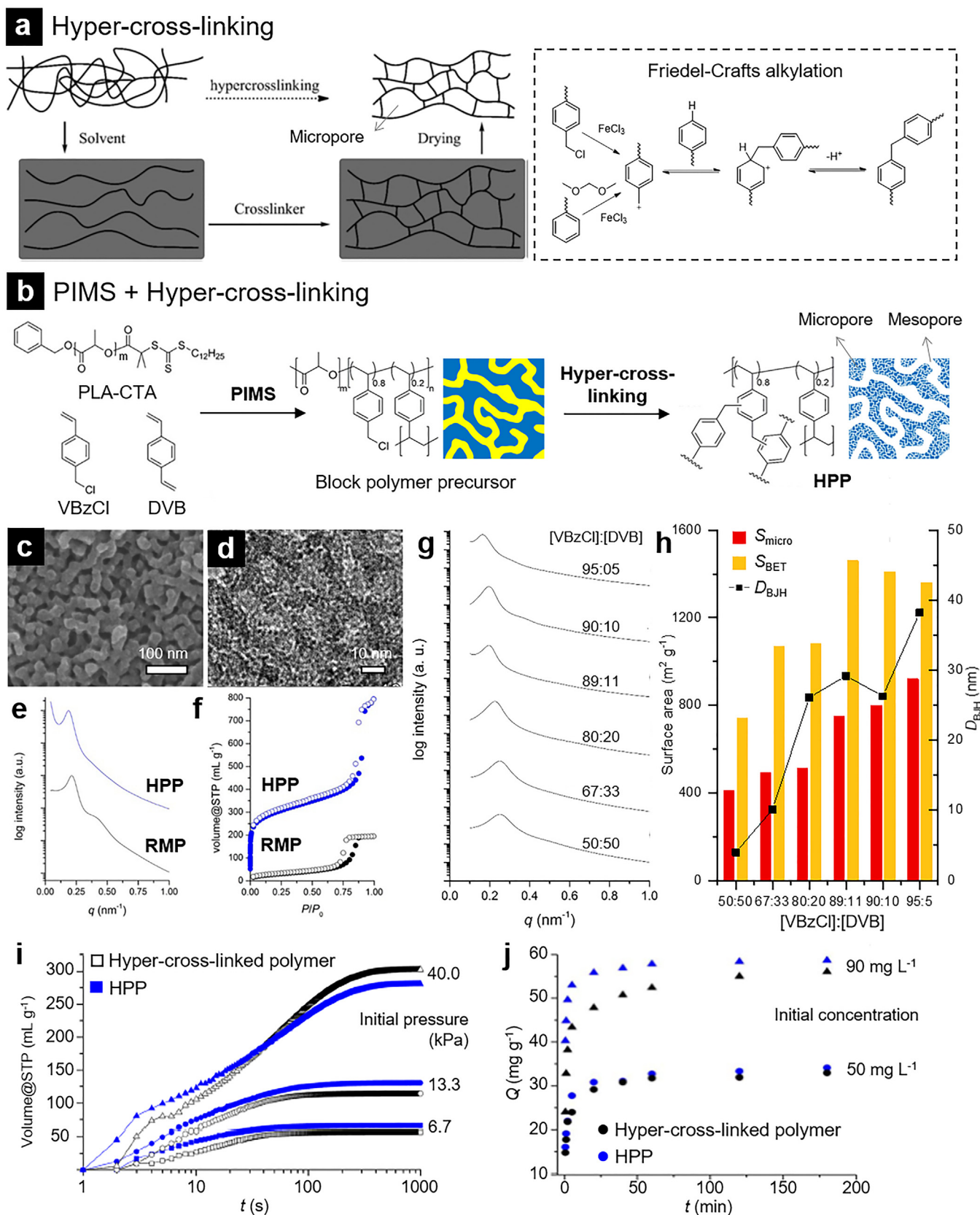


Fig. 12. Hierarchically porous polymers containing micro- and mesopores by the combination of hyper-cross-linking with PIMS. (a) Schematic depiction of hyper-cross-linking for the microporous polymer synthesis via Friedel-Crafts alkylation. [142], Copyright 2017. Reproduced with permission from the Royal Society of Chemistry. (b) Synthetic route to a hierarchically porous polymer (HPP) by PIMS of PLA-CTA/VBzCl/DVB followed by hyper-cross-linking [143], Copyright 2015. Adapted with permission from the American Chemical Society. (c) SEM image of HPP obtained with 41 kg mol⁻¹ PLA-CTA after Pt coating. (d) TEM image of HPP obtained with 11 kg mol⁻¹ PLA-CTA [109],

synthesis discussed above can be examples of postpolymerization modification of the block polymer precursors produced by PIMS. Here we discuss other chemical transformations, such as installing and converting functional groups, to see how postpolymerization modification enables to incorporate functional groups that cannot be directly included during the precursor synthesis and thus diversifies the scope of PIMS-based functional materials.

Postsulfonation. Jeon et al. reported postsulfonation of nanoporous P(S-co-DVB), which was derived by PIMS of PLA-CTA/styrene/DVB (Fig. 15a) [169,170]. The polymerization mixture was loaded in the middle of a sandwich assembly of glass plates to produce large-area samples. The postsulfonation reaction with concentrated sulfuric acid installed sulfonic acid groups on the polystyrenic pore surface via the electrophilic aromatic substitution mechanism. While nitrogen sorption analysis was impossible after sulfonation, SEM and SAXS data showed the highly cross-linked framework retained the 3D continuous pore structure during the reaction. The sulfonic acid content could be controlled by reaction time to reach the ion exchange capacity (IEC) up to 2 meq g⁻¹.

Proton conductivity increased with IEC regardless of the pore size, suggesting that protons traverse the pore mainly via a hopping mechanism [171]. In contrast, the ion permeability of alkali chlorides in aqueous solutions decreased with the increasing sulfonic acid content, presumably because of electrostatic drag from the pore wall. Cations with smaller hydrodynamic radii diffused faster through larger pores, indicating that the transport of ions driven by chemical potential difference occurs via a vehicular mechanism [171–173]. When the pore size was reduced below 4 nm, a theoretical threshold for VO²⁺ crossover [172], VO²⁺ permeability through the sulfonated pores dropped less than 4 × 10⁻⁸ cm² min⁻¹, which was 100 times lower than that of Nafion 212 (Fig. 15b). The permeability data suggests that the PIMS-based membranes with well-defined pore size and tailored surface charge characteristics can enhance permselectivity more than conventional proton exchange membranes such as Nafion.

To take advantage of decoupled proton conductivity and VO²⁺ permeability for the vanadium redox flow battery application, the authors developed a reinforced version of the free-standing membrane by impregnating a polyethylene fiber mat in the polymerization mixture. A much thinner yet mechanically superior membrane could be prepared with improved surface roughness. The effect of the polyethylene fiber on the PIMS process and the resulting pore structure seems minimal. A vanadium redox flow battery cell was fabricated with the optimized membrane compared with Nafion of a similar thickness. Higher voltage and coulombic efficiencies and excellent energy efficiency retention were attributed to facilitated proton conduction along the sulfonated pore surface and effectively suppressed VO²⁺ crossover by adjusting the pore size (Fig. 15b). This is the first example of block polymer-based nanoporous membranes for battery applications, suggesting the great potential of the PIMS methodology in this field.

Functional group conversion. Goldfeld et al. reported the functional group conversion approach to preparing nanostructured polymer electrolyte thermosets that carry charges bound to the polymer chain in the active domain (Fig. 15c) [174]. The authors used poly(*n*-octyl styrene sulfonic ester) and PVBzCl as macro-CTAs containing pre-functional polymer blocks. With styrene and DVB,

PIMS produced the bicontinuously nanostructured precursors. Exposure to trimethylamine solution converted the pre-ionic polymers to negatively charged poly(styrene sulfonate) and positively charged poly(vinylbenzyl trimethylammonium), respectively, while retaining the morphology [175]. ATR-IR analysis confirmed quantitative conversion. The low extent of swelling in water due to the cross-linked polystyrenic framework indicated the dimensional stability of the electrolyte materials. Adsorption of complementarily charged dye molecules corroborated successful functionalization through the percolating pre-ionic domains derived by PIMS.

Incorporating the pre-functional polymer block between the sacrificial and framework blocks allows the functionalized polymer chains to decorate the pore surface [176]. Peterson et al. applied this “middle block” approach to PIMS to synthesize nanoporous beads with cation- and anionically functionalized pore walls (Fig. 15d) [177]. They introduced polycaprolactone (PCL) as a sacrificial block that can be degraded under the alkaline condition, and extended the chain with PVBzCl or poly(*tert*-butyl acrylate) as pre-ionic polymer blocks via RAFT polymerization. The resulting diblock copolymers were used as macro-CTAs combined with styrene and DVB in suspension polymerization to produce precursor beads following the PIMS mechanism. Basic etching followed by acidic deprotection of the *tert*-butyl group resulted in poly(acrylic acid) chains dangling on the pore surface. Strong incompatibility between poly(*tert*-butyl acrylate) and PS seems to assist the formation of the well-defined pore structure [178]. An aqueous triethylamine solution concurrently etched PCL and modified the PVBzCl block while using anhydrous functionalized the PVBzCl block only. While the SAXS data indicated the retention of the morphology, negligible porosity of the cationic beads was attributed to the extended conformation of the charge chains filling up the porous channel [177]. Dye adsorption kinetic experiments also supported the presence of well-defined ion channels enabling fast adsorption of molecules with complementary charges, outperforming commercial Amberlite HPR4811 in the case of the cationic beads. This approach will be useful for tailoring the pore surface with control of functional group density.

Ceramization. Hwang et al. reported the conversion of the pre-ceramic polymer framework into silicon carbonitride (Fig. 15e) [179]. The authors used a methacrylate-modified vinylsilazane as a monomer in the PIMS recipe with PEO-CTA and DVB [180]. The resulting organic-inorganic hybrid was heated to 1000 °C to decompose PEO and convert the silazane-rich phase into SiC_xN_y ceramic. DVB was vital to maintain the structural integrity of the resulting mesoporous ceramics. Temperature-dependent *in situ* SAXS, FTIR, TGA analyses, and nitrogen sorption analysis of the post-mortem samples, suggested that mesopores and micropores develop above 650 °C. While the decomposition of PEO generates mesoporous voids, the Si-rich framework undergoes densification with the pyrolysis of organic residues, resulting in micropore formation and reduction in both nanoscopic and macroscopic dimensions. Because of the isotropic nature of the disordered bicontinuous morphology captured by PIMS, the ceramic retained its original geometry upon isotropic shrinkage, as demonstrated with molded samples. While the PEO molar mass primarily controlled the mesopore size, the sample synthesized with 10 kg mol⁻¹ PEO-CTA lost porosity above 750 °C. Mesopores centered at 9.1 nm survived at 1000 °C when 20 kg mol⁻¹ PEO-CTA was used, while microporos-

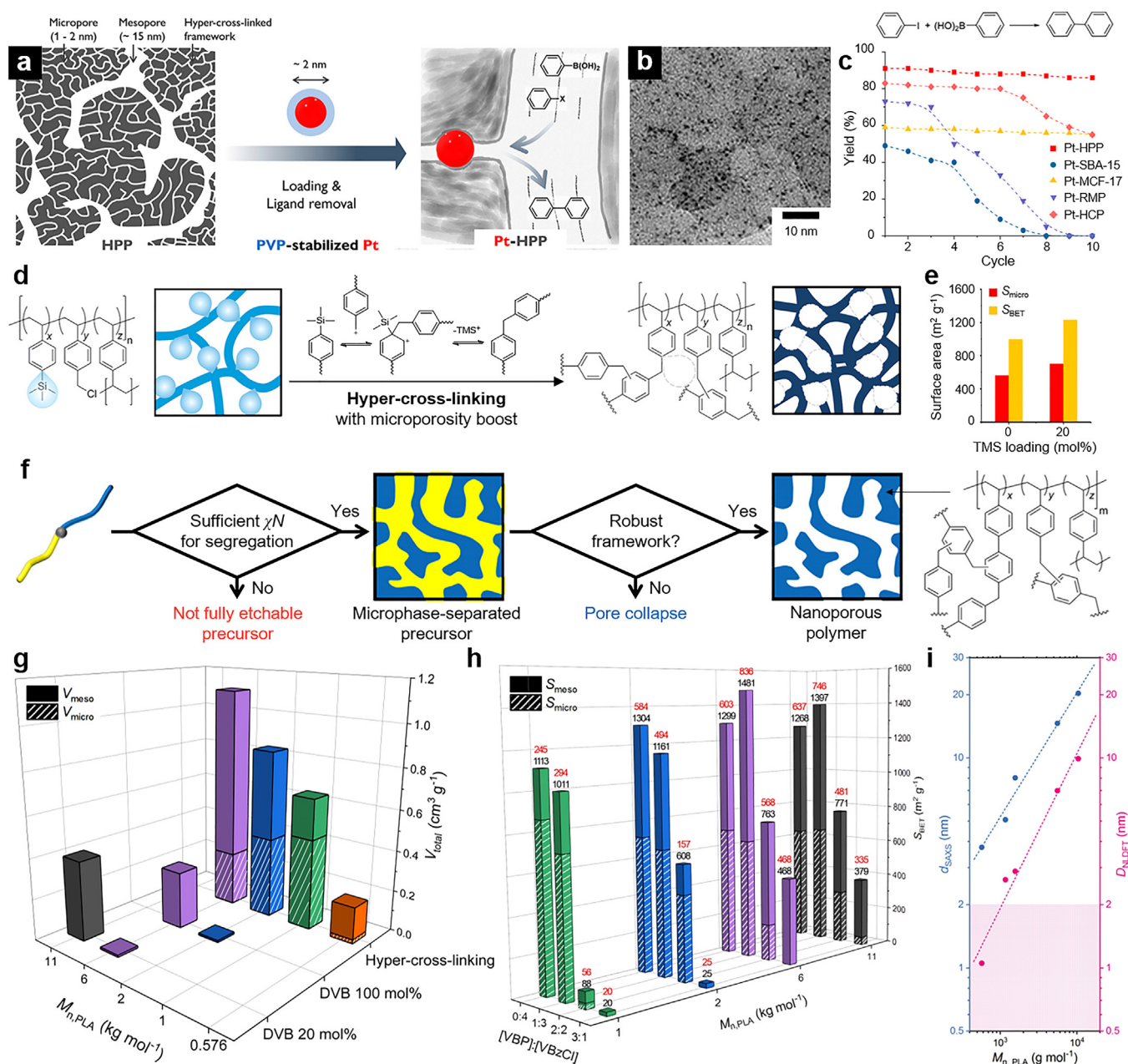


Fig. 13. (a–c) Pt nanoparticle-loaded polymer support as a heterogeneous catalyst for the Suzuki-Miyaura cross-coupling reaction [145]. Copyright 2021. Adapted with permission from the American Chemical Society. (a) Schematic depiction for the catalyst preparation, including PVP-stabilizing Pt nanoparticle loading into HPP followed by plasma treatment. (b) TEM image of the prepared Pt-HPP catalyst. (c) Recyclability of Pt-HPP compared to microporous (HCP) and mesoporous (RMP) polymers and mesoporous silica (SBA-15 and MCF-17) as supports. (d–e) Enhancing microporosity by introducing the trimethylsilyl group as the preferred leaving group in the Friedel-Crafts alkylation. (d) Schematic illustration of the mechanism [146]. Copyright 2018. Adapted with permission from the American Chemical Society. (e) Enhancement in surface areas of HPP produced from the PLA-CTA/TMSS&VBzCl/DVB system. The bar graph was plotted based on the data shown in [146]. The data without TMSS is shown as a reference. (f–i) Lowering the pore size limit by incorporating VBP [109]. Copyright 2021. Adapted with permission from the American Chemical Society. (f) Higher- χ , hyper-cross-linkable comonomer strategy to induce microphase separation at lower N and stabilize the pore structure by hyper-cross-linking. (g) Pore volume of the porous polymers without VBP as a function of PLA molar mass ($M_{n,PLA}$) and cross-linking density. In each column, solid (top) and patterned (bottom) fractions represent the contribution of meso- (V_{meso}) and micropores (V_{micro}), respectively. (h) S_{BET} of the VBP-containing porous polymers as a function of $M_{n,PLA}$ and [VBP]:[VBzCl] ratio. (i) Double logarithmic plot of d_{SAXS} and D_{NLDFT} as a function of $M_{n,PLA}$. The d_{SAXS} data is identical to that shown in Fig. 6h. (f–i).

ity diminished due to highly dense ceramization. TEM imaging corroborated the mesoporous nature of the resulting ceramic material, and also revealed the presence of an amorphous, graphite-like carbon phase derived from DVB in the SiCN ceramic phase.

Compared to previous strategies for mesoporous ceramics synthesis using silicon-containing block polymer precursors that typically require complicated solvent/thermal annealing steps to achieve uniformity and long-range continuity of the domains,

the organic-inorganic hybrid PIMS methodology utilizing preceramic monomers offers a convenient, moldable, and scalable synthesis of preceramic materials with control of domain size. The PIMS-derived nanoporous ceramics are expected to find applications in catalysis, separation, optical materials, and energy devices [181,182].

Reversible photoreaction. A unique example of postpolymerization modification was reported by Peterson and Hillmyer where

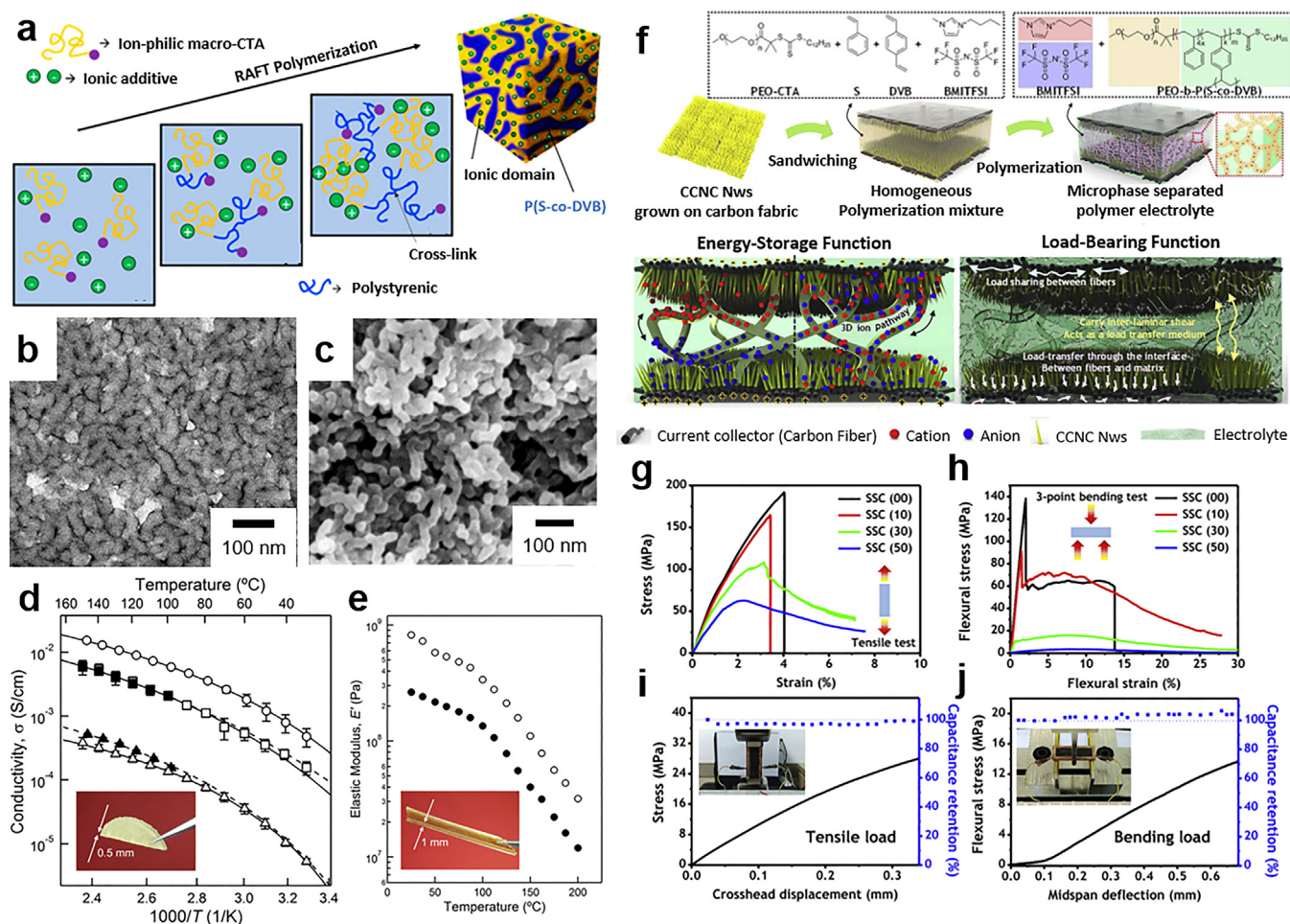


Fig. 14. Polymer electrolyte fabrication via PIMS. (a-e) Polymer electrolyte membrane synthesis from the PEO-CTA/styrene/DVB formulation with ionic additives [158], Copyright 2014. Adapted with permission from the American Chemical Society. (a) Schematic illustration for the structural evolution with the preferential partition of the ionic additives [162], Copyright 2017. Adapted with permission from the American Chemical Society. (b) TEM image of the membrane obtained with 28 kg mol⁻¹ PEO-CTA and 21 vol% BMITFSI. The specimen was stained with RuO₄ prior to imaging. (c) SEM image of the same sample after Hl(aq) treatment and Pt coating. (d) Ionic conductivity as a function of temperature. PEO-CTA of 5 kg mol⁻¹ was used for the synthesis. A photo of a typical sample is shown as an inset. Overall salt concentrations were 5 (Δ), 7 (▲), 21 (□) and 40 vol% (○). (e) Temperature-dependent linear elastic response. PEO-CTA of 28 kg mol⁻¹ was used with 21 vol% BMITFSI (●) and no ionic liquid (○). The inset is a photo of a typical tensile bar. (f-j) Structural supercapacitor fabrication [165], Copyright 2018. Adapted with permission from Elsevier Science Ltd. (f) Schematic depiction for the fabrication process including sandwiching of the PIMS solution between carbon-coated Ni-Co core-shell nanowires (CCNC Nws in the figure) on carbon fabric as active electrodes and subsequent polymerization. The working mechanism of the structural supercapacitor for energy-storage and load-bearing dual functions is also illustrated. (g-h) Tensile (g) and flexural (h) stress-strain curves. The weight fraction of BMITFSI is indicated within the parentheses. (i-j) Specific capacitance retention under tensile (i) and bending (j) loads *in situ*. 30 wt% of BMITFSI was included.

the authors utilized reversible spiropyran-merocyanine conversion by light (Fig. 15f) [183]. Spiropyran is a well-known photochromic dye that undergoes a C–O bond cleavage upon UV irradiation to form deeply colored merocyanine [184,185]. Without UV, the ring-closing reaction restores the colorless spiropyran. While the dye has been embedded in optically transparent materials such as PMMA to make responsive lenses, improving the photochromic transition rate has been challenging because the glassy matrix with little free volume hinders the reaction [186,187].

The authors adopted the PIMS approach to creating a bicontinuously nanostructured thermoset comprising rubbery and glassy domains, where the spiropyran motif is attached to some rubbery chain ends (Fig. 15f). Poly(γ -methyl- ϵ -caprolactone) (P4MCL) with T_g of -60°C was chosen as the rubbery polymer [188]. P4MCL-CTA containing 1.6% of dye-functionalized P4MCL was combined with MMA and ethylene glycol dimethacrylate as a cross-linker in the PIMS recipe. Polymerization produced a transparent yet yellow monolith because of the trithiocarbonate group. The monolith turned deep violet upon UV exposure and returned to its original color over time. The decoloration rate of the PIMS product was

five times faster than the dye-doped PMMA, supporting that the P4MCL-appended spiropyran is preferentially located in the rubbery domain containing large free volume. A PIMS product prepared by adding free spiropyran to the polymerization, where the dye should be statistically distributed across the whole specimen, showed slower decoloration kinetics and corroborated the importance of covalent engineering for the dye-polymer conjugate. Faster decoloration was achieved by lowering the P4MCL molar mass, decreasing the cross-linking density, and increasing the P4MCL mass fraction.

4. PIMS-compatible polymerization techniques

4.1. Neat thermal polymerization

RAFT copolymerization of vinyl monomers has been used as a main workhorse in the PIMS process to secure the covalent junction between the macro-CTA and the growing polymer block. Trithiocarbonates have been the choice of CTA that offer balanced activity and stability for more activated monomers, includ-

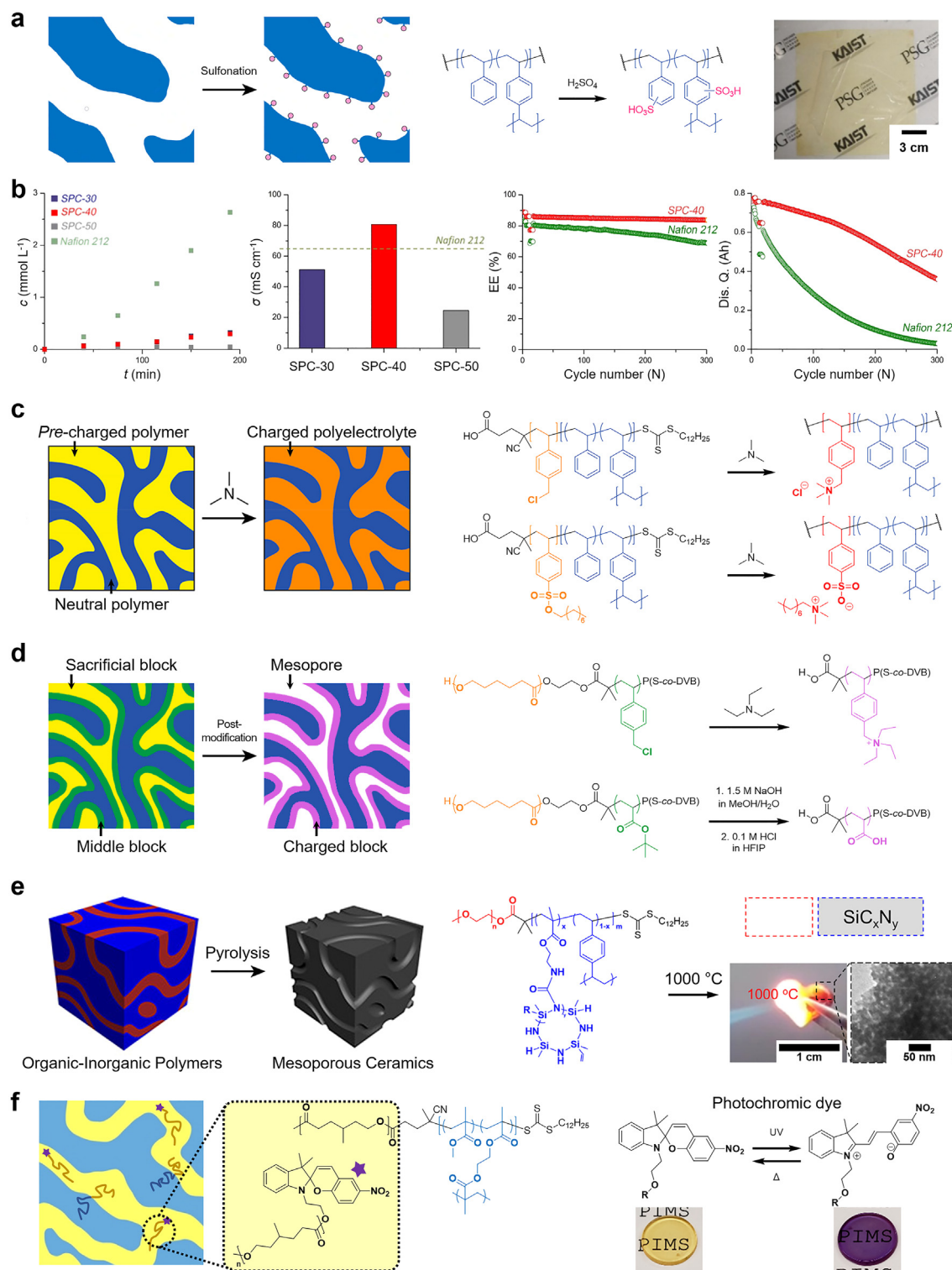


Fig. 15. Postpolymerization modification of PIMS materials. (a) Schematic depiction (left) and reaction scheme (middle) for postsulfonation on the mesoporous surface. A photo of the sulfonated porous membrane synthesized with the polyethylene fiber mat is also shown (right). (b) VO^{2+} permeability and proton conductivity of sulfonated porous membranes (SPCs; the number indicates the weight fraction of PLA-CTA in the polymerization mixture), and their energy efficiency and discharge capacitance retention compared to Nafion 212 during the vanadium redox flow battery operation. (a-b) [170], Copyright 2020. Reproduced with permission from the American Chemical Society. (c-d) Schematic depictions (left) and reaction schemes (right) for converting the pre-charged neutral polymers into charged polyelectrolytes. Nonporous (c) and porous systems involving the sacrificial block removal (d) are shown [174,177]. [174], Copyright 2021. Adapted with permission from the American Chemical Society. [177], Copyright 2022. Adapted with permission from the American Chemical Society. (e) Schematic illustration for converting the preceramic precursor into mesoporous ceramics by pyrolysis (left). The chemical structure of the preceramic precursor is given (middle), along with a photo of a molded mesoporous ceramic under flame and its TEM image (right) [179], Copyright 2020. Reproduced with permission from the American Chemical Society. (f) PIMS thermoset containing spiropyran. The chain conformation is sketched in the cartoon with the chemical structure (left). The photochromic reaction and the corresponding visual change are shown (right) [183], Copyright 2019. Adapted with permission from the American Chemical Society.

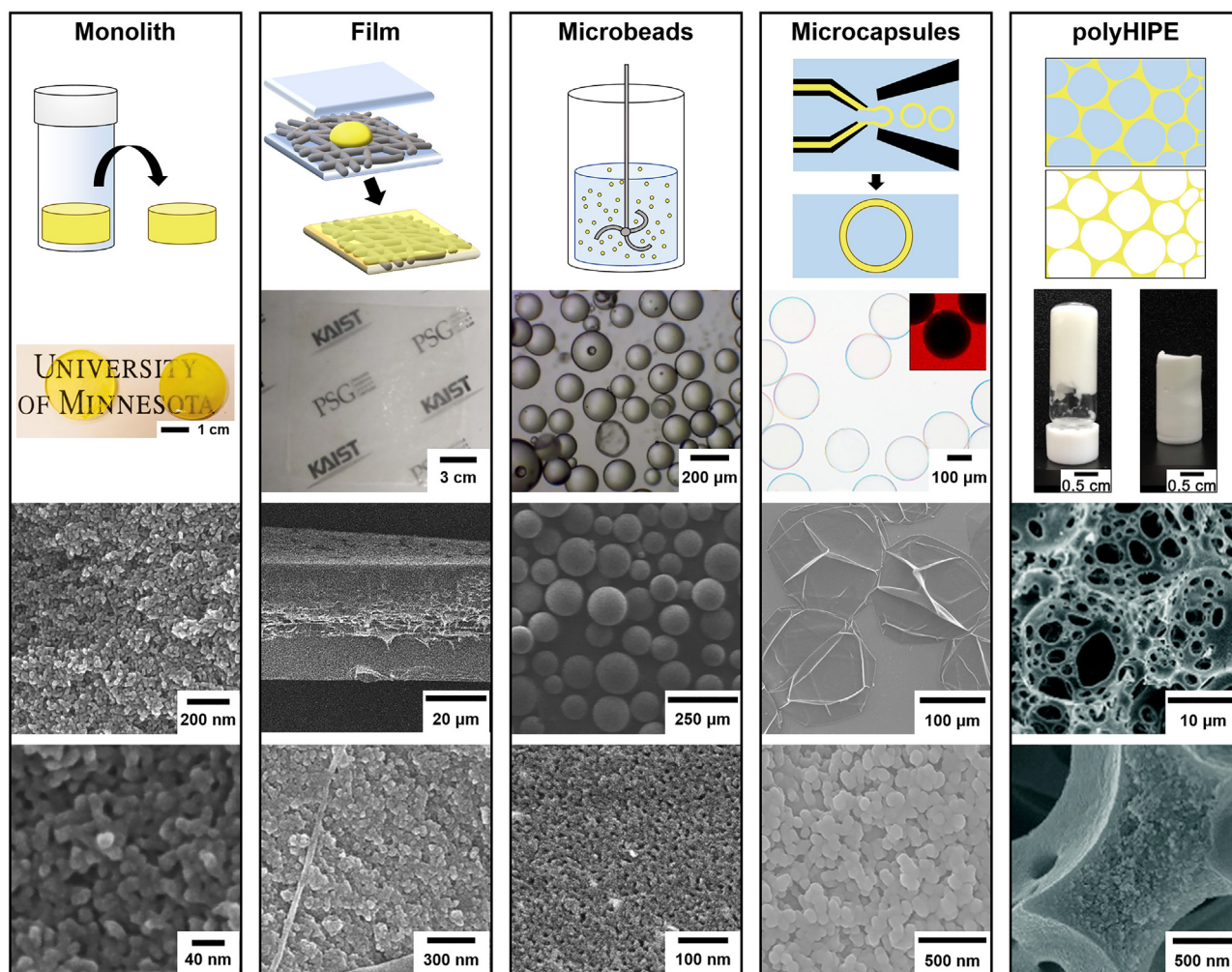


Fig. 16. Shapability of PIMS. Monolith [22], film [170], microbeads [177], microcapsules [198], and polyHIPE [207] forms are exemplified along with the cartoons for the fabrication processes, product photos, and SEM images after PLA etching (except for the photo of the film, which was taken at the precursor state). [22], Copyright 2012. Adapted with permission from the American Association for the Advancement of Science. [170], Copyright 2020. Adapted with permission from the American Chemical Society. [177], Copyright 2022. Adapted with permission from the American Chemical Society. [198], Copyright 2018. Adapted with permission from the American Chemical Society. [207], Copyright 2018. Adapted with permission from the Royal Society of Chemistry.

ing styrenics, methacrylates, and acrylates [189]. Carboxylic acid- and hydroxyl-functionalized CTAs are useful for conjugating with hydroxy-terminated homopolymers and initiating ROTEP of cyclic ester monomers to produce macro-CTAs [190,191].

Azobisisobutyronitrile (AIBN) has been widely used as a thermal radical initiator for the PIMS process in the temperature range of 50–90 °C. Autoinitiation above 120 °C without external radical initiators has also been utilized for styrenic monomers. Schulze et al. investigated the effect of polymerization temperatures of 60 and 120 °C on nanoporous polymers derived from the PLA-CTA/styrene/DVB formulation with AIBN [107]. While χ should decrease with the increasing temperature, negligible differences in the q^* position in the SAXS patterns suggested the reaction kinetics dominates the morphology at the onset of arrest. The polymerization at 120 °C produced larger BET surface areas in the resulting nanoporous polymers, probably because of the more rigid framework formation with elevated cross-linking. In some cases, additional heating to 200 °C was applied in the final polymerization stage to consume the remaining double bonds further and rigidify the structure [123].

In principle, the RAFT polymerization as controlled radical polymerization should be performed in an inert atmosphere to avoid chain transfer to oxygen. Nonetheless, adding more AIBN to the

polymerization mixture facilitates the PIMS process in air. The neat polymerization mixture without solvent can be poured into a closed container with the desired shape and heated under an ambient atmosphere to solidify the whole liquid into a molded block polymer monolith. Fig. 16 comprises different forms forged by the PIMS processes and their internal structures observed by SEM. Hwang et al. demonstrated moldability for PIMS using commercially available silicone molds [179]. Nearly quantitative conversion in the absence of solvent was crucial for replicating the mold features with minimal change in dimensions. RAFT copolymerization with a cross-linker provided a dense, homogeneous cross-linking across the whole sample to avoid crack formation. Film forms were also produced by using a glass plate assembly. Jeon et al. showed free-standing films as large as 10 cm × 10 cm could be readily prepared with a polyethylene fiber mat impregnated in the polymerization mixture.

4.2. Suspension and emulsion polymerizations

Being virtually identical to the free radical polymerization system except for the CTA, RAFT polymerization is compatible with various polymerization methods, including bulk, solution, suspension, and emulsion polymerizations [189]. The versatility of RAFT

polymerization has been exploited in the PIMS process to explore the soft templating strategies offered by suspension and emulsion polymerizations. The key is to disperse the PIMS polymerization mixture into an immiscible dispersion medium (or *vice versa* if the polymerization mixture forms a continuous phase) by proper interfacial engineering. Block polymer microspheres, microcapsules, and macroporous monoliths have been produced, retaining the nanoscopic bicontinuous morphology, and converted into nanoporous materials by subsequent removal of the sacrificial block (Fig. 16). Combining morphological control at the micrometer length scale with nanostructuring via PIMS offers a route to robust hierarchically structured materials with structural integrity and orthogonal length scale control.

Peterson et al. applied suspension polymerization to PIMS of the PCL/styrene/DVB formulation with poly(vinyl alcohol) (PVA) as a stabilizer in water. Suspension polymerization is suitable for the scalable production of polymer microspheres [177]. Block polymer beads were successfully produced by suspension polymerization. Their size and distribution of the beads could be adjusted by the stir rate, consistent with Hinze analysis [192]. Confocal Raman microscopy indicated the uniform distribution of PCL and polystyrenic domains within the micrometer resolution, supporting the presence of the nanoscopic bicontinuous morphology. PCL removal in the alkaline condition produced mesoporous polymer beads. Pore characteristics evaluated by SAXS, nitrogen sorption analysis, and SEM indicated the pore structure is virtually identical to that derived from PIMS of the neat polymerization mixture. Functionalizing the pore wall using the aforementioned middle block approach was also possible. Importantly, the pores were exposed on the bead surface, indicating both domains are in contact with water at the interface. The mesoporous beads could be prepared on a 20-g scale. They are anticipated to be useful for heterogeneous catalysis and separations [193–197].

PIMS within emulsions has been reported earlier by Oh et al. [198]. The authors used a microfluidic technique to prepare water/oil/water double emulsion drops with uniform sizes [199–201]. The PIMS solution comprising PLA-CTA/styrene/DVB was used as the thin middle oil phase, stabilized by PVA. Thermal polymerization using AIBN as the initiator produced transparent block polymer microcapsules suspended in water. The 3D continuous, densely cross-linked polystyrenic framework created by PIMS maintained the integrity of the capsules without rupturing upon drying. PLA etching derived mesopores percolating the entire shell thickness ($\sim 1 \mu\text{m}$ thick) while retaining the microcapsule structure. Permeability study with dye-tagged dextrans indicated size-selective permeability based on the relative pore size to permeate. The cutoff threshold for permeation could be controlled by the PLA molar mass in the hydrodynamic diameter range of 5–30 nm, which was not attainable by previous macrophase separation-based methods [202,203]. The permselective microcapsules are expected to be applicable as microreactors and sensing platforms by combining high encapsulation efficiency with regulated transport across the shell [204–206].

Park et al. prepared high internal phase emulsions (HIPEs) by dispersing aqueous droplets in a thin, continuous oil phase of the PLA-CTA/styrene/DVB solution under vigorous mixing [207]. Span 80 was added to the oil phase as a surfactant to stabilize the emulsion. The final emulsion could contain 90 vol% of the aqueous “internal” phase (containing 20 mM CaCl_2), occupying more than 74% of the whole volume, dispersed in 10 vol% of the external oil phase [208]. A sufficient amount of Span 80, far higher than the critical micellar concentration, was vital to cover the continuously generated interface promptly and form micelles to stabilize the aqueous droplets further. Potassium persulfate added to the aqueous phase initiated the RAFT polymerization at 70 °C and converted the while soft solid into “polyHIPE,” a highly porous poly-

mer monolith possessing interconnected macropores templated by the aqueous droplets [209–212]. PLA removal afforded continuous mesopores formed within the macroporous framework, supporting that the PIMS process successfully occurred within the confined oil phase. Orthogonal control of macro- and mesopore sizes was demonstrated. The meso- and macroporous monolith was further subjected to hyper-cross-linking by reacting with FeCl_3 and formaldehyde dimethyl acetal as an external cross-linker to create micropores within the mesoporous P(S-co-DVB) framework [140]. The enhanced dye adsorption kinetics with high adsorption capacity indicated that the micro-, meso-, and macropores are mutually interconnected in this hierarchically porous material to provide a short-cut path to the microporous surface.

4.3. Photopolymerization

RAFT photopolymerization is a promising methodology enabling spatiotemporal control over polymerization [212]. While large-area thermal polymerization is challenging in the PIMS process because of the potential loss of volatile monomers during the relatively long polymerization time at elevated temperatures, rapid conversion can be achieved with photopolymerization even under ambient conditions, especially when acrylates and methacrylates are used as the monomers. Recent applications of photo-PIMS in 3D printing further allow to build nanostructured block polymer materials with complex shapes.

Oh and Seo reported the first application of the photoinitiated RAFT polymerization in PIMS by developing an acrylate-based formulation of PLA-CTA/isobornyl acrylate (IBA)/ethylene glycol diacrylate (EGDA) (Fig. 17a) [191]. IBA was chosen because of its high T_g close to PS (112 °C). 2,2-Dimethoxy-2-phenylacetophenone (DMPA) was added as the photoradical initiator to generate radicals under long UV while avoiding the CTA decomposition [213]. IBA was successfully photopolymerized in the presence of PLA-CTA to produce PLA-*b*-PIBA. After confirming microphase separation of PLA-*b*-PIBA and selective degradation of PLA in the alkaline condition, photo-PIMS was performed to yield a monolithic product after 30 min of UV exposure at room temperature with 1,4-dioxane as a solvent (<40 wt% of the whole polymerization mixture). The bicontinuous morphology formation, following the PIMS mechanism, was confirmed by the SEM analysis (Fig. 17b). SAXS data was also consistent with the PIMS mechanism. A free-standing film with dimensions of 20 cm \times 20 cm \times 120 μm could be readily produced using the glass sandwich assembly in a UV tape curing system (Fig. 17c). The alkaline treatment removed both PLA and 1,4-dioxane to render the film mesoporous throughout the film thickness with lateral shrinkage due to solvent removal.

Bobrin et al. explored photo-PIMS of the formulation comprising poly(*n*-butyl acrylate)(PnBA)-CTA/acrylic acid(AA)/poly(ethylene glycol) diacrylate (PEGDA) in 3D printing (Fig. 18a) [214,215]. A commercial digital light processing printer was employed with diphenyl(2,4,6-trimethylbenzoyl) phosphine oxide as a photoradical initiator. 3D printed materials with the bicontinuous morphology were successfully produced via the PIMS process. Compared to the statistical copolymer of P(nBA-co-AA-co-PEGDA), the PIMS materials showed enhanced toughness and elongation at break owing to the interpenetrating soft PnBA and hard P(AA-co-PEGDA) microdomains (Fig. 18c). Systematic variation of the weight fraction and the molar mass of PnBA-CTA indicated the well-defined, percolating PnBA domain is critical for improved mechanical responses. However, increasing the PnBA domain size too much seems detrimental as the reduced interfacial area between the PnBA/P(AA-co-PEGDA) domains lowers the stress dissipation efficiency (Fig. 18c). The domain size was also tunable by adding PnBA homopolymer following the mechanism discussed in Section 2.2. The PnBA homopolymer seems to exceed

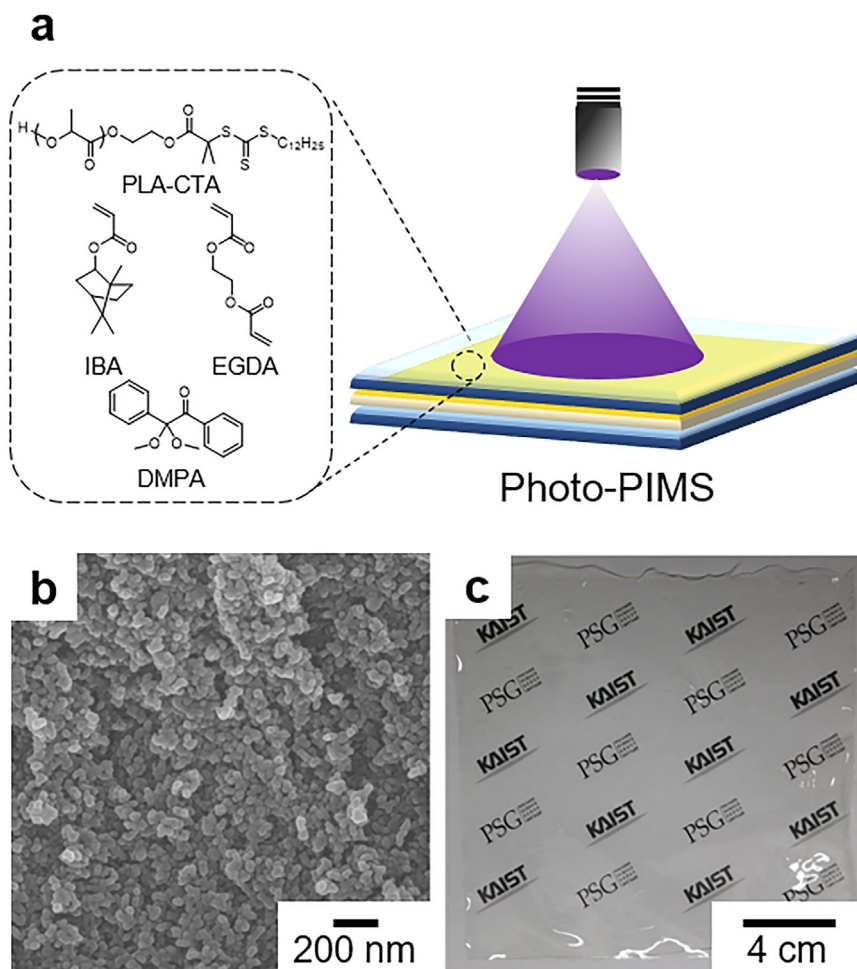


Fig. 17. Photo-PIMS for film fabrication [191], Copyright 2015. Adapted with permission from the American Chemical Society. (a) Schematic illustration of the photopolymerization setup. The PLA-CTA/IBA/EGDA formulation is given with DMPA as a photoradical initiator. (b) SEM image after PLA etching of the film. (c) A photo of the film produced by the tape curing system (20 cm × 20 cm × 120 μm).

the solubility limit above 50 wt% loading and start to induce macrophase separation, which makes the material more brittle (Fig. 18d and e).

Interestingly, Shi et al. demonstrated that a phase-inverted morphology of discrete P(AA-co-PEGDA) domains dispersed in the PnBA matrix was found when multi-arm PnBA-CTAs were used, suggesting a role of the macro-CTA architecture in the morphological evolution (Fig. 18f) [216]. The elongation at break and tensile strength of the PIMS materials were primarily related to the PnBA-CTA content. No significant difference was observed by the macro-CTA architecture variation. Higher swellability both in water and organic solvents and faster dye release kinetics were also attributed to the well-segregated hydrophobic PnBA and hydrophilic P(AA-co-PEGDA) domains (Fig. 18g). The swelling-induced deformation behavior demonstrates attractive opportunities for soft materials produced by PIMS.

Lee et al. further applied the 3D printing technique to the PEO-CTA/IBA/trimethylolpropane triacrylate(TMPTA) formulation with BMITFSI as an additive to fabricate solid polymer electrolytes [217]. The resulting materials shared structural characteristics with the polymer electrolyte membranes produced from the PEO-CTA/styrene/DVB mixture with BMITFSI discussed earlier [158] and also showed a similar structure-property relationship (Fig. 18h). Replacing PEO-CTA with poly(oligoethylene glycol methyl ether acrylate) (POEGMEA) with lower T_g increased ionic conductivity [218]. The authors further demonstrated that the printed elec-

trolyte could be used in the supercapacitor to successfully store and release electricity (Fig. 18i).

5. Summary and outlook

PIMS has proven to be a powerful tool for the facile, scalable, and moldable synthesis of nanostructured block polymer materials. In the course of block polymerization in highly concentrated solutions, the covalent junction between growing polymer blocks effectively suppresses macrophase separation and restrains the characteristic length scale to the radius of gyration of the forming block polymer. Copolymerization with a cross-linker is a distinct benefit of the PIMS process that enables to capture transient morphologies *in situ*. Specifically, the disordered bicontinuous morphology can be reliably arrested within robust monolithic materials with control over the length scale and provide synergetic combinations of functions with mechanical attributes. The ease of the macro-CTA synthesis makes the RAFT polymerization suitable for the PIMS process, particularly combined with ring-opening transesterification polymerization. High functional group tolerance and compatibility with various polymerization methods (especially neat polymerization) of RAFT polymerization can be exploited in the PIMS process to expand the polymer combinations and achievable product forms.

There exists vast room for PIMS to advance further. Some obvious opportunities and challenges are proposed below:

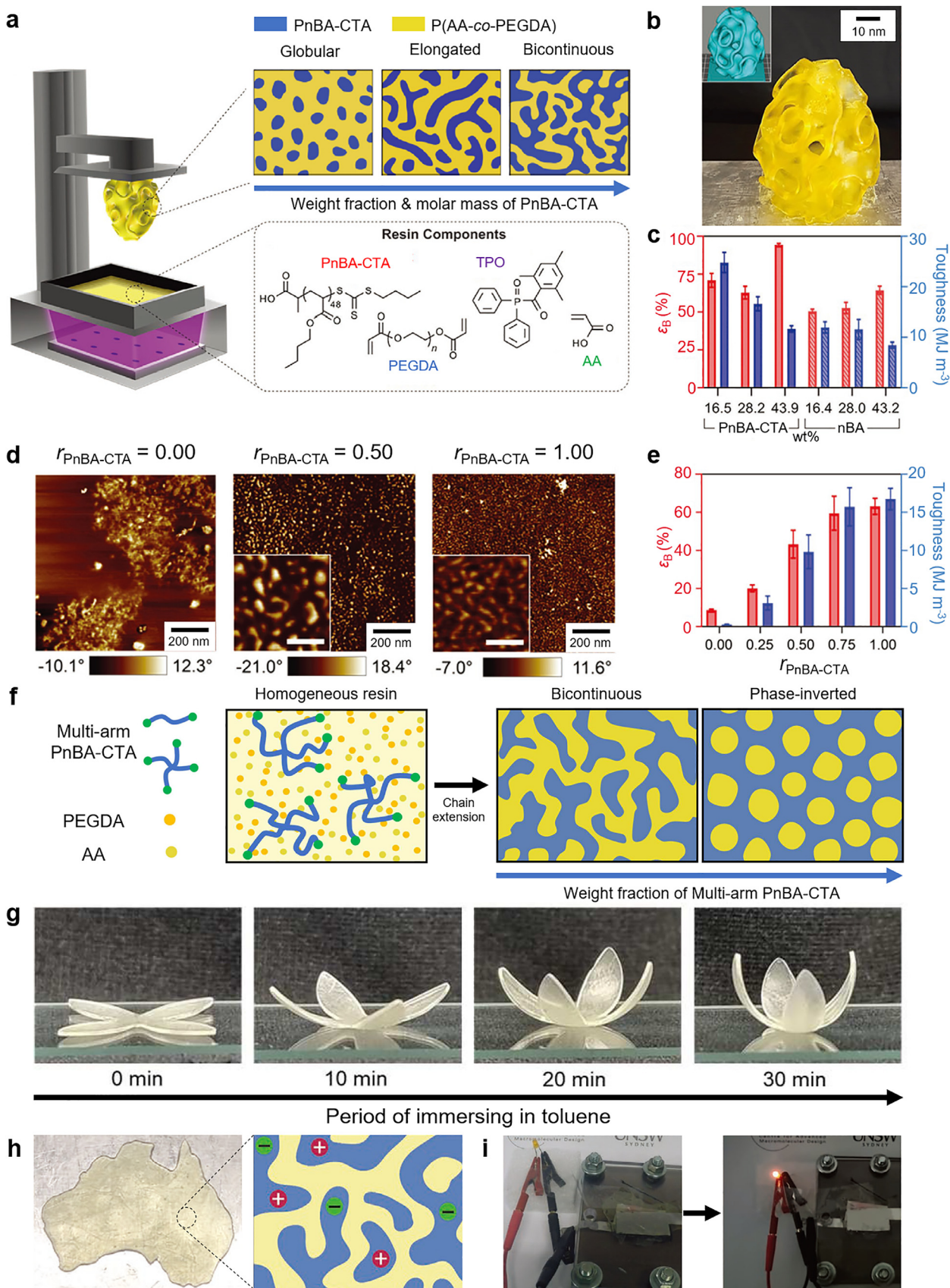


Fig. 18. 3D printing of PIMS materials. (a) Illustration of DLP-based 3D printing process. The PnBA-CTA/AA/PEGDA formulation is used with TPO as a photoradical initiator. Morphological transitions as a function of the weight fraction and the molar mass of PnBA-CTA are also depicted. (b) Representative photo of a printed object. (c) Elongation at break (ϵ_B) and toughness of the 3D-printed PIMS materials (marked with "PnBA-CTA") compared to P(nBA-co-AA-co-PEGDA) copolymers (marked with "nBA"). (d-e) AFM images (d) and mechanical properties (e) of the printed materials as a function of the ratio of PnBA-CTA to PnBA homopolymer. (f) Transition to a phase-inverted

Beyond RAFT. The PIMS process requires that the controlled polymerization proceeds in neat monomers or with minimal solvent to keep the product's monolithic character. While RAFT polymerization of liquid vinyl monomers meets the criterion well and has been the only choice so far, adopting other polymerization mechanisms in PIMS could drastically expand the possible polymer combinations for the *in situ* nanostructuring. Nitroxide-mediated polymerization is one apparent option particularly well suited to the neat polymerization of styrenic and acrylate monomers in a controlled manner. ATRP should also be applicable, and a reference example demonstrated ATRP of styrene/DVB in the presence of polychlorotrifluoroethylene-based graft copolymer containing PLA side chains produces cross-linked materials that can be rendered mesoporous by PLA removal [219]. Ring-opening metathesis polymerization can be another interesting candidate. We note that all these polymerizations have been utilized for synthesizing macroporous monolithic column materials following the PIPS mechanism [40,42,220].

Access to ordered morphologies. *In situ* cross-linking by copolymerization with multivinyl monomers has been beneficial for arresting the disordered bicontinuous morphology, which has been one of the main assets of PIMS. However, ordered morphologies can offer distinct advantages over the disordered version originating from the periodic nanostructure, such as photonic bandgaps, which allow long-range wave propagation or frequency-selective omnidirectional reflection, respectively [221]. While performing PIMS with no or very small cross-linker loading could give access to ordered phases, insufficient cross-linking density would be detrimental to the structural integrity and homogeneity of the PIMS product. As discussed in Section 2.2, increasing χ between the polymer blocks while ensuring the miscibility at the polymer-monomer mixture would be the key to creating cross-linking stabilized periodic nanostructures. Ordered network phases, including gyroid, may be noteworthy targets for PIMS, particularly for photonic applications, yet more challenging because of the narrow phase window.

Multidomain structures. Using diblock macro-CTAs and a mixture of two incompatible macro-CTAs demonstrated that the PIMS process can create more than two domains. The diblock macro-CTAs have proven their utility for tailoring the pore surface chemistries. As a recent example illustrated, middle block engineering would enable more sophisticated control over the environment of the porous channel by adjusting the microphase separation behavior and regulating the chain conformation after the sacrificial block removal [177]. The middle block could also be useful for interface engineering in nonporous systems, especially if different species should travel through individual domains and meet at the interface for a reaction.

Multiblock macro-CTAs would further increase the number of domains responsible for various functions, allowing the utilization of their interplay in the output as a response to external stimuli. Because microphase separation of multiblock polymers can be very complex [222], the block sequence and χ would need to be very carefully designed to achieve the target morphology. One-pot block polymerization of multicomponent monomer mixtures, for example, by utilizing the monomer reactivity differences [117] and frustrated Lewis pair polymerization [223], may be useful to this end from the synthetic perspective.

Thin film fabrication. Free-standing nanoporous films have been successfully fabricated via the PIMS process with a uniform pore

structure throughout the whole thickness. Perhaps a more ideal structure would be an asymmetric membrane consisting of the PIMS-derived nanoporous thin layer on top of a highly macroporous support membrane. The resulting thin film composite membrane would combine the size selectivity of the thin layer and the high flux provided by the support, as demonstrated in the reverse osmosis membranes [224]. However, PIMS is incompatible with thin film fabrication techniques such as spin coating, as a typical PIMS formulation includes volatile monomers that would evaporate quickly. Nonvolatile polymerization mixtures with appropriate viscosities would need to be developed, processed into thin films, and polymerized in ambient conditions without heating (photopolymerization, for example) to minimize the material loss and support deformation. We note that other polymer-based methodologies for the bicontinuous structure formation, such as the randomly end-linked copolymer network [83–87] and the cross-linking above the order-disorder transition temperature [106,225–228], may avoid the monomer evaporation issue. Interfacial engineering to retain the bicontinuous morphology on the surface of the thin film could be another challenge. Interestingly, direct etching of the PIMS materials without additional treatment produces nanoporous polymers with open pores on the surface, suggesting that the morphology is reserved.

The possibilities for creating advanced multicomponent materials via the PIMS process are fascinating. We hope this article will catalyze new research in this exciting area, and we look forward to the next set of scientific and technological advances.

Abbreviation: AA, Acrylic acid; BET, Brunauer-Emmett-Teller; BJH, Barrett-Joyner-Halenda; BMITFSI, 1-Butyl-3-methylimidazolium bis(trifluoromethylsulfonyl)imide; CTA, Chain-transfer agent; C₈mimNtf₂, 1-Octyl-3-methylimidazolium bis-(trifluoromethyl sulfonyl)imide; C₁₂mimNtf₂, 1-Dodecyl-3-methylimidazolium bis(trifluoromethyl sulfonyl)imide; DMA, N,N-dimethylacrylamide; DSC, Differential scanning calorimetry; DVB, Divinylbenzene; EGDA: Ethylene glycol diacrylate; EGDMA, Ethylene glycol dimethacrylate; HELmTFSI, 1-Ethylimidazolium bis(trifluoromethylsulfonyl)imide; HIPE, High internal phase emulsion; HPP, Hierarchically porous polymer; IBA, Isobornyl acrylate; IEC, Ion exchange capacity; LiTFSI, Lithium bis(trifluoromethylsulfonyl)imide; MMA, Methyl methacrylate; MVCL, Multivinyl cross-linker; mVSZ, Modified vinylsilazane; NLDFT, Nonlinear density functional theory; PB, Polybutadiene; PCL, Poly(ϵ -caprolactone); PDMS, Polydimethylsiloxane; PEO, Poly(ethylene oxide); PI, Polyisoprene; PIPS, Polymerization-induced phase separation; PISA, Polymerization-induced self-assembly; PLA, Polylactide; PnBA, Poly(*n*-butyl acrylate); POEG-MEA, poly(oligoethylene glycol methyl ether acrylate); PoSSE, Poly(*n*-octyl styrene sulfonic ester); PtBA, Poly(*tert*-butyl acrylate); PVA, Poly(vinyl alcohol); P4MCL, Poly(γ -methyl- ϵ -caprolactone); QSDFT, Quenched solid density functional theory; RAFT, Reversible addition-fragmentation chain transfer; ROTEP, Ring-opening transesterification polymerization; S, Styrene; SANS, Small-angle neutron scattering; SAXS, Small-angle X-ray scattering; SEM, Scanning electron microscopy; SN, Succinonitrile; tBuS, *tert*-Butylstyrene; TEM, Transmission electron microscopy; *T_g*, Glass transition temperature; TGA, Thermogravimetric analysis; TMPTA, Trimethylolpropane triacrylate; TMSS, Trimethylsilylstyrene; TP, 2,3,6,7,10,11-Hexakis(4-vinylphenyl)triphenylene; VBP, 4-Vinylbiphenyl; VbZCl, 4-Vinylbenzyl chloride; 2VN, 2-Vinylnaphthalene; 3VBP, 1,3,5-Tris(4-

morphology with multi-arm PnBA-CTAs. (g) Swelling-induced shape change of the material produced by combining PIMS and non-PIMS materials. (h) 3D printed solid polymer electrolyte following the shape of Australia. The PEO-CTA/IBA/TMPTA combination was used with BMITFSI as an additive. (i) Demonstration of turning LED off and on in the supercapacitor setup. (a-e) [214], Copyright 2022. Adapted with permission from John Wiley & Sons Inc. [215], Copyright 2022. Adapted with permission from Springer Nature. (f-g) [216], Copyright 2022. Adapted with permission from John Wiley & Sons Inc. (h-i) [217], Copyright 2022. Adapted with permission from John Wiley & Sons Inc.

vinylphenyl) benzene; 4VBM, Tetrakis(4-vinylbiphenyl)methane; 4VP, 4-Vinylpyridine.

Declaration of Competing Interest

The authors declare that they have no known competing financial interests or personal relationships that could have appeared to influence the work reported in this paper.

CRediT authorship contribution statement

Taeseok Oh: Visualization, Writing – original draft. **Suchan Cho:** Visualization, Writing – original draft. **Changsu Yoo:** Visualization, Writing – original draft. **Wonjune Yeo:** Visualization, Writing – original draft. **Jinyeong Oh:** Visualization, Writing – original draft. **Myungeun Seo:** Conceptualization, Funding acquisition, Supervision, Visualization, Writing – review & editing.

Data availability

No data was used for the research described in the article.

Acknowledgements

This work was supported by the National Research Foundation of Korea (NRF) grant funded by the Korea government (MSIT) (2023R1A2C2005705 and 2018R1A5A1025208), the Basic Science Research Program through NRF funded by the Ministry of Education (2019R111A2A01063804), and the Bio-Industrial Technology Development Program funded by the Ministry of Trade, Industry and Energy (20008628).

References

- [1] Bates FS, Fredrickson GH. Block copolymers—Designer soft materials. *Phys Today* 1999;52:32–8.
- [2] Zhang L, Yu K, Eisenberg A. Ion-induced morphological changes in “crew-cut” aggregates of amphiphilic block copolymers. *Science* 1996;272:1777–9.
- [3] Shen H, Zhang L, Eisenberg A. Multiple pH-induced morphological changes in aggregates of polystyrene-*block*-poly(4-vinylpyridine) in DMF/H₂O mixtures. *J Am Chem Soc* 1999;121:2728–40.
- [4] Mai Y, Eisenberg A. Self-assembly of block copolymers. *Chem Soc Rev* 2012;41:5969–85.
- [5] Thomas EL, Anderson DM, Henkee CS, Hoffman D. Periodic area-minimizing surfaces in block copolymers. *Nature* 1988;334:598–601.
- [6] Bates FS. Polymer-polymer phase behavior. *Science* 1991;251:898–905.
- [7] van Hest JCM, Delnoye DAP, Baars MWPL, van Genderen MHP, Meijer EW. Polystyrene-dendrimer amphiphilic block copolymers with a generation-dependent aggregation. *Science* 1995;268:1592–5.
- [8] Blanz A, Armes SP, Ryan AJ. Self-assembled block copolymer aggregates: from micelles to vesicles and their biological applications. *Macromol Rapid Commun* 2009;30:267–77.
- [9] Zhang L, Eisenberg A. Multiple morphologies of “crew-cut” aggregates of polystyrene-*b*-poly(acrylic acid) block copolymers. *Science* 1995;268:1728–31.
- [10] Drobny JG. 14 – thermoplastic elastomers based on recycled rubber and plastics. In: Drobny JG, editor. *Handbook of thermoplastic elastomers*. Oxford, UK: William Andrew publications; 2007. p. 277–9.
- [11] Cabral H, Miyata K, Osada K, Kataoka K. Block copolymer micelles in nanomedicine applications. *Chem Rev* 2018;118:6844–92.
- [12] Kim HC, Park SM, Hinsberg WD. Block copolymer based nanostructures: materials, processes, and applications to electronics. *Chem Rev* 2010;110:146–77.
- [13] Phillip WA, O'Neill B, Rodwogin M, Hillmyer MA, Cussler EL. Self-assembled block copolymer thin films as water filtration membranes. *ACS Appl Mater Interfaces* 2010;2:847–53.
- [14] Jackson EA, Hillmyer MA. Nanoporous membranes derived from block copolymers: from drug delivery to water filtration. *ACS Nano* 2010;4:3548–53.
- [15] Khandpur AK, Foerster S, Bates FS, Hamley IW, Ryan AJ, Bras W, Almdal K, Mortensen K. Polyisoprene-polystyrene diblock copolymer phase diagram near the order-disorder transition. *Macromolecules* 1995;28:8796–806.
- [16] Cao J, Tan Y, Chen Y, Zhang L, Tan J. Expanding the scope of polymerization-induced self-assembly: recent advances and new horizons. *Macromol Rapid Commun* 2021;42:2100498.
- [17] Lequieu J, Magenau AJD. Reaction-induced phase transitions with block copolymers in solution and bulk. *Polym Chem* 2021;12:12–28.
- [18] Penfold NJW, Yeow J, Boyer C, Armes SP. Emerging trends in polymerization-induced self-assembly. *ACS Macro Lett* 2019;8:1029–54.
- [19] Liu C, Hong CY, Pan CY. Polymerization techniques in polymerization-induced self-assembly (PISA). *Polym Chem* 2020;11:3673–89.
- [20] D'Agosto F, Rieger J, Lansalot M. RAFT-mediated polymerization-induced self-assembly. *Angew Chem Int Ed* 2020;59:8368–92.
- [21] Derry MJ, Fielding LA, Armes SP. Polymerization-induced self-assembly of block copolymer nanoparticles via RAFT non-aqueous dispersion polymerization. *Prog Polym Sci* 2016;52:1–18.
- [22] Seo M, Hillmyer MA. Reticulated nanoporous polymers by controlled polymerization-induced microphase separation. *Science* 2012;336:1422–5.
- [23] Paul DR, Bucknall CB. *Polymer blends*. New York: Wiley-interscience; 2000.
- [24] Sperling LH. *Polymeric multicomponent materials*. New York: Wiley-interscience; 1997.
- [25] Williams RJJ, Rozenberg BA, Pascault JP. Reaction-induced phase separation in modified thermosetting polymers. In: *Polymer analysis polymer physics*. Berlin, Heidelberg: Springer Berlin Heidelberg; 1997. p. 95–156.
- [26] Inoue T. Reaction-induced phase decomposition in polymer blends. *Prog Polym Sci* 1995;20:119–53.
- [27] Yamanaka K, Takagi Y, Inoue T. Reaction-induced phase separation in rubber-modified epoxy resins. *Polymer (Guildf)* 1989;30:1839–44.
- [28] Ryan AJ. Spinodal decomposition during bulk copolymerization: reaction injection moulding. *Polymer (Guildf)* 1990;31:707–12.
- [29] Yang WP, Macosko CW. Phase separation during fast (RIM) poly-urethane polymerization. *Makromol Chem Macromol Symp* 1989;25:23–44.
- [30] Li W, Ryan AJ, Meier IK. Morphology development via reaction-induced phase separation in flexible polyurethane foam. *Macromolecules* 2002;35:5034–42.
- [31] Doane JW, Golemme A, West JL, Whitehead JB, Wu BG. Polymer dispersed liquid crystals for display application. *Mol Cryst Liq Cryst Inc Nonlinear Opt* 1988;165:511–32.
- [32] Drzaic PS. Polymer dispersed nematic liquid crystal for large area displays and light valves. *J Appl Phys* 1986;60:2142–8.
- [33] Svec F. Preparation and HPLC applications of rigid macroporous organic polymer monoliths. *J Sep Sci* 2004;27:747–66.
- [34] Pucci V, Raggi MA, Svec F, Fréchet MJM. Monolithic columns with a gradient of functionalities prepared via photoinitiated grafting for separations using capillary electrochromatography. *J Sep Sci* 2004;27:779–88.
- [35] Viklund C, Svec F, Fréchet MJM, Irgum K. Monolithic, “molded”, porous materials with high flow characteristics for separations, catalysis, or solid-phase chemistry: Control of porous properties during polymerization. *Chem Mater* 1996;8:744–50.
- [36] Tsujioka N, Ishizuka N, Tanaka N, Kubo T, Hosoya K. Well-controlled 3D skeletal epoxy-based monoliths obtained by polymerization induced phase separation. *J Polym Sci Part A: Polym Chem* 2008;46:3272–81.
- [37] Palm A, Novotny MV. Macroporous polyacrylamide/poly(ethylene glycol) matrices as stationary phases in capillary electrochromatography. *Anal Chem* 1997;69:4499–507.
- [38] Moravcová D, Jandera P, Urban J, Planeta J. Characterization of polymer monolithic stationary phases for capillary HPLC. *J Sep Sci* 2003;26:1005–16.
- [39] Peters EC, Svec F, Fréchet MJM, Viklund C, Irgum K. Control of porous properties and surface chemistry in “molded” porous polymer monoliths prepared by polymerization in the presence of TEMPO. *Macromolecules* 1999;32:6377–9.
- [40] Viklund C, Nordström A, Irgum K, Svec F, Fréchet MJM. Preparation of porous poly(styrene-*co*-divinylbenzene) monoliths with controlled pore size distributions initiated by stable free radicals and their pore surface functionalization by grafting. *Macromolecules* 2001;34:4361–9.
- [41] Sinner F, Buchmeiser MR. A new class of continuous polymer supports prepared by ring-opening metathesis polymerization: A straightforward route to functionalized monoliths. *Macromolecules* 2000;33:5777–86.
- [42] Kanamori K, Hasegawa J, Nakanishi K, Hanada T. Facile synthesis of macroporous cross-linked methacrylate gels by atom transfer radical polymerization. *Macromolecules* 2008;41:7186–93.
- [43] Barlow KJ, Hao X, Hughes TC, Hutt OE, Polyzos A, Turner KA, Moad G. Porous, functional, poly(styrene-*co*-divinylbenzene) monoliths by RAFT polymerization. *Polym Chem* 2014;5:722–32.
- [44] Hillmyer MA, Lipic PM, Hajduk DA, Almdal K, Bates FS. Self-assembly and polymerization of epoxy resin-amphiphilic block copolymer nanocomposites. *J Am Chem Soc* 1997;119:2749–50.
- [45] Lipic PM, Bates FS, Hillmyer MA. Nanostructured thermosets from self-assembled amphiphilic block copolymer/epoxy resin mixtures. *J Am Chem Soc* 1998;120:8963–70.
- [46] Meng F, Zheng S, Zhang W, Li H, Liang Q. Nanostructured thermosetting blends of epoxy resin and amphiphilic poly(ϵ -caprolactone)-*block*-polybutadiene-*block*-poly(ϵ -caprolactone) tri-block copolymer. *Macromolecules* 2006;39:711–19.
- [47] Fischer M, Hellmann GP. On the evolution of phase patterns during the high-impact-modified polystyrene process. *Macromolecules* 1996;29:2498–509.
- [48] Bras W, Derbyshire GE, Bogg D, Cooke J, Elwell MJ, Komanshek BU, Naylor S, Ryan AJ. Simultaneous studies of reaction kinetics and structure development in polymer processing. *Science* 1995;267:996–9.
- [49] Ryan AJ, Hamley IW, Bras W, Bates FS. Structure development in semicrystalline diblock copolymers crystallizing from the ordered melt. *Macromolecules* 1995;28:3860–8.

- [50] Fetters LJ, Balsara NP, Huang JS, Jeon HS, Almdal K, Lin MY. Aggregation in living polymer solutions by light and neutron scattering: a study of model ionomers. *Macromolecules* 1995;28:4996–5005.
- [51] Stellbrink J, Willner L, Jucknischke O, Richter D. Self-assembling behavior of living polymers. *Macromolecules* 1998;31:4189–97.
- [52] Stellbrink J, Allgaier J, Willner L, Richter D, Slaweki T, Fetters LJ. Real time SANS study on head group self-assembly for lithium based anionic polymerizations. *Polymer (Guildf)* 2002;43:7101–9.
- [53] Niu AZ, Stellbrink J, Allgaier J, Willner L, Radulescu A, Richter D, Koenig BW, May RP, Fetters LJ. An *in situ* study of the *t*-butyllithium initiated polymerization of butadiene in *D*-heptane via small angle neutron scattering and ¹H NMR. *J Chem Phys* 2005;122:134906.
- [54] Watanabe H, Oishi Y, Kanaya T, Kaji H, Horii F. Rheology of living bifunctional polybutadienyl dilithium chains in benzene: viscoelastic evaluation of aggregate lifetime. *Macromolecules* 2003;36:220–8.
- [55] Motokawa R, Nakahira T, Annaka M, Hashimoto T, Koizumi S. Time-resolved gel permeation chromatographic study on poly(*N*-isopropylacrylamide)-*block*-poly(ethylene glycol) prepared by soap-free emulsion polymerization. *Polymer (Guildf)* 2004;45:9019–22.
- [56] Yamauchi K, Hasegawa H, Hashimoto T, Tanaka H, Motokawa R, Koizumi S. Direct observation of polymerization-reaction-induced molecular self-assembling process: In-situ and real-time SANS measurements during living anionic polymerization of polyisoprene-*block*-polystyrene. *Macromolecules* 2006;39:4531–9.
- [57] Motokawa R, Iida Y, Zhao Y, Hashimoto T, Koizumi S. Living polymerization induced macro- and microdomain investigated by focusing ultra-small-angle neutron scattering. *Polym J* 2007;39:1312–18.
- [58] Iida Y, Kawakatsu T, Motokawa R, Koizumi S, Hashimoto T. Transition in domain morphology of block copolymers undergoing polymerization. *Macromolecules* 2008;41:9722–6.
- [59] Motokawa R, Koizumi S, Hashimoto T, Annaka M, Nakahira T. Soap-free emulsion polymerization of poly(ethylene glycol)-*block*-poly(*N*-isopropylacrylamide): elucidation of specific reaction fields for quasi-living polymerization by time-resolved SANS. *Macromolecules* 2009;43:752–64.
- [60] Zhang X, Boissé S, Zhang W, Beaunier P, D'Agosto F, Rieger J, Charleux B. Well-defined amphiphilic block copolymers and nano-objects formed *in situ* via RAFT-mediated aqueous emulsion polymerization. *Macromolecules* 2011;44:4149–58.
- [61] Zhang W, Charleux B, Cassagnau P. Viscoelastic properties of water suspensions of polymer nanofibers synthesized via RAFT-mediated emulsion polymerization. *Macromolecules* 2012;45:5273–80.
- [62] Blanz A, Madsen J, Battaglia G, Ryan AJ, Armes SP. Mechanistic insights for block copolymer morphologies: how do worms form vesicles? *J Am Chem Soc* 2011;133:16581–7.
- [63] Chambon P, Blanz A, Battaglia G, Armes SP. Facile synthesis of methacrylic ABC triblock copolymer vesicles by RAFT aqueous dispersion polymerization. *Macromolecules* 2012;45:5081–90.
- [64] Blanz A, Ryan AJ, Armes SP. Predictive phase diagrams for RAFT aqueous dispersion polymerization: effect of block copolymer composition, molecular weight, and copolymer concentration. *Macromolecules* 2012;45:5099–107.
- [65] Warren NJ, Armes SP. Polymerization-induced self-assembly of block copolymer nano-objects via RAFT aqueous dispersion polymerization. *J Am Chem Soc* 2014;136:10174–85.
- [66] Charleux B, Delaitre G, Rieger J, D'Agosto F. Polymerization-induced self-assembly: from soluble macromolecules to block copolymer nano-objects in one step. *Macromolecules* 2012;45:6753–65.
- [67] Murray JG, Schwab FC. Organic fillers by anionic dispersion polymerization. *Ind Eng Chem Prod Res Dev* 1982;21:93–6.
- [68] Okay O, Funke W. Anionic dispersion polymerization of 1,4-divinylbenzene. *Macromolecules* 1990;23:2623–8.
- [69] Kim J, Jeong SY, Kim KU, Ahn YH, Quirk RP. Anionic dispersion polymerization. I. control of particle size. *J Polym Sci Part A: Polym Chem* 1996;34:3277–88.
- [70] Zheng G, Pan C. Reversible addition-fragmentation transfer polymerization in nanosized micelles formed *in situ*. *Macromolecules* 2006;39:95–102.
- [71] Park J, Saba SA, Hillmyer MA, Kang DC, Seo M. Effect of homopolymer in polymerization-induced microphase separation process. *Polymer (Guildf)* 2017;126:338–51.
- [72] Park J, Ahn NY, Seo M. Cross-linking polymerization-induced self-assembly to produce branched core cross-linked star block polymer micelles. *Polym Chem* 2020;11:4335–43.
- [73] Rymaruk MJ, O'Brien CT, Gyorgy C, Darmau B, Jennings J, Mykhaylyk OO, Armes SP. Small-angle X-ray scattering studies of block copolymer nano-objects: formation of ordered phases in concentrated solution during polymerization-induced self-assembly. *Angew Chem Int Ed* 2021;60:12955–63.
- [74] Zofchak ES, LaNasa JA, Mei W, Hickey RJ. Polymerization-induced nanostructural transition driven by *in situ* polymer grafting. *ACS Macro Lett* 2018;7:822–7.
- [75] Zofchak ES, LaNasa JA, Torres VM, Hickey RJ. Deciphering the complex phase behavior during polymerization-induced nanostructural transitions of a block polymer/monomer blend. *Macromolecules* 2020;53:835–43.
- [76] Torres VM, LaNasa JA, Vogt BD, Hickey RJ. Mixed, controlling nanostructure and mechanical properties in triblock copolymer/monomer blends via reaction-induced phase transitions. *Soft Matter* 2021;17:1505–12.
- [77] Howe DH, Hart JL, McDaniel RM, Taheri ML, Magenau AJD. Functionalization-induced self-assembly of block copolymers for nanoparticle synthesis. *ACS Macro Lett* 2018;7:1503–8.
- [78] Howe DH, Jenewein KJ, Hart JL, Taheri ML, Magenau AJD. Functionalization-induced self-assembly under ambient conditions via thiol-epoxide “click” chemistry. *Polym Chem* 2020;11:298–303.
- [79] Su L, Wang C, Frank P, Lu Y, Chen G, Jiang M. Glyco-inside micelles and vesicles directed by protection-deprotection chemistry. *ACS Macro Lett* 2014;3:534–9.
- [80] Qi W, Zhang Y, Wang J, Tao G, Wu L, Kochovski Z, Gao H, Chen G, Jiang M. Deprotection-induced morphology transition and immunoactivation of glycovesicles: a strategy of smart delivery polymersomes. *J Am Chem Soc* 2018;140:8851–7.
- [81] Wu X, Su L, Chen G, Jiang M. Deprotection-induced micellization of glycopolymers: control of kinetics and morphologies. *Macromolecules* 2015;48:3705–12.
- [82] Yamamoto K, Ito E, Fukaya S, Takagi H. Phase-separated conetwork structure induced by radical copolymerization of poly(dimethylsiloxane)- α,ω -diacrylate and *N,N*-dimethylacrylamide. *Macromolecules* 2009;42:9561–7.
- [83] Walker CN, Bryson KC, Hayward RC, Tew GN. Wide bicontinuous compositional windows from co-networks made with telechelic macromonomers. *ACS Nano* 2014;8:12376–85.
- [84] Zeng D, Ribbe A, Hayward RC. Anisotropic and interconnected nanoporous materials from randomly end-linked copolymer networks. *Macromolecules* 2017;50:4668–76.
- [85] Zeng D, Ribbe A, Kim H, Hayward RC. Stress-induced orientation of cocontinuous nanostructures within randomly end-linked copolymer networks. *ACS Macro Lett* 2018;7:828–33.
- [86] Zeng D, Hayward RC. Effects of randomly end-linked copolymer network parameters on the formation of disordered cocontinuous phases. *Macromolecules* 2019;52:2642–50.
- [87] Zeng D, Gupta R, Coughlin EB, Hayward RC. Assembly of disordered cocontinuous morphologies by multiblock copolymers with random block sequence and length dispersity. *ACS Appl Polym Mater* 2020;2:3282–90.
- [88] Matsen MW. Effect of architecture on the phase behavior of AB-type block copolymer melts. *Macromolecules* 2012;45:2161–5.
- [89] Huang CI, Lodge TP. Self-consistent calculations of block copolymer solution phase behavior. *Macromolecules* 1998;31:3556–65.
- [90] Lodge TP, Pudil B, Hanley KJ. The full phase behavior for block copolymers in solvents of varying selectivity. *Macromolecules* 2002;35:4707–17.
- [91] Motokawa R, Koizumi S, Zhao Y, Hashimoto T. *In situ* and time-resolved ultra small-angle neutron scattering observation on growing poly(methyl methacrylate)-*block*-polystyrene via reversible addition-fragmentation chain transfer living radical polymerization. *J Appl Crystallogr* 2007;40:s645–9.
- [92] Bates FS. Measurement of the correlation hole in homogeneous block copolymer melts. *Macromolecules* 1985;18:525–8.
- [93] Motokawa R, Taniguchi T, Kumada T, Iida Y, Aoyagi S, Sasaki Y, Kohri M, Kishikawa K. Photonic crystals fabricated by block copolymerization-induced microphase separation. *Macromolecules* 2016;49:6041–9.
- [94] Isozaki Y, Higashiharaguchi S, Kaneko N, Yamazaki S, Taniguchi T, Karatsu T, Ueda Y, Motokawa R. Polymer photonic crystals prepared by triblock copolymerization-induced *in situ* microphase separation. *Chem Lett* 2022;51:625–8.
- [95] Rosedale JH, Bates FS, Almdal K, Mortensen K, Wignall GD. Order and disorder in symmetric diblock copolymer melts. *Macromolecules* 1995;28:1429–43.
- [96] Bates FS, Wiltzius P. Spinodal decomposition of a symmetric critical mixture of deuterated and protonated polymer. *J Chem Phys* 1989;91:3258–74.
- [97] Hashimoto T. Time-dependent Ginzburg-Landau approach for microphase-separation kinetics of block polymers. *Macromolecules* 1987;20:465–8.
- [98] Connell JG, Richards RW, Rennie AR. Phase-separation kinetics in concentrated solutions of linear diblock copolymers of polystyrene and polyisoprene from time-resolved small-angle neutron scattering. *Polymer (Guildf)* 1991;32:2033–42.
- [99] Erlebacher J, Aziz MJ, Karma A, Dimitrov N, Sieradzki K. Evolution of nanoporosity in dealloying. *Nature* 2001;410:450–3.
- [100] Zhou N, Bates FS, Lodge TP. Mesoporous membrane templated by a polymeric bicontinuous microemulsion. *Nano Lett* 2006;6:2354–7.
- [101] Mao H, Hillmyer MA. Macroscopic samples of polystyrene with ordered three-dimensional nanochannels. *Soft Matter* 2006;2:57–9.
- [102] Ndoni S, Vigild ME, Berg RH. Nanoporous materials with spherical and gyroid cavities created by quantitative etching of polydimethylsiloxane in polystyrene-polydimethylsiloxane block copolymers. *J Am Chem Soc* 2003;125:13366–7.
- [103] Li L, Schulte L, Clausen LD, Hansen KM, Jonsson GE, Ndoni S. Gyroid nanoporous membranes with tunable permeability. *ACS Nano* 2011;5:7754–66.
- [104] Schulte L, Grydgaard A, Jakobsen MR, Szweczykowski PP, Guo F, Vigild ME, Berg RH, Ndoni S. Nanoporous materials from stable and metastable structures of 1,2-PB-*b*-PDMS block copolymers. *Polymer (Guildf)* 2011;52:422–9.
- [105] Meuler AJ, Hillmyer MA, Bates FS. Ordered network mesostructures in block polymer materials. *Macromolecules* 2009;42:7221–50.
- [106] Vidil T, Hampu N, Hillmyer MA. Nanoporous thermosets with percolating pores from block polymers chemically fixed above the order-disorder transition. *ACS Cent Sci* 2017;3:1114–20.

- [107] Schulze MW, Hillmyer MA. Tuning mesoporosity in cross-linked nanostructured thermosets via polymerization-induced microphase separation. *Macromolecules* 2017;50:997–1007.
- [108] Bates FS, Fredrickson GH. Block copolymer thermodynamics: theory and experiment. *Annu Rev Phys Chem* 1990;41:525–57.
- [109] Lee J, Seo M. Downsizing of block polymer-templated nanopores to one nanometer via hyper-cross-linking of high χ -low N precursors. *ACS Nano* 2021;15:9154–66.
- [110] Baruth A, Seo M, Lin CH, Walster K, Shankar A, Hillmyer MA, Leighton C. Optimization of long-range order in solvent vapor annealed poly(styrene)-*block*-poly(lactide) thin films for nanolithography. *ACS Appl Mater Interfaces* 2014;6:13770–81.
- [111] McIntosh LD, Schulze MW, Irwin MT, Hillmyer MA, Lodge TP. Evolution of morphology, modulus, and conductivity in polymer electrolytes prepared via polymerization-induced phase separation. *Macromolecules* 2015;48:1418–28.
- [112] He Y, Boswell PG, Bühlmann P, Lodge TP. Ion gels by self-assembly of a tri-block copolymer in an ionic liquid. *J Phys Chem B* 2007;111:4645–52.
- [113] Simone PM, Lodge TP. Phase behavior and ionic conductivity of concentrated solutions of polystyrene-poly(ethylene oxide) diblock copolymers in an ionic liquid. *ACS Appl Mater Interfaces* 2009;1:2812–20.
- [114] Zhang S, Lee KH, Frisbie CD, Lodge TP. Ionic conductivity, capacitance, and viscoelastic properties of block copolymer-based ion gels. *Macromolecules* 2011;44:940–9.
- [115] Saba SA, Mousavi MP, Bühlmann P, Hillmyer MA. Hierarchically porous polymer monoliths by combining controlled macro- and microphase separation. *J Am Chem Soc* 2015;137:8896–9.
- [116] Seo M, Murphy CJ, Hillmyer MA. One-step synthesis of cross-linked block polymer precursor to a nanoporous thermoset. *ACS Macro Lett* 2013;2:617–20.
- [117] Gavrilov AA, Chertovich AV. Polymerization-induced microphase separation with long-range order in melts of gradient copolymers. *Polymers (Basel)* 2020;12:2637.
- [118] Lu GM, Zhao XS. Nanoporous Materials: science and Engineering. World Scientific 2004.
- [119] Todd EM, Hillmyer MA. Porous Polymers from Self-Assembled Structures. In: Silverstein MS, Cameron NR, Hillmyer MA, editors. Porous polymers. Hoboken, NJ: John Wiley & Sons Inc; 2011. p. 31–78.
- [120] Eissa AM, Wilson P, Chen C, Collins J, Walker M, Haddleton DM, Cameron NR. Reversible surface functionalisation of emulsion-templated porous polymers using dithiophenol maleimide functional macromolecules. *Chem Commun* 2017;53:9789–92.
- [121] Atkins CJ, Seow DK, Burns G, Town JS, Hand RA, Lester DW, Cameron NR, Haddleton DM, Eissa AM. Branched macromonomers from catalytic chain transfer polymerisation (CCTP) as precursors for emulsion-templated porous polymers. *Polym Chem* 2020;11:3841–8.
- [122] Svec F, Frechet JM. Kinetic control of pore formation in macroporous polymers. formation of “molded” porous materials with high flow characteristics for separations or catalysis. *Chem Mater* 1995;7:707–15.
- [123] Kanamori K, Nakanishi K, Hanada T. Rigid macroporous poly(divinylbenzene) monoliths with a well-defined bicontinuous morphology prepared by living radical polymerization. *Adv Mater* 2006;18:2407–11.
- [124] Olson DA, Chen L, Hillmyer MA. Templating nanoporous polymers with ordered block copolymers. *Chem Mater* 2008;20:869–90.
- [125] Seo M. Robust mesoporous polymers derived from cross-linked block polymer precursors. In: Bettotti P, editor. Submicron porous materials. Switzerland: Springer Cham; 2017. p. 53–79.
- [126] Zalusky AS, Olayo-Valles R, Wolf JH, Hillmyer MA. Ordered nanoporous polymers from polystyrene-poly(lactide) block copolymers. *J Am Chem Soc* 2002;124:12764–73.
- [127] Lee JS, Hirao A, Nakahama S. Polymerization of monomers containing functional silyl groups. 5. Synthesis of new porous membranes with functional groups. *Macromolecules* 1988;21:274–6.
- [128] Lee JS, Hirao A, Nakahama S. Polymerization of monomers containing functional silyl groups. 7. Porous membranes with controlled microstructures. *Macromolecules* 1989;22:2602–6.
- [129] Chen HY, Kwon Y, Thornton K. Multifunctionality of three-dimensional self-assembled composite structure. *Scr Mater* 2009;61:52–5.
- [130] Xu P, Yu B. Developing a new form of permeability and Kozeny–Carman constant for homogeneous porous media by means of fractal geometry. *Adv Water Resour* 2008;31:74–81.
- [131] Muralidharan V, Hui CY. Stability of nanoporous materials. *Macromol Rapid Commun* 2004;25:1487–90.
- [132] Cavicchi KA, Zalusky AS, Hillmyer MA, Lodge TP. An ordered nanoporous monolith from an elastomeric crosslinked block copolymer precursor. *Macromol Rapid Commun* 2004;25:704–9.
- [133] Thommes M, Smarsly B, Groenewolt M, Ravikovitch PI, Neimark AV. Adsorption hysteresis of nitrogen and argon in pore networks and characterization of novel micro- and mesoporous silicas. *Langmuir* 2006;22:756–64.
- [134] Weber J, Bergström L. Impact of cross-linking density and glassy chain dynamics on pore stability in mesoporous poly(styrene). *Macromolecules* 2009;42:8234–40.
- [135] Barrett EP, Joyner LG, Halenda PP. The determination of pore volume and area distributions in porous substances. I. Computations from nitrogen isotherms. *J Am Chem Soc* 1951;73:373–80.
- [136] Brunauer S, Emmett PH, Teller E. Adsorption of gases in multimolecular layers. *J Am Chem Soc* 1938;60:309–19.
- [137] Larsen MB, Van Horn JD, Wu F, Hillmyer MA. Intrinsically hierarchical nanoporous polymers via polymerization-induced microphase separation. *Macromolecules* 2017;50:4363–71.
- [138] Satheeshkumar C, Seo M. Creation of micropores by RAFT copolymerization of conjugated multi-vinyl cross-linkers. *Polym Chem* 2018;9:5680–9.
- [139] Satheeshkumar C, Seo H, Hong S, Kim P, Seo M. Synthesis of triphenylene-based hierarchically porous monolith with nitroaromatic-sensitive fluorescence. *Polymer (Guildf)* 2023;265:125577.
- [140] Fontanals N, Marcé RM, Borrull F, Cormack PAG. Hypercrosslinked materials: preparation, characterisation and applications. *Polym Chem* 2015;6:7231–44.
- [141] Li B, Gong R, Wang W, Huang X, Zhang W, Li H, Hu C, Tan B. A new strategy to microporous polymers: knitting rigid aromatic building blocks by external cross-linker. *Macromolecules* 2011;44:2410–14.
- [142] Tan L, Tan B. Hypercrosslinked porous polymer materials: design, synthesis, and applications. *Chem Soc Rev* 2017;46:3322–56.
- [143] Seo M, Kim S, Oh J, Kim SJ, Hillmyer MA. Hierarchically porous polymers from hyper-cross-linked block polymer precursors. *J Am Chem Soc* 2015;137:600–3.
- [144] Kim S, Seo M. Control of porosity in hierarchically porous polymers derived from hyper-crosslinked block polymer precursors. *J Polym Sci Part A: Polym Chem* 2018;56:900–13.
- [145] Kim S, Varga G, Seo M, Sápi A, Rácz V, Gómez-Pérez JF, Sebők D, Lee J, Kukovecz Á, Kónya Z. Nesting well-defined Pt nanoparticles within a hierarchically porous polymer as a heterogeneous Suzuki–Miyaura catalyst. *ACS Appl Nano Mater* 2021;4:4070–6.
- [146] Lee J, Seo M. Hyper-cross-linked polymer with enhanced porosity by *in situ* removal of trimethylsilyl group via electrophilic aromatic substitution. *ACS Macro Lett* 2018;7:1448–54.
- [147] Saba SA, Lee B, Hillmyer MA. Tricontinuous nanostructured polymers via polymerization-induced microphase separation. *ACS Macro Lett* 2017;6:1232–6.
- [148] Hallinan DT, Balsara NP. Polymer electrolytes. *Annu Rev Mater Res* 2013;43:503–25.
- [149] Steele BCH, Heinzel A. Materials for fuel-cell technologies. *Nature* 2001;414:345–52.
- [150] Tarascon JM, Armand M. Issues and challenges facing rechargeable lithium batteries. *Nature* 2001;414:359–67.
- [151] Young WS, Kuan WF, Epps TH. Block copolymer electrolytes for rechargeable lithium batteries. *J Polym Sci Part B: Polym Phys* 2014;52:1–16.
- [152] Goodenough JB, Kim Y. Challenges for rechargeable Li batteries. *Chem Mater* 2010;22:587–603.
- [153] Goodenough JB, Park KS. The Li-ion rechargeable battery: a perspective. *J Am Chem Soc* 2013;135:1167–76.
- [154] Noda A, Susan MABH, Kudo K, Mitsushima S, Hayamizu K, Watanabe M. Brønsted acid-base ionic liquids as proton-conducting nonaqueous electrolytes. *J Phys Chem B* 2003;107:4024–33.
- [155] Nakamoto H, Watanabe M. Brønsted acid-base ionic liquids for fuel cell electrolytes. *Chem Commun* 2007;24:2539–41.
- [156] Hoarfrost ML, Tyagi MS, Segalman RA, Reimer JA. Effect of confinement on proton transport mechanisms in block copolymer/ionic liquid membranes. *Macromolecules* 2012;45:3112–20.
- [157] Monroe C, Newman J. The impact of elastic deformation on deposition kinetics at lithium/polymer interfaces. *J Electrochem Soc* 2005;152:A396.
- [158] Schulze MW, McIntosh LD, Hillmyer MA, Lodge TP. High-modulus, high-conductivity nanostructured polymer electrolyte membranes via polymerization-induced phase separation. *Nano Lett* 2014;14:122–6.
- [159] Chopade SA, Au JG, Li Z, Schmidt PW, Hillmyer MA, Lodge TP. Robust polymer electrolyte membranes with high ambient-temperature lithium-ion conductivity via polymerization-induced microphase separation. *ACS Appl Mater Interfaces* 2017;9:14561–5.
- [160] Chopade SA, So S, Hillmyer MA, Lodge TP. Anhydrous proton conducting polymer electrolyte membranes via polymerization-induced microphase separation. *ACS Appl Mater Interfaces* 2016;8:6200–10.
- [161] Liu L, Wu Z, Zheng Z, Zhou Q, Chen K, Yin P. Polymerization-induced microphase separation of polymer-polyoxometalate nanocomposites for anhydrous solid state electrolytes. *Chin Chem Lett* 2022;33:4326–30.
- [162] Chopade SA, Anderson EL, Schmidt PW, Lodge TP, Hillmyer MA, Bühlmann P. Self-supporting, hydrophobic, ionic liquid-based reference electrodes prepared by polymerization-induced microphase separation. *ACS Sens* 2017;2:1498–504.
- [163] Inzelt G, Lewenstam A, Scholz F. Handbook of reference electrodes. Heidelberg, Germany: Springer; 2013.
- [164] Kakiuchi T, Yoshimatsu T, Nishi N. New class of Ag/AgCl electrodes based on hydrophobic ionic liquid saturated with AgCl. *Anal Chem* 2007;79:7187–91.
- [165] Bae SH, Jeon C, Oh S, Kim CG, Seo M, Oh IK. Load-bearing supercapacitor based on bicontinuous PEO-*b*-P(S-*co*-DVB) structural electrolyte integrated with conductive nanowire-carbon fiber electrodes. *Carbon N Y* 2018;139:10–20.
- [166] Gauthier MA, Gibson MI, Klok HA. Synthesis of functional polymers by post-polymerization modification. *Angew Chem Int Ed* 2009;48:48–58.
- [167] Das A, Theato P. Activated ester containing polymers: opportunities and challenges for the design of functional macromolecules. *Chem Rev* 2016;116:1434–95.
- [168] Jeon C, Kim DW, Chang S, Kim JG, Seo M. Synthesis of polypropylene via catalytic deoxygenation of poly(methyl acrylate). *ACS Macro Lett* 2019;8:1172–8.

- [169] Jeon C, Han JJ, Seo M. Control of ion transport in sulfonated mesoporous polymer membranes. *ACS Appl Mater Interfaces* 2018;10:40854–62.
- [170] Jeon C, Choi C, Kim HT, Seo M. Achieving fast proton transport and high vanadium ion rejection with uniformly mesoporous composite membranes for high-efficiency vanadium redox flow batteries. *ACS Appl Energy Mater* 2020;3:5874–81.
- [171] Saito M, Arimura N, Hayamizu K, Okada T. Mechanisms of ion and water transport in perfluorosulfonated ionomer membranes for fuel cells. *J Phys Chem B* 2004;108:16064–70.
- [172] Zhou XL, Zhao TS, An L, Zeng YK, Wei L. Modeling of ion transport through a porous separator in vanadium redox flow batteries. *J Power Sources* 2016;327:67–76.
- [173] Tansel B, Sager J, Rector T, Garland J, Strayer RF, Levine L, Roberts M, Hummerick M, Bauer J. Significance of hydrated radius and hydration shells on ionic permeability during nanofiltration in dead end and cross flow modes. *Sep Purif Technol* 2006;51:40–7.
- [174] Goldfeld DJ, Silver ES, Valdez JM, Hillmyer MA. Bicontinuous ion-exchange materials through polymerization-induced microphase separation. *ACS Macro Lett* 2021;10:60–4.
- [175] Goldfeld DJ, Silver ES, Radlauer MR, Hillmyer MA. Synthesis and self-assembly of block polyelectrolyte membranes through a mild, 2-in-1 postpolymerization treatment. *ACS Appl Polym Mater* 2020;2:817–25.
- [176] Mao H, Arrechea PL, Bailey TS, Johnson BJ, Hillmyer MA. Control of pore hydrophilicity in ordered nanoporous polystyrene using an AB/AC block copolymer blending strategy. *Faraday Discuss* 2005;128:149–62.
- [177] Peterson CH, Werber JR, Lee HK, Hillmyer MA. Tailored mesoporous microspheres by polymerization-induced microphase separation in suspension. *ACS Appl Polym Mater* 2022;4:4219–33.
- [178] Qin J, Chen Y, Yan D, Xi F. Dispersible shaped nanoobjects from bulk microphase separation of high T_g block copolymers without chemical cross-linking. *Macromolecules* 2010;43:10652–8.
- [179] Hwang YH, Oh J, Ahn H, Kim DP, Seo M. Synthesis of *in situ* microphase-separated organic-inorganic block polymer precursors to 3D-continuous mesoporous SiC-based ceramic monoliths. *ACS Appl Polym Mater* 2020;2:2802–9.
- [180] Pham TA, Kim DP, Lim TW, Park SH, Yang DY, Lee KS. Three-dimensional SiCN ceramic microstructures via nano-sterolithography of inorganic polymer photoresists. *Adv Funct Mater* 2006;16:1235–41.
- [181] Colombo P, Mera G, Riedel R, Soraru GD. Polymer-derived ceramics: 40 years of research and innovation in advanced ceramics. *J Am Ceram Soc* 2010;93:1805–37.
- [182] Shi YF, Meng Y, Chen DH, Cheng SJ, Chen P, Yang HF, Wan Y, Zhao DY. Highly ordered mesoporous silicon carbide ceramics with large surface areas and high stability. *Adv Funct Mater* 2006;16:561–7.
- [183] Peterson C, Hillmyer MA. Fast photochromic dye response in rigid block polymer thermosets. *ACS Appl Polym Mater* 2019;1:2778–86.
- [184] Smets G. Photochromic behaviour of polymeric systems and related phenomena. *Pure Appl Chem* 1972;30:1–24.
- [185] Evans RA, Such GK. Research trends in photochromism: control of photochromism in rigid polymer matrices and other advances. *Aust J Chem* 2005;58:825–30.
- [186] Kryszewski M, Nadolski B, North AM, Pethrick RA. Kinetic matrix effects (response and density distribution functions): ring closure. Reaction of indolinobenzospiropyran in glassy poly(alkyl methacrylates). *J Chem Soc Faraday Trans* 1980;2(76):351–68.
- [187] Topchiyev DA. Photochromism of spiropyran in polymeric media. Some aspects and possibilities of regulating the spectral-kinetic characteristics. *Polym Sci U.S.S.R* 1990;32:2361–83.
- [188] Watts A, Kurokawa N, Hillmyer MA. Strong, resilient, and sustainable aliphatic polyester thermoplastic elastomers. *Biomacromolecules* 2017;18:1845–54.
- [189] Perrier S. 50th anniversary perspective: RAFT polymerization—A user guide. *Macromolecules* 2017;50:7433–47.
- [190] Rzaev J, Hillmyer MA. Nanochannel array plastics with tailored surface chemistry. *J Am Chem Soc* 2005;127:13373–9.
- [191] Oh J, Seo M. Photoinitiated polymerization-induced microphase separation for the preparation of nanoporous polymer films. *ACS Macro Lett* 2015;4:1244–8.
- [192] Hinze JO. Fundamentals of the hydrodynamic mechanism of splitting in dispersion processes. *AIChE J* 1955;1:289–95.
- [193] Zhang X, Zhao Y, Xu S, Yang Y, Liu J, Wei Y, Yang Q. Polystyrene sulphonic acid resins with enhanced acid strength via macromolecular self-assembly within confined nanospace. *Nat Commun* 2014;5:3170.
- [194] Boysen RI. Advances in the development of molecularly imprinted polymers for the separation and analysis of proteins with liquid chromatography. *J Sep Sci* 2019;42:51–71.
- [195] Arcos-Casarrubias JA, Cruz-Díaz MR, Cardoso-Martínez J, Vázquez-Arenas J, Caballero-Domínguez FV. Chromium adsorption into a macroporous resin based on vinylpyridine-divinylbenzene copolymers: thermodynamics, kinetics, and process dynamic in a fixed bed column. *Adsorption* 2018;24:105–20.
- [196] Han S, Zang Y, Gao Y, Yue Q, Zhang P, Kong W, Jin B, Xu X, Gao B. Co-monomer polymer anion exchange resin for removing Cr(VI) contaminants: adsorption kinetics, mechanism and performance. *Sci Total Environ* 2020;709:136002.
- [197] Simoes-Cardoso JC, Yoshimoto N, Yamamoto S. Thermodynamic analysis of polyphenols retention in polymer resin chromatography by van't Hoff plot and isothermal titration calorimetry. *J Chromatogr A* 2019;1608:460405.
- [198] Oh J, Kim B, Lee S, Kim SH, Seo M. Semipermeable microcapsules with a block-polymer-templated nanoporous membrane. *Chem Mater* 2018;30:273–9.
- [199] Utada AS, Lorceau E, Link DR, Kaplan PD, Stone HA, Weitz DA. Monodisperse double emulsions generated from a microcapillary device. *Science* 2005;308:537–41.
- [200] Kim SH, Kim JW, Cho JC, Weitz DA. Double-emulsion drops with ultra-thin shells for capsule templates. *Lab Chip* 2011;11:3162–6.
- [201] Datta SS, Abbaspourrad A, Amstad E, Fan J, Kim SH, Romanowsky M, Shum HC, Sun B, Utada AS, Windbergs M, Zhou S, Weitz DA. 25th anniversary article: double emulsion templated solid microcapsules: mechanics and controlled release. *Adv Mater* 2014;26:2205–18.
- [202] Kim B, Lee TY, Abbaspourrad A, Kim SH. Perforated microcapsules with selective permeability created by confined phase separation of polymer blends. *Chem Mater* 2014;26:7166–71.
- [203] Kim B, Jeon TY, Oh YK, Kim SH. Microfluidic production of semipermeable microcapsules by polymerization-induced phase separation. *Langmuir* 2015;31:6027–34.
- [204] Nam JO, Kim J, Jin SH, Chung YM, Lee CS. Microfluidic preparation of a highly active and stable catalyst by high performance of encapsulation of polyvinylpyrrolidone (PVP)-Pt nanoparticles in microcapsules. *J Colloid Interface Sci* 2016;464:246–53.
- [205] Axthelm F, Casse O, Koppenol WH, Nauser T, Meier W, Palivan CG. Antioxidant nanoreactor based on superoxide dismutase encapsulated in superoxide-permeable vesicles. *J Phys Chem B* 2008;112:8211–17.
- [206] Orive G, Gascón AR, Hernández RM, Igartua M, Pedraz JL. Cell microencapsulation technology for biomedical purposes: novel insights and challenges. *Trends Pharmacol Sci* 2003;24:207–10.
- [207] Park J, Kim K, Seo M. Hyper-cross-linked polymers with controlled multiscale porosity via polymerization-induced microphase separation within high internal phase emulsion. *Chem Commun* 2018;54:7908–11.
- [208] Williams JM. Toroidal microstructures from water-in-oil emulsions. *Langmuir* 1988;4:44–9.
- [209] Silverstein MS. PolyHIPEs: recent advances in emulsion-templated porous polymers. *Prog Polym Sci* 2014;39:199–234.
- [210] Cameron NR. High internal phase emulsion templating as a route to well-defined porous polymers. *Polymer (Guildf)* 2005;46:1439–49.
- [211] Pulko I, Krajnc P. High internal phase emulsion templating—a path to hierarchically porous functional polymers. *Macromol Rapid Commun* 2012;33:1731–46.
- [212] Pan X, Tasdelen MA, Laun J, Junkers T, Yagci Y, Matyjaszewski K. Photomediated controlled radical polymerization. *Prog Polym Sci* 2016;62:73–125.
- [213] Quinn JF, Barner L, Barner-Kowollik C, Rizzardo E, Davis TP. Reversible addition-fragmentation chain transfer polymerization initiated with ultraviolet radiation. *Macromolecules* 2002;35:7620–7.
- [214] Bobrin VA, Lee K, Zhang J, Corrigan N, Boyer C. Nanostructure control in 3D printed materials. *Adv Mater* 2022;34:2107643.
- [215] Bobrin VA, Yao Y, Shi X, Xiu Y, Zhang J, Corrigan N, Boyer C. Nano- to macro-scale control of 3D printed materials via polymerization induced microphase separation. *Nat Commun* 2022;13:3577.
- [216] Shi X, Bobrin VA, Yao Y, Zhang J, Corrigan N, Boyer C. Designing nanostructured 3D printed materials by controlling macromolecular architecture. *Angew Chem Int Ed* 2022;61:e202206272.
- [217] Lee K, Shang Y, Bobrin VA, Kuchel R, Kundu D, Corrigan N, Boyer C. 3D printing nanostructured solid polymer electrolytes with high modulus and conductivity. *Adv Mater* 2022;34:2204816.
- [218] Melodia D, Bhadra A, Lee K, Kuchel R, Kundu D, Corrigan N, Boyer C. 3D printed solid polymer electrolytes with bicontinuous nanoscopic domains for ionic liquid conduction and energy storage. *Small* 2023;2206639.
- [219] Lee J, Lopez G, Améduri B, Seo M. Synthesis of heterograft copolymers with a semifluorinated backbone by combination of grafting-through and grafting-from polymerizations. *Macromolecules* 2020;53:2811–21.
- [220] Sinner FM, Buchmeiser MR. Ring-opening metathesis polymerization: access to a new class of functionalized, monolith stationary phases for liquid chromatography. *Angew Chem Int Ed* 2000;39:1433–6.
- [221] Yu S, Qiu CW, Chong Y, Torquato S, Park N. Engineered disorder in photonics. *Nat Rev Mater* 2020;6:226–43.
- [222] Bates FS, Hillmyer MA, Lodge TP, Bates CM, Delaney KT, Fredrickson GH. Multiblock polymers: panacea or Pandora's box? *Science* 2012;336:434–40.
- [223] Wan Y, He J, Zhang Y. An arbitrarily regulated monomer sequence in multi-block copolymer synthesis by frustrated Lewis pairs. *Angew Chem Int Ed* 2023;62:e202218248.
- [224] Lau WJ, Ismail AF, Misdan N, Kassim MA. A recent progress in thin film composite membrane: a review. *Desalination* 2012;287:190–9.
- [225] Hampu N, Hillmyer MA. Temporally controlled curing of block polymers in the disordered state using thermally stable photoacid generators for the preparation of nanoporous membranes. *ACS Appl Polym Mater* 2019;1:1148–54.
- [226] Hampu N, Bates MW, Vidil T, Hillmyer MA. Bicontinuous porous nanomaterials from block polymers radically cured in the disordered state for size-selective membrane applications. *ACS Appl Nano Mater* 2019;2:4567–77.
- [227] Hampu N, Hillmyer MA. Molecular engineering of nanostructures in disordered block polymers. *ACS Macro Lett* 2020;9:382–8.
- [228] Hampu N, Hillmyer MA. Nanostructural rearrangement of lamellar block polymers cured in the vicinity of the order-disorder transition. *Macromolecules* 2020;53:7691–704.